A Network-Based Framework for Hydro-Geomorphic Modeling and Decision Support with Application to Space-Time Sediment Dynamics, Identifying Vulnerabilities, and Hotspots of Change

A DISSERTATION
SUBMITTED TO THE FACULTY OF
UNIVERSITY OF MINNESOTA
BY

Jonathan A. Czuba

IN PARTIAL FULFILLMENT OF THE REQUIREMENTS
FOR THE DEGREE OF
DOCTOR OF PHILOSOPHY

Efi Foufoula-Georgiou

May, 2016

Acknowledgements

I would like to express my sincere gratitude to my adviser Efi Foufoula-Georgiou for her support, encouragement, and inspiration during the past four years. I would also like to thank members of Efi's research group: Alejandro Tejedor, Anthony Longjas, Arvind Singh, Amy Hansen, Jon Schwenk, Zeinab Takbiri, Mohammad Danesh-Yazdi, and Mohammad Ebtehaj for insightful and stimulating discussions.

I would also like to thank Karen Gran (University of Minnesota, Duluth), Martin Bevis (University of Minnesota, Duluth), Patrick Belmont (Utah State University), and Peter Wilcock (Utah State University) for sharing their knowledge of the Minnesota River Basin and their data quantifying a sediment budget for the Le Sueur and Greater Blue Earth River Basins.

Thank you to the members of my committee, Michele Guala, Vaughan Voller, and Peter Wilcock (Utah State University) for your invaluable suggestions and comments.

Finally, I would like to thank my family, particularly my wife and daughter, for their continuous support and encouragement during these years.

This research was partly funded by NSF grant EAR-1209402 under the Water Sustainability and Climate Program (WSC): REACH (REsilience under Accelerated CHange) and benefited from collaborations made possible by NSF grant EAR-1242458 under Science Across Virtual Institutes (SAVI): LIFE (Linked Institutions for Future Earth). Additional financial support for this research was provided by (1) a University of Minnesota Civil Engineering Departmental Fellowship, (2) an Interdisciplinary Doctoral Fellowship through the University of Minnesota Graduate School and the Institute on the Environment, and (3) an Edward Silberman Fellowship through the St. Anthony Falls Laboratory at the University of Minnesota.

Abstract

Increasing pressure to meet the food, water, and energy demands of our growing society in a changing climate has strained the physical, chemical, and biological functioning of watersheds to maintain ecosystem services, such as providing clean water, and to sustain a productive and diverse ecosystem. Confronted with multifaceted environmental issues, watershed managers could use a simple first-order approach for understanding how physical, chemical, and biological processes operate within a watershed to guide watershed-management decisions. This research advances a network-based modeling framework for guiding effective landscape management decisions towards sustainability focusing on understanding large-scale system functioning and predicting the emergence of vulnerabilities, "hotspots" of change, and unexpected system behavior. Based on a combination of mathematical theory, field-data analysis, and numerical simulations applied to the dynamics of bed-material sediment (i.e., the sediment composing the riverbed) on river networks, we (1) identify a resonant frequency of sediment supply from network topology and sediment-transport dynamics that could lead to an unexpected downstream amplification of sedimentological response in the Minnesota River Basin; (2) identify hotspots of likely sediment-driven fluvial geomorphic change where sediment has a tendency to persist and exacerbate channel migration on the Greater Blue Earth River Network; and (3) elucidate the hierarchical role of river-network structure on bed-material sediment dynamics in propagating, altering, and amalgamating the emergent large temporal fluctuations and periodicities of bed-sediment thickness. By embedding small-scale bed-material sediment dynamics on a river network, this research shows that it is possible to gain a better understanding of the large-scale system functioning whereby management actions that target the identified critical times, places, and processes in the landscape will be most effective at improving water quality and the health of the aquatic ecosystem.

Contents

List of Figures

Notation

a_i	directly contributing area of link i [L^2]
A_b	bluff surface area projected onto a vertical plane [L^2]
A_i	upstream drainage area of link i [L^2]
A_r	incised area of a ravine [L^2]
b	near-bed distance above the bed [L]
$b_1 - b_5$	coefficients of the sediment fall velocity relation of *Dietrich* [1982] as presented by *Garcia* [2006]
B_i	channel width of link i [L]
$\bar{c}$	suspended-sediment concentration averaged over turbulence at a distance z above the bed [ML^3]
$\bar{c}_b$	near-bed suspended-sediment concentration averaged over turbulence [ML^3]
$C_{f,i}$	friction coefficient of link i
C_j	denotes cluster j
CPI_i	cluster persistence index of link i [MLT]
COV	coefficient of variation
d	index of the link directly downstream of link i
$dCOV$	deviation of the COV from that predicted for a Poisson distribution
$d_{k,l}$	inter-parcel distance between parcel p_k and the nearest downstream parcel p_l [L]
d^*	inter-parcel distance threshold for defining a cluster [L]
D_i	grain size of sediment in link i [L]
e_b	long-term, subbasin-average bluff erosion rate [LT^{-1}]

$f_{s,soil}$	fraction of sand in soil
$f_{s,till}$	fraction of sand in till
$f\left(h_{s,i,t}\right)$	probability distribution function of $h_{s,i,t}$
$\hat{f}\left(h_{s,i,t}\right)$	estimate of $f\left(h_{s,i,t}\right)$ assuming the in-channel storage process preserves the structure of a Poisson arrival process
$f\left(h_{s,i,t}^{act}\right)$	probability distribution function of $h_{s,i,t}^{act}$
$f\left(k_p;\lambda_i \bar{t}_{s,i}\right)$	Poisson distribution with index k_p and parameter $\lambda_i \bar{t}_{s,i}$
$f(t)$	travel time probability distribution function at a fixed control section
$f_{\xi_i}(t)$	travel time probability distribution function through geomorphic state ξ_i
$f_{\gamma_i}(t)$	travel time probability distribution function from link i to the outlet
g	acceleration due to gravity [LT^{-2}]
$g(\boldsymbol{X},t)$	displacement probability density function
$\bar{h}_{s,i}$	time-averaged bed-sediment thickness of link i [L]
$\bar{h}_{s,i}^{act}$	time-averaged bed-sediment thickness of the active-transport layer of link i [L]
$\bar{h}_{s,i}^{stor}$	time-averaged bed-sediment thickness of the storage layer of link i [L]
$h_{s,i,t}$	bed-sediment thickness of link i at time t [L]
$h_{s,i,t}^{act}$	bed-sediment thickness of the active-transport layer of link i at time t [L]
$h_{s,i,t}^{stor}$	bed-sediment thickness of the storage layer of link i at time t [L]
H_i	flow depth of link i [L]
$H_{s,i}$	bed-sediment thickness at capacity of link i [L]
i	link index
$iter$	index of the current iteration

$I_{f,g}$	intermittency factor for gravel transport
$I_{f,s}$	intermittency factor for sand transport
j	index denoting a specific cluster
k	index denoting a specific parcel
k_p	index of Poisson distribution
k_s	effective roughness height [L]
l	index denoting the nearest downstream parcel of parcel p_k
ℓ_i	length of link i [L]
$L_{a,i}$	active layer thickness of link i [L]
L_i	pathway distance from geomorphic state ξ_i to the outlet [L]
L_j	distance spanned by cluster C_j [L]
$L_{\max}$	maximum pathway distance [L]
m	mass of a sediment parcel [M]
m_i	total mass in link i [M]
M_j	mass within cluster C_j [M]
$M_{s,b}$	mass erosion rate of sand from a bluff [MT^{-1}]
$M_{s,r}$	mass erosion rate of sand from a ravine [MT^{-1}]
$M_{s,u}$	mass erosion rate of sand from an upland area [MT^{-1}]
n_i	total number of inputs of volume V_p upstream of link i but downstream of any lakes directly connected to the network
N	total number of links in the network
N_i	number of parcels within link i for duration $\bar{t}_{s,i}$
p_k	denotes the k^{th} (sediment) parcel
p_l	denotes the nearest l^{th} (sediment) parcel downstream of parcel p_k
p_ϕ	probability of occurrence of the ϕ^{th}–percentile daily streamflow

$q_{g,i}$	volumetric transport rate of gravel in link i [L^2T^{-1}]
$q_{g^*,i}$	dimensionless volumetric transport rate of gravel in link i
$\bar{q}_s$	mean annual volumetric transport rate of sand per unit width [L^2T^{-1}]
$q_{s,b}$	volumetric transport rate of sand per unit width at the two-year (bankfull) flow [L^2T^{-1}]
$q_{s,i}$	volumetric transport rate of sand in link i [L^2T^{-1}]
$q_{s^*,i}$	dimensionless volumetric transport rate of sand in link i
$q_{s,\phi}$	volumetric transport rate of sand per unit width in the ϕ^{th} percentile [L^2T^{-1}]
q_{ϕ}	ϕ^{th}–percentile daily streamflow [L^2T^{-1}]
$Q_{g,i}$	volumetric transport rate of gravel in link i [L^3T^{-1}]
$Q_{s,i,t}$	volumetric transport rate of sand in link i at time t [L^3T^{-1}]
$Q_{w,i}$	streamflow or volumetric transport rate of water in link i [L^3T^{-1}]
Q_2	two-year recurrence interval peak flow [L^3T^{-1}]
R_{ep}	dimensionless particle Reynolds number
R_f	dimensionless fall velocity
R_i	submerged specific gravity of sediment in link i
RC_i^{iter}	relative capacity of link i at iteration $iter$
$\widetilde{S}_i^{iter}$	iterated channel slope of link i at iteration $iter$
S_i^*	channel slope of link i where sediment transport equals supply
$S_{i,t}$	channel slope of link i at time t
t	time index
$t_{g,i}$	travel time of gravel through link i [T]
$t'_{g,i}$	travel time of gravel through link i during constant bankfull flow [T]

$t_{p,i}$	process-specific transport time through link i [T]
$\bar{t}_{s,i}$	time-averaged travel time of a sand parcel through link i [T]
$\tilde{t}_{s,i}^{iter}$	iterated travel time of a sand parcel through link i at iteration $iter$ [T]
$t_{s,i}^{*}$	travel time of a sand parcel through link i when sediment transport equals supply [T]
$t'_{s,i}$	travel time of sand through link i during constant bankfull flow [T]
$t_{s,i,t}$	travel time of a sand parcel through link i at time t [T]
$t_{w,i}$	travel time of mud (streamflow) through link i [T]
t_0	initial time index
T	dominant period of $h_{s,i,t}$ [T]
T_a	arrival time of a parcel at the control section [T]
$T_{g,i}$	pathway travel time of gravel from link i to the outlet [T]
$T_{p,i}$	process-specific pathway travel time from link i to the outlet [T]
$T_{p,\max}$	maximum process-specific pathway travel time [T]
$T_{s,i}$	pathway travel time of sand from link i to the outlet [T]
$T_{w,i}$	pathway travel time of mud (streamflow) from link i to the outlet [T]
u	time-averaged flow velocity at a distance z above the bed [LT^{-1}]
$u1$, $u2$	indices of directly upstream channel links
u_*	shear velocity [LT^{-1}]
$u_{g,i}$	characteristic velocity of gravel in link i [LT^{-1}]
$u_{p,i}$	process-specific velocity in link i [LT^{-1}]
$u_{w,i}$	streamflow velocity in link i [LT^{-1}]
$u_{s,i,t}$	bulk sand transport velocity in link i at time t [LT^{-1}]
V	arbitrary control volume

V_p	parcel volume [L^3]
$V_{s,i,t}$	total volume of sand from all parcels in link i at time t [L^3]
$V_{s,i,t}^{stor}$	total volume of sand in storage in link i at time t [L^3]
$W(x)$	width function
$W_g(t)$	process-scaled width function for gravel transport
$W_p(t)$	process-scaled width function
$W_s(t)$	process-scaled width function for sand transport
$W_w(t)$	process-scaled width function for mud transport (streamflow)
x	arbitrary pathway distance from the outlet measured along the network [L]
$\boldsymbol{X}$	Lagrangian coordinate of a parcel
$\boldsymbol{X}_0$	initial position of a parcel at time $t = 0$
$\boldsymbol{X}_{p_k}$	Lagrangian coordinate of parcel p_k
$\boldsymbol{\mathcal{X}}$	collection of Lagrangian parcel locations
Y_r	average annual ravine yield [ML^2T^{-1}]
Y_u	annual upland yield [ML^2T^{-1}]
z	distance above the bed [L]
Z_R	dimensionless Rouse number
α_g	coefficient of the gravel transport formula
α_{HA}	coefficient of the $H_i \sim A_i$ scaling relation
α_{u_wA}	coefficient of the $u_{w,i} \sim A_i$ scaling relation
β_g	exponent of the gravel transport formula
β_{HA}	exponent of the $H_i \sim A_i$ scaling relation
β_{u_wA}	exponent of the $u_{w,i} \sim A_i$ scaling relation
γ_i	connectivity of geomorphic state ξ_i to the outlet

$\tilde{\eta}_i^{iter}$	iterated bed elevation at the upstream end of link i at iteration $iter$ [L]
$\eta_{i,t}$	bed elevation at the upstream end of link i at time t [L]
θ_i	scale factor for determining the characteristic vertical length scale for sand transport in link i
κ	von Karman's constant
λ	rate parameter of the exponential interarrival time distribution [T^{-1}]
λ_i	rate of Poisson arrivals to link i [T^{-1}]
λ_p	porosity of bed-material sediment
ν	kinematic viscosity of water [L^2T]
ν_s	sediment fall velocity [LT^{-1}]
$\xi_{f,i}$	geomorphic fluvial state of link i
ξ_i	geomorphic state of link i
ρ	density of water [ML^{-3}]
ρ_s	sediment density [ML^{-3}]
ρ_{till}	average bulk density of till [ML^{-3}]
$\sigma_{h_s,i}$	standard deviation of $h_{s,i,t}$ [L]
$\tau_{b,i}$	bed shear stress in link i [$ML^{-1}T^{-2}$]
$\tau_{*c,i}$	critical dimensionless bed shear stress for the initiation of motion in in link i
$\tau_{*,i}$	dimensionless bed shear stress in link i
ϕ	index of a percentile
χ_i	volume of sediment moved at capacity through link i [L^3]
ψ	connectivity index along pathway γ_i
Ω	index of the basin outlet

Chapter 1

Introduction

One of the grand challenges of this century is how to sustain our society, as global populations swell from 7 billion today to an estimated 9 billion by 2050, and our environment, to meet growing demands for water, food, and energy. We as a society have grappled with this challenge, through an intensification and expansion of agriculture [*Lark et al*., 2015], but at the expense of degraded water quality in many streams and rivers and associated decline in diversity and number of aquatic species [*Carlisle et al.*, 2013]. Confronted with multifaceted environmental issues, watershed managers could use a simple first-order approach for understanding how physical, chemical, and biological processes operate within a watershed to guide watershed-management decisions. Further complicating the management options is the wide range of space and time scales involved in the cascade of changes and feedbacks among all the interacting processes in this complex human-natural system.

The main objective of this research is to advance a network-based modeling framework for guiding effective landscape management decisions towards sustainability focusing on understanding large-scale system functioning and predicting the emergence of vulnerabilities, "hotspots" of change, and unexpected system behavior. This research involved a combination of mathematical theory, field-data analysis, and numerical simulations with specific objectives of: (1) identifying synchronizations and amplifications of sediment delivery in river basins, (2) identifying hotspots of fluvial geomorphic change, and (3) elucidating the hierarchical role of river-network structure on bed-material sediment dynamics (i.e., the sediment composing the riverbed).

Landscapes are too complex to be modeled with fully distributed deterministic models that consider all the small-scale physics and interactions, due to large and unavoidable uncertainties associated with the myriad of relevant processes. Besides, changes in climate, land use, and water management impose non-stationary conditions and also nonlinearities in the system make it sensitive to small perturbations. Instead, the aim of the developed framework is to capture the most important interactions and amplifications by exploring the system connectivity and its transport pathways including residence times, threshold behavior, and physical transformations. This is accomplished by: (1) establishing the connectivity network of flow pathways from an underlying digital elevation model (DEM), (2) attributing those flow pathways with hydro-geomorphic attributes relevant to the process dynamics from field and remotely sensed data, (3) spatially and temporally distributing inputs of water, sediment, and/or nutrients, and (4) tracking these inputs from a Lagrangian perspective on the network via process-based time delays.

For this research, the 44,000 km^2 Minnesota River Basin serves as a test bed for application of the developed framework. The Minnesota River Basin is impaired under the Clean Water Act for excessive sediment and nutrients as well as degraded aquatic life [*Carlisle et al.*, 2013; *MPCA*, 2014]. These impairments are due to a unique combination of (1) a geologic legacy from glacial and post-glacial processes characterized by rapidly down-cutting rivers with tall bluffs vulnerable to river erosion [*Gran et al.*, 2009, 2011b, 2013; *Belmont et al.*, 2011; *Day et al.*, 2013], (2) climate change leading to an increase in short duration, large precipitation events [*Angel and Huff*, 1997; *Groisman et al.*, 2004, 2012; *Michaels et al.*, 2004; *Pryor et al.*, 2009], and (3) widespread changes in agricultural land and water management which has increased the volume and rate at which water is delivered to streams [*Zhang and Schilling*, 2006; *Novotny and Stefan*, 2007; *Dadaser-Celik and Stefan*, 2009; *Blann et al.*, 2009; *Schottler et al.*, 2014; *Foufoula-Georgiou et al.*, 2015]. Recent studies have clearly documented increased near-channel sediment production [*Belmont et al.*, 2011] and stream morphologic changes such as channel widening [*Lenhart et al.*, 2013; *Schottler et al.*, 2014]. At the same time, a decline in macroinvertebrates, sensitive fish species, and native mussels has also been

reported [*Kirsch et al.*, 1985; *Musser et al.*, 2009] and the decline in native mussels potentially linked to increased suspended-sediment concentrations [*Hansen et al.*, 2016].

As such, the cascade of changes from water to sediment to river biology is dictated by the propagation of those quantities on the river network, the "skeleton" of the landscape. By embedding small-scale process dynamics on the connected network, specifically bed-material sediment dynamics on a river network, this research shows that it is possible to gain a better understanding of the large-scale system functioning whereby management actions that target the identified critical times, places, and processes in the landscape will be most effective at improving water quality and the health of the aquatic ecosystem.

In Chapter 2, we propose a simplified network-based predictive framework of environmental response in a basin, which incorporates network topology, channel characteristics, and transport-process dynamics to perform a non-linear process-based scaling of the river-network width function to a time-response function. We develop the process-scaling formulation for transport of mud, sand, and gravel, using simplifying assumptions including neglecting long-term storage, and apply the methodology to the Minnesota River Basin. We identify a robust bimodal distribution of the sedimentological response for sand of the basin which we attribute to specific source areas, and identify a resonant frequency of sediment supply where the disturbance of one area followed by the disturbance of another area after a certain period of time, may result in amplification of the effects of sediment inputs which would be otherwise difficult to predict. We perform a sensitivity analysis to test the robustness of the proposed formulation to model parameter uncertainty and use observations of suspended sediment at several stations in the basin to diagnose the model.

In Chapter 3, we put forward the hypothesis that places in the network predisposed (due to process dynamics and network topology) to accumulate excess sediment over a considerable river reach and over a considerable period of time reflect locations where a local imbalance in sediment flux may occur thereby highlighting a susceptibility to potential fluvial geomorphic change. We develop a dynamic connectivity framework which uses the river network structure and a simplified Lagrangian transport model to

trace fluxes through the network and integrate emergent "clusters," i.e., places of excess flux accumulation, through a cluster persistence index (CPI). The framework was applied to sand transport in the Greater Blue Earth River Network in the Minnesota River Basin. We show how this framework can be used to assess the persistence of mass within different reaches of a network and ultimately identify hotspots of fluvial geomorphic change associated with observed high rates of channel migration. This framework was then used to pinpoint the sources of sediment contributing to large clusters which can be useful information for management decisions.

In Chapter 4, we develop a network-based model of bed-material sediment and extensively describe its implementation in the Greater Blue Earth River Basin in southern Minnesota. This model combines spatially-explicit sediment sourcing with in-channel transport and storage dynamics within the network-based framework described in chapters 2 and 3. We analytically derive the quasi-steady-state, spatio-temporal characteristics of bed-sediment thickness from the mechanistic underpinnings of the model and the hierarchical structure of the river network – all without the need for numerical simulations. We then use the model to simulate the transport and storage of bed-material sediment over a 600-year time period and the spatio-temporal characteristics of bed-sediment thickness. Furthermore, we use the model to isolate the influence of river-network structure on bed-material sediment dynamics in propagating, altering, and amalgamating the emergent, large temporal fluctuations and periodicities of bed-sediment thickness.

In Chapter 5, we close with concluding remarks and perspectives on future research.

Chapter 2

A Network-Based Framework for Identifying Potential Synchronizations and Amplifications of Sediment Delivery in River Basins

Long-term prediction of environmental response to natural and anthropogenic disturbances in a basin becomes highly uncertain using physically-based distributed models, particularly when transport time scales range from tens to thousands of years, such as for sediment. Yet, such predictions are needed as changes in one part of a basin now might adversely affect other parts of the basin in years to come. In this chapter we propose a simplified network-based predictive framework of sedimentological response in a basin, which incorporates network topology, channel characteristics, and transport-process dynamics to perform a non-linear process-based scaling of the river-network width function to a time-response function. We develop the process-scaling formulation for transport of mud, sand, and gravel, using simplifying assumptions including neglecting long-term storage, and apply the methodology to the Minnesota River Basin. We identify a robust bimodal distribution of the sedimentological response for sand of the basin which we attribute to specific source areas, and identify a resonant frequency of sediment supply where the disturbance of one area followed by the disturbance of another area after a certain period of time, may result in amplification of the effects of sediment

inputs which would be otherwise difficult to predict. We perform a sensitivity analysis to test the robustness of the proposed formulation to model parameter uncertainty and use observations of suspended sediment at several stations in the basin to diagnose the model. The proposed framework has identified an important vulnerability of the Minnesota River Basin to spatial and temporal structuring of sediment delivery.

2.1 Introduction

For long-term prediction of the environmental response of a basin to natural and anthropogenic disturbances, physically-based distributed models are of limited use as they need many input parameters which are hard to specify and predictions become increasingly uncertain as the prediction horizon increases. For example, the transport time scale for mud (silt and clay) can be of the order of hours to days (storm-event response), while for sand and gravel can be of the order of tens to thousands of years, depending on climate and basin characteristics. When predicting such long-term response, the specific magnitude of the predicted flux might not be very accurate but the timing of the maximum flux, and also the identification of areas of the basin contributing to that maximum flux are important for long-term planning and for assessing how human-changes on a naturally evolving landscape might inadvertently affect downstream changes in many years to come.

Landscapes contain networks of dynamically connected paths (fluvial, hillslope, subsurface, etc.) that play an important role in structuring environmental fluxes and the overall basin response to a given input. An environmental response, defined as the time distribution of a quantity of interest (streamflow, sediment, nutrients, etc.) at the outlet of a basin due to a spatially distributed input, is structured by the network through time delays and transformations imposed by the physics of the environmental process operating on that network. Simplified approaches that take advantage of network topology, channel characteristics, and transport-process dynamics offer the possibility to identify hot spots or vulnerable areas/times of disturbance that can lead to synchronization and downstream amplification of the response.

Inspired by the extensive linear systems theory approach to the hydrologic response [*Sherman*, 1932; *Nash*, 1957; *Dooge, 1973; Kirkby*, 1976; *Rodriguez-Iturbe and Valdes*, 1979; *Gupta et al.*, 1980; *Troutman and Karlinger*, 1985; *Gupta et al.*, 1986; *Mesa and Mifflin*, 1986; *Gupta and Mesa*, 1988; *Maidment et al.*, 1996; *Muzik*, 1996; *Rinaldo et al*., 2006a, 2006b; *Botter et al*., 2010] and its extension to the sedimentological response for mud at the storm-event time scale [*Johnson*, 1943; *Williams*, 1978; *Kumar and Rastogi*, 1987; *Sharma et al.*, 1992; *Raghuwanshi et al.*, 1994; *Gracia-Sanchez*, 1996; *Lee and Singh*, 1999; *Kalin et al.*, 2004a, 2004b; *Singh et al.*, 2008; *Bhunya et al.*, 2010; *Lee and Yang*, 2010], we propose here a conceptual framework for computing the "sedimentological response function" of a basin focusing specifically on the transport of mud, sand, and gravel. The sedimentological response function is defined as the time distribution of the sediment quantity delivered to the outlet of a basin in response to an instantaneous unit input of sediment uniformly distributed over the basin. This response function is computed by performing a non-linear process-based scaling of the network width function (the probability distribution of distances to the outlet) into a time response function. The framework incorporates not only the network topology, but also (via process-based scaling) specific attributes of the three-dimensional structure of the landscape, stream morphology, and hydrodynamics that contribute to sediment production and transport, such as slope, depth, and width of the river at any location, shear stress of the bed, relevant magnitude/frequency of flow, etc. Using scaling functions (such as hydraulic geometry) the proposed framework can be considerably simplified and reduced down to a few parameters that can convert the network width function to a process-scaled response function.

In this chapter we present the proposed framework for transport of mud, sand, and gravel and demonstrate it in a specific high sediment production regime in the Minnesota River Basin. This basin was selected as a prototype because excessive sediment impairs river water quality and biotic functioning, and the management of current and future actions on the landscape requires unraveling the temporal and spatial effects of these actions, as well as understanding how the environment continues to respond to past actions and disturbances.

2.2 Conceptual Framework of Environmental Response

The proposed connectivity-based conceptual framework of environmental response relies on performing a physically-based scaling of the distances (link lengths) along the network by characteristic velocities of the flux transported on the network to obtain the "environmental response function" for the flux of interest. The environmental response function provides significant insight into the "workings of the system" (in terms of both its structural components and dynamics) and provides a building block for computing the flux at the outlet of the basin in response to any temporally variable input in the basin, under of course, the proportionality and superposition assumptions of linear system theory. The theoretical basis of the proposed framework rests on the link between Lagrangian and Eulerian transport formalisms by which one can establish the relation between the evolution in time and space of the trajectories of an ensemble of particles injected over a set of points at an initial time and transported over all possible trajectories in the network, to the first passage (or travel time) distribution at a fixed control section, here at the outlet of the basin [e.g., *Rodriguez-Iturbe and Rinaldo*, 1997].

Let the river network be defined by a set of hierarchically connected links i, where a link is defined as the segment of the network between a source and a junction (a source link), two successive junctions, or a junction and the basin outlet. Junctions are the points at which two links join, sources are the points farthest upstream in the network, and the outlet is the point farthest downstream in the network. Each link i is assigned a geomorphic fluvial state $\xi_{f,i}$ which may include geomorphologic and hydraulic attributes of the link, i.e., $\xi_{f,i}\left(\ell_i, a_i, A_i, S_i, Q_{w,i}, H_i, B_i, ...\right)$, where the geomorphologic attributes may include the link length ℓ_i [L], directly contributing area a_i [L^2], upstream drainage area A_i [L^2], and link slope S_i, and the hydraulic attributes may include the streamflow $Q_{w,i}$ [L^3T^{-1}], cross-section average depth H_i [L], average width B_i [L], etc. (Figure 2.1a). While not indicated explicitly, attributes of the geomorphic state $\xi_{f,i}$ may also be a function of time to capture possible time-varying properties of the system.

Let now γ_i denote the pathway (set of links) that a particle initiating at link i will follow along the river network to reach the outlet. The properties of this pathway are defined by the hierarchical (directed) collection of the geomorphic fluvial states of the links composing γ_i, i.e., $\{\xi_i,...,\xi_\Omega\}$ from the geomorphic state ξ_i through the network to the outlet (i.e., $\xi_i \to ... \to \xi_\Omega$). It is noted that, in general, a landscape can be seen as a set of connected paths, which in addition to fluvial paths might include hillslope, subsurface, floodplain, pond/wetland, pipe, etc. paths which can also be incorporated in the above framework if their properties are known. In what follows we restrict ourselves to fluvial paths only.

A particle introduced into link i has a pathway distance L_i [L] from that point to the outlet given by

$$L_i = \sum_{\psi \in \gamma_i} \ell_\psi \,, \tag{2.1}$$

which is the sum of link lengths along pathway γ_i. The width function (WF) $W(x)$ is defined as the number of links in the network (typically normalized by the total number of links) which are found at a discretized pathway distance x [L] from the outlet measured along the network (Figure 2.1b). Thus, in the limit of a large number of pathways, the WF is the probability distribution of pathway distances to the outlet of the basin. The directed network of link lengths ℓ_i [L] may be transformed to a directed network of travel times $t_{p,i}$ [T] based on a process operating on the network, say through a process-specific velocity $u_{p,i}$ [LT^{-1}] of the transported environmental flux. The travel time $t_{p,i}$ is the time it takes a particle to move through (or the time during which a particle is in) geomorphic state ξ_i and is given by

$$t_{p,i} = \frac{\ell_i}{u_{p,i}}. \tag{2.2}$$

Note that $t_{p,i}$ must include both the time when the particle is actually moving and the time when it is not being transported, i.e., it stays in storage within link i. When long-

term storage is present, then $u_{p,i}$ represents a virtual velocity whose physical meaning has to be interpreted with caution. Here, as detailed in section 2.3, long-term storage effects are ignored and only short-term storage (due to the intermittency of flood events capable of transporting sediment) is incorporated via an intermittency factor formalism (explained in more detail in section 2.4.4). Considering this length-to-time conversion, a particle introduced into link i has a pathway travel time $T_{p,i}$ [T] to the outlet given by

$$T_{p,i} = \sum_{\psi \in \gamma_i} t_{p,\psi} \,, \tag{2.3}$$

which is the sum of travel times along pathway γ_i. Thus, when such transport dynamics are introduced on the river network, each pathway distance to the outlet is scaled to a travel time to the outlet. This allows one to compute the probability that a particle found at the outlet at time t [T] was in position x (and thus within an upstream link at distance x from the outlet) at time $t = 0$. This distribution produces a process-scaled width function (PSWF) $W_p(t)$ defined as the number of links in the network (normalized by the total number of links) that contribute to the outlet at time t (Figure 2.1c). This PSWF is also the probability distribution of pathway travel times of particles (introduced instantaneously and uniformly in all links in the network) to the outlet of the basin, and as such relates to the geomorphologic instantaneous unit response function (GIURF) of the basin. It is understood that the contributions of different areas of the basin to the WF may be considerably redistributed in the PSWF based on the characteristics of the process of interest (Figure 2.1); e.g., particles injected at two points which are at the same distance to the outlet might arrive at the outlet at significantly different times depending on the transport properties of their pathways (slopes, channel hydraulic properties, bed friction, etc.). Obviously, if the process-specific velocity u_p is constant for all links, the PSWF (normalized by the maximum process-specific pathway travel time $T_{p,\max}$ [T]) and the WF (normalized by the maximum pathway distance $L_{\max}$ [L]) coincide. In the next section, the PSWF (or GIURF) is formulated for mud, sand, and gravel transport in a river network.

2.3 Formulation of the Sedimentological Response Function

Sediment in large and small quantities is intermittently and spatially non-uniformly supplied to river networks [*Benda and Dunne*, 1997a, 1997b; *Reid et al*., 2007a] across a broad range of sizes that include clay (< 4 μm), silt (4 – 62 μm), sand (0.062 – 2 mm), gravel (2 – 64 mm), and cobbles (6.4 – 25.6 cm) (following the sedimentological phi scale of *Garcia* [2008]). Once emplaced in the river, sediment is transported downstream by the next capable streamflow and transitions between various transient storage zones (e.g., channel bed, bars, floodplain) on its way to the outlet [*Harvey*, 2002; *Malmon et al*., 2003; *Reid et al*., 2007b; *Lauer and Parker*, 2008; *Fryirs*, 2013; *Pizzuto et al.*, 2014].

The connectivity-based conceptual framework of environmental response is applied to the process of sediment transport. Herein, equations for the characteristic velocity of sediment are developed for mud (within a particle-size range for clay and silt), sand, and gravel (a term used herein to collectively describe the particle-size range for gravel and cobbles) considering only the transport time (and not long-term storage time) through each geomorphic fluvial state $\xi_{f,i}$. In many systems, storage is an important component in the transfer of sediment out of a basin and must be incorporated in sediment-transport formulations. In principle, there is no conceptual difficulty in incorporating storage in the sedimentological response function approach presented here, by specifying residence times and accounting for the transitions between the channel and transient storage zones (e.g., floodplains); however, lack of data for its characterization has prompted us to exclude it from the present analysis. The equations for the characteristic velocity for each class of sediment (developed under a set of clearly defined assumptions) are used to develop PSWFs, which represent the geomorphologic instantaneous unit sedimentographs (GIUS) for each class of sediment. It is noted that for any real system subject to temporally variable inputs, the observed response at the outlet can be realized by convolving partitioned and scaled versions of the GIUS that reflect the specific sediment supply conditions. Also, spatially variable inputs can be handled by computing the GIUS over smaller basins where sediment input can be comfortably considered spatially uniform.

2.3.1 Mud Response Function

During transport by streamflow, turbulence is generally strong enough to carry mud (clay and silt) in continuous suspension. This leads to a uniform distribution of mud in the water column, a characteristic vertical length scale for mud transport as the flow depth, and a characteristic velocity of mud transport as that of the streamflow.

The characteristic velocity of mud transport (streamflow velocity) $u_{w,i}$ [LT^{-1}] can be obtained in several ways, including through hydraulic equations and hydraulic geometry relations. However, hydraulic equations, such as Manning's equation, require the specification of a channel roughness in addition to a characteristic streamflow throughout the network. The specified channel roughness should be verified against hydraulic measurements to ensure the simulated hydraulics is reasonable and not driving the flow towards supercritical on moderate slopes. Hydraulic geometry relations specify hydraulic variables based on a characteristic streamflow or drainage area alone, and these relations can be readily determined from gage data within the basin. Using hydraulic geometry, the characteristic velocity of mud transport (streamflow) scales as

$$u_{w,i} = \alpha_{u_w A} A_i^{\beta_{u_w A}} \tag{2.4}$$

where A_i [L^2] is the drainage area upstream of link i, and $\alpha_{u_w A}$ and $\beta_{u_w A}$ are the coefficient and exponent, respectively, of the scaling relation. The parameters $\alpha_{u_w A}$ and $\beta_{u_w A}$ can be determined directly from gage data within the basin or in the absence of these data, typical hydraulic geometry exponents can be used [*Leopold and Maddock*, 1953; *Leopold et al.*, 1964; *Park*, 1977]. The characteristic velocity scaling of equation (2.4) leads to the travel time scaling as

$$t_{w,i} = \frac{\ell_i}{\alpha_{u_w A}} A_i^{-\beta_{u_w A}} . \tag{2.5}$$

Summing the travel time along pathway γ_i gives the pathway travel time as

$$T_{w,i} = \sum_{\psi \in \gamma_i} t_{w,\psi} , \tag{2.6}$$

which can be used to obtain the PSWF for mud transport (streamflow) $W_w(t)$.

2.3.2 Sand Response Function

Sand is transported by streamflow throughout the water column, with the highest concentrations near the bed. Turbulence acts to lift sand into suspension; the weight of particles cause it to fall back towards the bed. In the absence of sufficient turbulence to lift sand into suspension, sand is transported along the bed. The characteristic velocity of sand can be described as a bulk velocity of sand $u_{s,i}$ [LT^{-1}] and can be obtained by combining equations for the volumetric transport rate of sand, channel hydraulics, and sand transport.

The volumetric transport rate of sand $Q_{s,i}$ [L^3T^{-1}] can be decomposed as

$$Q_{s,i} = u_{s,i}(\theta_i H_i)B_i, \tag{2.7}$$

where H_i [L] is the channel depth, θ_i is a scale factor, and B_i [L] is the channel width of link i. The term $\theta_i H_i$ defines a characteristic vertical length scale for sand transport where the majority of sand transport takes place (see section 2.4.5). The scale factor θ_i will vary depending on the flow (turbulence): larger for higher flows when more sand is lifted into suspension and smaller for lower flows when sand primarily transports along the bed.

Streamflow exerts a stress on the sediment composing the bed, which can be estimated assuming uniform (normal) flow for the channel hydraulics as

$$\tau_{b,i} = \rho g H_i S_i = \rho C_{f,i} u_{w,i}^2, \tag{2.8}$$

where $\tau_{b,i}$ [$ML^{-1}T^{-2}$] is the bed shear stress, S_i is the channel slope, and $C_{f,i}$ is the friction coefficient of link i, ρ is the density of water [ML^{-3}], and g is the acceleration due to gravity [LT^{-2}]. Additionally, the volumetric transport rate of water $Q_{w,i}$ [L^3T^{-1}] through link i is

$$Q_{w,i} = u_{w,i} H_i B_i. \tag{2.9}$$

The stress exerted on the bed sediment can be related to the transport rate of that sediment through the sand-transport formula of *Engelund and Hansen* [1967] for the total

sand load (neglecting the shear stress partition for bedforms) as

$$q_{s*,i} = \frac{0.05}{C_{f,i}}\left(\tau_{*,i}\right)^{5/2}, \tag{2.10}$$

where $q_{s*,i}$ is the dimensionless volumetric transport rate of sand per unit width and $\tau_{*,i}$ is the dimensionless bed shear stress in link i,

$$q_{s*,i} = \frac{q_{s,i}}{\sqrt{R_i g D_i} D_i}, \tag{2.11}$$

where $q_{s,i}$ [L^2T^{-1}] is the volumetric transport rate of sand per unit width, R_i is the submerged specific gravity of sediment, and D_i [L] is the sediment grain size in link i,

$$q_{s,i} = \frac{Q_{s,i}}{B_i}, \tag{2.12}$$

and

$$\tau_{*,i} = \frac{\tau_{b,i}}{\rho g R_i D_i}. \tag{2.13}$$

The above equations relate streamflow to bed shear stress to sand transport rate to the characteristic velocity of sand transport. These equations combine and simplify to

$$u_{s,i} = \frac{0.05}{\theta_i g^{1/2} R_i^2 D_i} u_{w,i}^2 H_i^{1/2} S_i^{3/2}. \tag{2.14}$$

As mentioned above, there are several ways of obtaining relations for flow velocity and depth. Again, hydraulic geometry relations are used to provide equations for flow velocity from equation (2.4) and depth as

$$H_i = \alpha_{HA} A_i^{\beta_{HA}}, \tag{2.15}$$

where α_{HA} and β_{HA} are the coefficient and exponent, respectively, of the scaling relation. The parameters α_{HA} and β_{HA} can be determined directly from gage data within the basin or in the absence of these data, typical hydraulic geometry exponents can be used [*Leopold and Maddock*, 1953; *Leopold et al.*, 1964; *Park*, 1977].

Substituting the relations for the flow velocity (equation 2.4) and depth (equation 2.15) into equation (2.14) provides an equation for the characteristic velocity of sand

transport in terms of variables that can be specified or easily extracted from a digital elevation model (DEM) as

$$u_{s,i} = \frac{0.05}{\theta_i g^{1/2} R_i^2 D_i} \alpha_{u_w A}^2 \alpha_{HA}^{1/2} A_i^{2\beta_{u_w A} + \beta_{HA}/2} S_i^{3/2} . \tag{2.16}$$

The characteristic velocity scaling of equation (2.16) leads to a travel time scaling of

$$t'_{s,i} = \frac{\theta_i g^{1/2} R_i^2 D_i}{0.05 \alpha_{u_w A}^2 \alpha_{HA}^{1/2}} \ell_i A_i^{-(2\beta_{u_w A} + \beta_{HA}/2)} S_i^{-3/2} , \tag{2.17}$$

where $t'_{s,i}$ is the travel time of sand in geomorphic fluvial state $\xi_{f,i}$, and in this formulation a characteristic flow is implicitly tied to the scaling of hydraulic variables with drainage area. Therefore, $t'_{s,i}$ represents the time it would take sand to move through geomorphic fluvial state $\xi_{f,i}$ if the flow implicit in the hydraulic scaling were held constant during this time.

However, streamflows capable of significantly transporting sediment occur for short periods intermittently throughout the year. As a simplification, rather than determining incremental travel times for sediment based on daily flows, a representative flow that transports sediment, such as bankfull flow, can be used to determine the channel hydraulics. Then a simulated time of continuous bankfull flow can be translated into real time by incorporating an intermittency factor $I_{f,s}$ [*Paola et al.*, 1992; *Parker*, 2004] where

$$t'_{s,i} = I_{f,s} t_{s,i} . \tag{2.18}$$

The intermittency factor denotes the fraction of time per year that continuous bankfull flow would yield the mean annual sand load (see section 2.4.4). In this way, time is scaled so that in one year, the mean annual sand load has been transported by continuous bankfull flow. It is important to note that the intermittency factor is specified with respect to the sand-transport process and not (directly) from the recurrence of the bankfull flow.

Introducing the intermittency factor of equation (2.18) into equation (2.17) leads to the travel time scaling of

$$t_{s,i} = \frac{\theta_i g^{1/2} R_i^2 D_i}{0.05 \alpha_{u_w A}^2 \alpha_{HA}^{1/2} I_{f,s}} \ell_i A_i^{-(2\beta_{u_w A} + \beta_{HA}/2)} S_i^{-3/2} . \tag{2.19}$$

Summing the travel time along pathway γ_i gives the pathway travel time

$$T_{s,i} = \sum_{\psi \in \gamma_i} t_{s,\psi} , \tag{2.20}$$

which can be used to obtain the PSWF for sand transport $W_s(t)$.

2.3.3 Gravel Response Function

Gravel (gravel and cobbles) is much larger in size than sand and is therefore much harder to move. Thus, gravel is transported by streamflow along the bed of a river. The transport of gravel occurs in a layer of active transport that is typically a few particle diameters thick [*Parker*, 2008]. The development of the characteristic velocity of gravel $u_{g,i}$ [LT^{-1}] is similar to that for sand, but specific to gravel transport, which includes an appropriate characteristic vertical length scale and sediment transport relation for gravel transport. The equations for channel hydraulics for uniform (normal) flow remain the same.

The volumetric transport rate of gravel $Q_{g,i}$ [L^3T^{-1}] can be decomposed as

$$Q_{g,i} = u_{g,i} L_{a,i} B_i , \tag{2.21}$$

where $L_{a,i}$ [L] is the active layer thickness of link i and defines a characteristic vertical length scale for gravel transport. The stress exerted on the bed sediment can be related to the transport rate of that sediment through a gravel transport formula [e.g., *Wong and Parker*, 2006] of the form

$$q_{g^*,i} = \alpha_g \left(\tau_{*,i} - \tau_{*c,i} \right)^{\beta_g} , \tag{2.22}$$

where $q_{g^*,i}$ is the dimensionless volumetric transport rate of gravel per unit width and $\tau_{*c,i}$ is the critical dimensionless bed shear stress for the initiation of motion in link i, α_g and β_g are the coefficient and exponent of the gravel transport formula, respectively,

$$q_{g^*,i} = \frac{q_{g,i}}{\sqrt{R_i g D_i} D_i} , \tag{2.23}$$

where $q_{g,i}$ [L^2T^{-1}] is the volumetric transport rate of gravel per unit width and

$$q_{g,i} = \frac{Q_{g,i}}{B_i}. \tag{2.24}$$

The above equations relate streamflow to bed shear stress to gravel transport rate to the characteristic velocity of gravel transport. These equations combine and simplify to

$$u_{g,i} = \frac{R_i^{1/2} g^{1/2} D_i^{3/2} \alpha_g}{L_{a,i}} \left(\frac{H_i S_i}{R_i D_i} - \tau_{*c,i} \right)^{\beta_g}. \tag{2.25}$$

Substituting the scaling relation for flow depth (equation 2.15) into equation (2.25) provides an equation for the characteristic velocity of gravel transport in terms of variables that can be specified or easily extracted from a DEM as

$$u_{g,i} = \frac{R_i^{1/2} g^{1/2} D_i^{3/2} \alpha_g}{L_{a,i}} \left(\frac{\alpha_{HA} A_i^{\beta_{HA}} S_i}{R_i D_i} - \tau_{*c,i} \right)^{\beta_g}. \tag{2.26}$$

The characteristic velocity scaling of equation (2.26) leads to a travel time scaling of

$$t'_{g,i} = \frac{L_{a,i}}{R_i^{1/2} g^{1/2} D_i^{3/2} \alpha_g} \ell_i \left(\frac{\alpha_{HA} A_i^{\beta_{HA}} S_i}{R_i D_i} - \tau_{*c,i} \right)^{-\beta_g}, \tag{2.27}$$

where $t'_{g,i}$ is the travel time of gravel in geomorphic fluvial state $\xi_{f,i}$, and in this formulation a characteristic flow is implicitly tied to the scaling of hydraulic variables with drainage area. As for sand, bankfull flow is used to determine the scaling of the channel hydraulics. Therefore, a simulated time of continuous bankfull flow can be translated into real time by incorporating an intermittency factor $I_{f,g}$ [*Paola et al*., 1992; *Parker*, 2004] where

$$t'_{g,i} = I_{f,g} t_{g,i}. \tag{2.28}$$

The intermittency factor denotes the fraction of time per year that continuous bankfull flow would yield the mean annual gravel load. The intermittency factor for gravel transport is different from the intermittency factor for sand even though the streamflow driving the process may be the same. Introducing the intermittency factor of equation (2.28) into equation (2.27) leads to the travel time scaling of

$$t_{g,i} = \frac{L_{a,i}}{R_i^{1/2} g^{1/2} D_i^{3/2} \alpha_g I_{f,g}} \ell_i \left(\frac{\alpha_{HA} A_i^{\beta_{HA}} S_i}{R_i D_i} - \tau_{*c,i} \right)^{-\beta_g} . \tag{2.29}$$

Summing the travel time along pathway γ_i gives the pathway travel time

$$T_{g,i} = \sum_{\psi \in \gamma_i} t_{g,\psi} , \tag{2.30}$$

which can be used to obtain the PSWF for gravel transport $W_g(t)$.

2.3.4 Major Assumptions

The GIUS is the sedimentological response of a basin to the generation of an instantaneous unit volume of sediment uniformly entering all links of the network; it explicitly incorporates the network topology, channel characteristics, and transport-process dynamics. The PSWF for mud, sand, and gravel (developed herein) is the GIUS for each class of sediment under the following assumptions:

1. Uniform (normal) flow.
2. Wide rectangular channel; that is, the hydraulic radius is approximated by the average depth.
3. The scaling of hydraulic characteristics (streamflow, velocity, depth, and width) from gages represents the hydraulics of the entire channel network.
4. The bankfull flow is constant during the entire period of response. The sedimentological effect (for sand and gravel) from a simulated bankfull flow can be transformed into real time by an intermittency factor.
5. Sediment-transport formulas (of the form of *Engelund and Hansen* [1967] for sand and *Wong and Parker* [2006] for gravel) represent the sediment-transport process.
6. Total shear stress drives sediment transport. There is no partitioning of shear stress due to the potential presence of bedforms.
7. The characteristic velocity of sediment can be obtained from the volumetric transport rate of sediment divided by a characteristic area (channel width B_i multiplied by a characteristic vertical length scale, H_i for mud, $\theta_i H_i$ for sand, and

$L_{a,i}$ for gravel).

8. No storage or morphologic change occurs in the river network over time. That is, there is no erosion, deposition, or change in any channel characteristics over time; there is no feedback from sediment transport back to channel morphology. The sediment supplied does not overwhelm the transport capacity.
9. No mechanism is present for dispersion of sediment other than geomorphologic dispersion due to the network topology.
10. No attrition of sediment occurs within the river network. That is, the sediment supplied to the system retains its size through the system. Sediment does not abrade or break down into smaller particles as it is transported downstream.
11. Delivery of sediment to the network is represented by an instantaneous unit input of sediment with grain size D_i supplied to the upstream end of links.
12. Every point in the watershed drains to a singular, unique outlet point. No local depressions are allowed in the network; only geomorphic fluvial states.
13. Sedimentological response is linear. Individual responses can be superimposed with each other.
14. Sedimentological response is time invariant. The response is always the same irrespective of when it occurs.

This chapter explores a formulation of the GIUS for mud, sand, and gravel and as a first step toward understanding basin-scale response of sediment, it makes several simplifying assumptions as discussed above. However, many of these assumptions can be relaxed within the proposed framework to provide a more realistic sedimentological response.

2.4 Application to the Minnesota River Basin

In applying this framework to the Minnesota River Basin, we first begin by describing the landscape setting (section 2.4.1) and the extraction of the river network from an underlying DEM to obtain link attributes (section 2.4.2). In further parameterizing the sedimentological response function, we describe the hydraulic geometry scaling (section

2.4.3), the intermittency factor for sand transport (section 2.4.4), and the characteristic vertical length scale for sand transport (section 2.4.5). Then we describe the formulation of travel times for the sedimentological response functions (section 2.4.6) and conclude this section with an estimate of the rate of total sand transport (section 2.4.7).

2.4.1 Landscape Setting

The Minnesota River accounts for 80-90% of the total sediment delivered to Lake Pepin, a naturally dammed lake on the Mississippi River about 80 km downstream of the mouth of the Minnesota River (Figure 2.2), from the combined basins of the Minnesota, St. Croix, and upper Mississippi Rivers, despite the fact that it accounts for only about one third of the total drainage area [*Kelley and Nater*, 2000]. The Minnesota River drains approximately 44,000 km^2 in southern Minnesota and parts of South Dakota, Iowa, and North Dakota, and is tributary to the Mississippi River just south of Minneapolis-St. Paul, Minnesota (Figure 2.2). The landscape of the Minnesota River Basin has been sculpted by glaciers and geomorphic processes associated with their retreat, notably with the carving of the Minnesota River valley after glacial Lake Agassiz drained catastrophically through the proto-Minnesota River 13,400 years ago [*Clayton and Moran*, 1982]. The incision of the mainstem Minnesota River reduced the base level of its tributaries which created knickpoints, or sharp increases in channel gradient, at the mouths of tributaries. Over time the knickpoints have migrated upstream creating knickzones of rapidly incising channels, disconnected from their floodplains, with steep slopes that actively erode bluffs and ravines [*Gran et al.*, 2009, 2011b; *Belmont*, 2011; *Belmont et al.*, 2011]. Streams meander through low-gradient uplands above the knickzones, and are tributary to the low-gradient, meandering, mainstem Minnesota River downstream of the knickzones.

Around the time of European settlement in the mid-1800s, the Minnesota River Basin was dominated by tall-grass prairie and dotted with poorly drained wetlands [*Marschner*, 1974]. Beginning in the late 1800s, surface ditches were dug and subsurface drainage tiles were installed to drain wetlands and uplands for agriculture. As of 2007, agriculture accounted for around 90% of land-use in the basin [*Musser et al.*, 2009].

Wetlands that were once connected by subsurface flowpaths to the Minnesota River are now connected to the river by a vast network of drainage tiles and ditches, which has greatly changed the hydrologic connectivity of the basin and the rate at which water enters the river after rainfall. Late 19th century and early 20th century agricultural practices largely disturbed the landscape and increased sediment loads to the river network, initially by top-soil erosion. As soil-conservation practices improved and underground tile drainage expanded, sources of sediment shifted from upland fields to river banks and bluffs caused by increased streamflow due the combined effects of increased precipitation, crop conversions, and primarily amplified runoff from agricultural tile drainage [*Belmont et al.*, 2011; *Schottler et al.*, 2014].

2.4.2 Extraction of Network and Link Attributes its Spatial Heterogeneity

A 30-m DEM was downloaded in tiles covering the entire Minnesota River Basin from the U.S. Geological Survey (USGS) National Map with a coordinate system in the North American Datum of 1983 (NAD83) in decimal degrees and North American Vertical Datum of 1988 (NAVD88) in meters [*U.S. Geological Survey*, 2012]. Using ArcGIS, the tiles were mosaicked and projected into the Universal Transverse Mercator zone 15N (UTM15N) coordinate system. A drainage network was extracted for the Minnesota River Basin using ArcHydro tools in ArcGIS and a threshold area of 10 km^2. Although this threshold area is too large to extract all fluvial channels in the river network, the extracted network sufficiently captures the major fluvial channels and for simplicity, ignores the lowest order drainage ditches, whose initiation may not be based on a simple threshold area [*Passalacqua et al.*, 2012]. This produced a network of links each with attributes: index of link i, index of upstream link, index of downstream link, link length ℓ_i, directly contributing area a_i, and upstream drainage area A_i.

The elevation at the upstream and downstream end of each link was extracted from the underlying DEM, differenced, and divided by link length (channel path length) to determine the slope S_i of each link (Figure 2.3). The elevations extracted from the DEM for the river network represent the water surface and not the riverbed. The slope of the

water surface is equivalent to the slope of the riverbed under uniform flow conditions which is likely approximate for most of the network. However, around tributaries where there is backwater, the uniform flow assumption is violated, the slope of water surface is less than the slope of the riverbed, and the slopes obtained from elevations extracted from the DEM likely underestimate the slope of the riverbed. To account for this, specifically in the lower mainstem Minnesota River, all slopes less than 0.0001 were set to this value. However, if the adjusted slopes are actually much less than this value, then the simulated transport time through these links will be much faster than the actual transport time. For the Minnesota River Basin, the highest slopes in the network occur in the knickzones of tributaries entering the mainstem Minnesota River and in the northwestern part of the basin; between these regions are low-gradient uplands (Figure 2.3). The heterogeneity of slopes within the basin leads to non-uniform transport velocities, supporting the need for a spatially-explicit analysis of process response. Finally, all attributes were exported from ArcGIS and imported into MatLab for computing the sedimentological response.

2.4.3 Hydraulic Geometry Scaling

Hydraulic geometry scaling was based on field measurements from 23 USGS streamflow-gaging stations in the Minnesota River Basin (see Figure 2.2 for gage locations, [*U.S. Geological Survey*, 2014]). A representative bankfull flow at each gage was determined from a frequency analysis of annual peak flows, where bankfull flow was chosen as the two-year recurrence interval peak flow (Q_2 or two-year flow [L^3T^{-1}]) and determined as the daily streamflow that has a 50% chance of being exceeded in any year. Then the hydraulic characteristics ($u_{w,i}$ [LT^{-1}], H_i [L], and B_i [L]) at the Q_2 at each gage were obtained by regressing the measured hydraulic characteristics made during USGS streamflow measurements against streamflow, and taking the values of the hydraulic characteristics at the Q_2 (figures not shown). Downstream hydraulic geometry relations were developed by regressing the Q_2 with each hydraulic characteristic obtained at each gage for all 23 gages in the basin (Figure 2.4a-c).

The downstream hydraulic geometry relations for the Minnesota River Basin were obtained as:

$$B_i = (5.34)Q_{2,i}^{0.48}, \tag{2.31}$$

$$H_i = (0.321)Q_{2,i}^{0.42}, \tag{2.32}$$

and

$$u_{w,i} = (0.583)Q_{2,i}^{0.10}, \tag{2.33}$$

where $Q_{2,i}$ is specified in m^3/s, B_i in m, H_i in m, and $u_{w,i}$ in m/s. Typical exponents for these relations are 0.50, 0.40, and 0.10 for the $B_i \sim Q_{2,i}$, $H_i \sim Q_{2,i}$, and $u_{w,i} \sim Q_{2,i}$ scaling relations, respectively [*Leopold and Maddock*, 1953; *Park*, 1977], which are in close agreement with those of the Minnesota River Basin. It is noted that the velocity hydraulic geometry relation has a low coefficient of determination (R^2 = 0.12; Figure 2.4c), highlighting the spatial heterogeneity in this basin which calls for a spatially-explicit analysis. Additionally, the Q_2 was found to scale with upstream drainage area, A_i [L], (Figure 2.4d) as

$$Q_{2,i} = (1.4e-5)A_i^{0.70}, \tag{2.34}$$

where A_i is specified in m^2. Typically, this exponent is 0.75 and varies from 0.65 to 0.80 for bankfull flow [*Leopold et al.*, 1964], which is in close agreement with that of the Minnesota River Basin.

Combining the hydraulic geometry relations of equations (2.31-2.33) with equation (2.34) gives the scaling of hydraulic characteristics with upstream drainage area for the Minnesota River Basin as:

$$B_i = (0.024)A_i^{0.34}, \tag{2.35}$$

$$H_i = (0.0029)A_i^{0.29}, \tag{2.36}$$

and

$$u_{w,i} = (0.20)A_i^{0.07}, \tag{2.37}$$

where A_i is specified in m^2, B_i in m, H_i in m, and $u_{w,i}$ in m/s.

2.4.4 Intermittency Factor for Sand Transport

The intermittency factor for sand transport for the Minnesota River Basin was calculated at USGS streamflow-gaging station 05325000, Minnesota River at Mankato, Minnesota (see Figure 2.2 for gage location) and assumed to apply to the entire basin. The approach for determining the intermittency factor (first introduced by *Paola et al.* [1992]) follows the approach outlined by *Parker* [2004].

The volumetric transport rate of sand per unit width at the Q_2 (two-year [~bankfull] flow), $q_{s,b}$ [L^2T^{-1}], was computed using equations (2.8, 2.13, 2.10, and 2.11). Then the daily streamflow record at the Mankato gage was used to compute non-parametrically the ϕ^{th}–percentile daily streamflow, q_ϕ [L^2T^{-1}], and its corresponding probability of occurrence, p_ϕ. From q_ϕ, the volumetric transport rate of sand per unit width in the ϕ^{th} percentile, $q_{s,\phi}$ [L^2T^{-1}], was then computed for all ϕ percentiles using equations (2.8, 2.13, 2.10, and 2.11). Next, the mean annual volumetric transport rate of sand per unit width, $\overline{q}_s$ [L^2T^{-1}], was computed as

$$\overline{q}_s = \sum_\phi p_\phi q_{s,\phi} \,, \tag{2.38}$$

by summing the product $p_\phi q_{s,\phi}$ over all ϕ percentiles. Finally, the intermittency factor for sand transport, $I_{f,s}$, was computed as

$$I_{f,s} = \frac{\overline{q}_s}{q_{s,b}} \,. \tag{2.39}$$

For the Minnesota River at Mankato, the intermittency factor for sand was computed as $I_{f,s}$ = 0.175. This is the fraction of time per year that continuous Q_2 would yield the mean annual sand load.

2.4.5 Selecting a Characteristic Vertical Length Scale for Sand Transport

The characteristic vertical length scale for sand transport $(\theta_i H_i)$ is set by θ_i which

defines a fraction of the flow depth below which the "majority" of sand transport takes place. The "majority" can be defined quantitatively as capturing a certain percentage of the total sand load, which can be calculated as the product of the vertical distributions of suspended sediment and velocity. This analysis is specific to a single link i and for simplicity the index i has been dropped in this subsection.

The Rouse-Vanoni-Ippen suspended-sediment distribution [*Garcia*, 2008] is given by

$$\frac{\bar{c}}{\bar{c}_b} = \left[\frac{(H-z)/z}{(H-b)/b}\right]^{Z_R}, \tag{2.40}$$

where $\bar{c}$ [ML^3] is the suspended-sediment concentration averaged over turbulence at a distance z above the bed, $\bar{c}_b$ [ML^3] is the near-bed suspended-sediment concentration averaged over turbulence, H [L] is the flow depth, z [L] is the distance above the bed, b [L] is the near-bed distance above the bed, and Z_R is the dimensionless Rouse number given as

$$Z_R = \frac{\nu_s}{\kappa u_*}, \tag{2.41}$$

where ν_s [LT^{-1}] is the sediment fall velocity, κ = 0.41 is the von Karman's constant, and u_* [LT^{-1}] is the shear velocity. Sediment fall velocity was computed from the empirical relation of *Dietrich* [1982] as

$$R_f = \exp\left\{-b_1 + b_2 \ln(R_{ep}) - b_3\left[\ln(R_{ep})\right]^2 - b_4\left[\ln(R_{ep})\right]^3 + b_5\left[\ln(R_{ep})\right]^4\right\}, \tag{2.42}$$

where R_f is a dimensionless fall velocity

$$R_f = \frac{\nu_s}{\sqrt{gRD}}, \tag{2.43}$$

g = 9.81 m·s^{-2} [LT^2] is the acceleration due to gravity, R = 1.65 is the submerged specific gravity of sediment, D [L] is the sediment grain size, R_{ep} is a dimensionless particle Reynolds number

$$R_{ep} = \frac{\nu_s D}{\nu}, \tag{2.44}$$

$\nu = 1\times10^{-6}$ $m^2 \cdot s^{-1}$[L^2T] is the kinematic viscosity of water, and the coefficients are given as $b_1 = 2.891394$, $b_2 = 0.95296$, $b_3 = 0.056835$, $b_4 = 0.002892$, and $b_5 = 0.000245$ (as presented by *Garcia* [2006]). The shear velocity was calculated via the depth-slope product for the bed shear stress as

$$u_* = \sqrt{gHS}\,, \tag{2.45}$$

where S is the channel slope. For convenience, equation (2.40) can be rearranged as

$$\frac{\bar{c}}{\bar{c}_b} = \left[\frac{\left(\frac{1}{z/H} - 1\right)}{\left(\frac{1}{b/H} - 1\right)}\right]^{Z_R}, \tag{2.46}$$

which relates the relative concentration $\bar{c}/\bar{c}_b$ to the relative depth z/H where b/H = 0.05 [*Vanoni*, 1975].

The velocity distribution according to *Keulegan* [1938] is given by

$$\frac{u}{u_*} = \frac{1}{\kappa}\ln\left(30\frac{z}{k_s}\right), \tag{2.47}$$

where u [LT^{-1}] is the time-averaged flow velocity at a distance z above the bed and $k_s = 2D$ [L] is an effective roughness height [*Garcia*, 2008]. Rearranging, we can write equation (2.47) as

$$\frac{u}{u_*} = \frac{1}{\kappa}\ln\left[30\frac{(z/H)}{(k_s/H)}\right], \tag{2.48}$$

which relates the relative velocity u/u_* to the relative depth z/H.

In multiplying equation (2.46) by equation (2.48) we can compute a vertical distribution of the relative suspended-sediment load and take the cumulative sum of this distribution from the bed. Then θ_i can be computed directly from the cumulative distribution of relative suspended-sediment load (normalized so the maximum of the cumulative distribution is equal to one) as the vertical location which captures a certain percentage of the suspended-sediment load. Note that only the relative distributions are necessary and not the actual distributions because we only need to know, in a relative

sense, how much sediment is transported at various points throughout the water column.

For the study basin at the two-year recurrence interval flow and where D = 0.4 mm, the value of θ_i = 0.1 captures 73% of the total sand load on average for all links of the network (standard deviation of 18%). Similarly, say we wanted θ_i to capture 80% of the total sand load, then on average θ_i = 0.15 (standard deviation of 0.1), or for 90%, then on average θ_i = 0.23 (standard deviation of 0.14). Herein we maintain θ_i = 0.1 for all links.

2.4.6 Formulation of Travel Times

In this section, parameters of the sedimentological response function for mud, sand, and gravel (developed in section 2.3) are specified based on characteristics of the Minnesota River Basin.

2.4.6.1 Mud Response Function

Hydraulic geometry scaling relations for the Minnesota River Basin were developed at an approximate bankfull flow chosen as the two-year recurrence interval peak flow Q_2 or two-year flow (section 2.4.3) from which estimates were obtained for the parameters $\alpha_{u_{w}A}$ = 0.20, and $\beta_{u_{w}A}$ = 0.07 for the streamflow velocity scaling equation (2.4), and thus the characteristic velocity of mud transport, as

$$u_{w,i} = (0.20)A_i^{0.07}, \tag{2.49}$$

where A_i is specified in m^2 and $u_{w,i}$ in m/s.

The characteristic velocity scaling of equation (2.49) leads to the travel time scaling of

$$t_{w,i} = 5\ell_i A_i^{-0.07}, \tag{2.50}$$

where ℓ_i is specified in meters and thus $t_{w,i}$ in seconds. Summing the travel time along each pathway γ_i gives the pathway travel time $T_{w,i}$, which can be used to obtain the

PSWF for mud transport (streamflow) $W_w(t)$.

2.4.6.2 Sand Response Function

The characteristic velocity of sand for the Minnesota River Basin was obtained by substituting the parameters g = 9.81 m·s^{-2}, θ_i = 0.1 ($\forall i$; see section 2.4.5), R_i = 1.65 ($\forall i$), D_i = 0.0004 m ($\forall i$; D50 size of sand from riverbed material within the Minnesota River Basin [*U.S. Geological Survey*, 2014]), $\alpha_{u_{wA}}$ = 0.20, $\beta_{u_{wA}}$ = 0.07, α_{HA} = 0.0029, and β_{HA} = 0.29 (section 2.4.3; at Q_2 or two-year flow, where A_i is specified in m^2, H_i in m, and $u_{w,i}$ in m/s) into equation (2.16), which reduces the characteristic velocity of sand to

$$u_{s,i} = 0.32 A_i^{0.285} S_i^{3/2}, \tag{2.51}$$

where $u_{s,i}$ is specified in m/s. Substituting the intermittency factor $I_{f,s}$ = 0.175 (section 2.4.4) into equation (2.19) and incorporating equation (2.51) leads to the travel time scaling of

$$t_{s,i} = 18 \ell_i A_i^{-0.285} S_i^{-3/2}, \tag{2.52}$$

where again ℓ_i is specified in meters and thus $t_{s,i}$ in seconds. Summing the travel time along each pathway γ_i gives the pathway travel time $T_{s,i}$, which can be used to obtain the PSWF for sand transport $W_s(t)$.

2.4.6.3 Gravel Response Function

The gravel transport equation contains a threshold for transport (see equation 2.22 and 2.29); above the threshold, transport occurs and below the threshold no transport occurs. The flow is capable of transporting gravel when the dimensionless bed shear stress

$$\tau_{*,i} = \frac{H_i S_i}{R_i D_i} \tag{2.53}$$

exceeds the threshold value for initiation of motion $\tau_{*,i} > \tau_{*c,i}$, where $\tau_{*c,i} = 0.0495$ for the *Wong and Parker* [2006] gravel-transport formula. The proposed formulation for gravel response only exists if the transport threshold is exceeded everywhere in the basin (otherwise contributions from the basin can never be transported to the outlet). Therefore, the flow is capable of transporting gravel when, and the GIUS for gravel for the Minnesota River Basin only exists if,

$$S_i > \frac{\tau_{*c,i} R_i D_i}{\alpha_{HA}} A_i^{-\beta_{HA}} \tag{2.54}$$

for the Q_2. Considering the potential transport of sediment with a grain size of $D_i = 0.01$ m ($\forall i$; and the other parameters specified based on those given for the sand response function), the transport threshold is not exceeded everywhere in the basin for this formulation, and therefore, the gravel response function does not exist at the outlet of the basin at the Q_2. This suggests that this size gravel is not transported out of the Minnesota River Basin at or below the Q_2. For this reason, we do not go into further details about the gravel response and leave further investigations that consider spatially variable grain size, abrasion, and variable flow above the Q_2, for a future study.

However, mapping where the river system is capable of transporting gravel ($\tau_{*,i} - \tau_{*c,i} > 0$) would provide insight into potential transport and deposition areas of the network. While this map is not shown, the areas where the river system is capable of transporting gravel are those with the steepest slopes (Figure 2.3) in the knickzones of tributaries entering the mainstem Minnesota River and in the northwestern part of the basin. Gravel supplied to channels capable of transporting this material will eventually be transported downstream (and abrade or break down into smaller particles) until it reaches a channel that is not capable of transporting this material. These downstream channels are potential deposition reaches for gravel as any gravel supplied to it would accumulate at this location. Additionally, channels capable of transporting gravel are those with the greatest capacity for erosion and these channels may indicate potential sediment sources where the river is capable of recruiting bank material into the channel.

2.4.7 Best Estimate of the Rate of Total Sand Transport

Estimates of the rate of total sand transport were obtained from suspended-sediment measurements at 18 USGS streamflow-gaging stations in the Minnesota River Basin (see Figure 2.2 for gage locations) as follows. At each gage, suspended-sediment concentration and sand fraction, if not a full grain-size distribution, was measured along with streamflow at different instants of time and flows [*U.S. Geological Survey*, 2014]. Suspended-sediment concentration and sand fraction at the two-year recurrence interval peak flow (Q_2) was estimated from the measurements at each gage. For the majority of sites, approximately 30% of the measured suspended sediment was sand at the Q_2. The rate of suspended-sand transport at the Q_2 was computed by multiplying the suspended-sediment concentration by the sand fraction and the Q_2 streamflow. The rate of total sand transport at the Q_2 was then computed following the method of *Shah-Fairbank et al.* [2011] (and using the method of *Guo and Julien* [2004] to compute the Einstein integrals) from the rate of suspended-sand transport at the Q_2, bed shear stress (estimated from Q_2 and channel dimensions), suspended-sediment fall velocity (estimated using the equation of *Ferguson and Church* [2004] and measured D50 sand size in suspension, ~0.15 mm [*U.S. Geological Survey*, 2014]), and D65 of bed material (from bed-material measurements at gages, ~1 mm [*U.S. Geological Survey*, 2014]). In the end, this method generally estimated the rate of total sand transport at the Q_2 equal to approximately 120% of the measured rate of suspended-sand transport at the Q_2, and represents the best estimate of the observed rate of total sand transport (including both suspended and bedload transport) at the Q_2 from suspended-sediment measurements at gages.

2.5 GIUS of the Minnesota River Basin

The proposed formulation of the GIUS describes how sediment with grain size D_i instantaneously released and uniformly distributed over the basin would propagate (below transport capacity) through the river system to the basin outlet. We repeat that the present formulation only considers storage (time delays) for sediment on the bed or on bars that are readily mobilized by the next capable flow. Long-term storage of sediment due to floodplain deposition or meander migration over a bar that is re-entrained when the river sweeps back across the floodplain is not considered at present. Thus the proposed GIUS provides a lower bound on the fastest timescale for sediment to transport from different parts of the basin to the outlet. This is in contrast to the prodigious research on sediment pulses in rivers, where an emplaced pulse of sediment exceeds transport capacity and largely disperses in place [*Lisle et al*., 1997, 2001; *Cui et al*., 2003a, 2003b; *Cui and Parker*, 2005; *Lisle*, 2008; *Sklar et al.*, 2009].

This section includes a description of the GIUS of the Minnesota River Basin, an evaluation of its robustness to model parameter uncertainty, and a diagnostics/validation analysis of the GIUS for sand using suspended-sediment data.

2.5.1 Description of the GIUS

The pathway distance from each link to the outlet was grouped into 7 bins to show the correspondence between the river network of the Minnesota River Basin and its WF (Figure 2.5a-b). The first two contributions to the WF (corresponding to areas at distances 0-100 and 101-200 km from the outlet in Figure 2.5a-b) are small which is reflected in the narrow width of the Minnesota River Basin near the outlet. The two peaks of the WF (corresponding to areas at distances 301-400 and 501-600 km from the outlet in Figure 2.5a-b) reflect the widest regions of the Minnesota River Basin and result from the structure of the network, where many links are within these distances from the outlet.

The WF generated using 100 bins maintains the large-scale structure of the 7-bin WF but now conveys smaller-scale information on the network structure (Figure 2.5c).

Three distinct regions of the WF emerge: a narrow region (between normalized distance 0 and 0.3), a central region (between normalized distance 0.3 and 0.7), and a distant region (between normalized distance 0.7 and 1) (Figure 2.5c). Each region reflects contributions from different areas of the Minnesota River Basin. The PSWF or GIUS can be thought of as a WF generated from a network of pathway travel times rather than from a network of pathway distances. In this way, scaling link lengths by a characteristic velocity transforms the pathway-distance network non-uniformly into a pathway travel-time network.

The GIUS for mud (streamflow) (Figure 2.5d) is similar in shape to the WF because the characteristic velocity for mud transport (streamflow velocity) weakly increases with drainage area (to the 0.07 power; equation 2.49). If the characteristic velocity for mud transport was a constant throughout the basin, then the GIUS would be a linearly scaled version of the width function. However, because the characteristic velocity increases downstream, the pathway travel-time network is similar to the pathway-distance network except for proportionally longer upstream links and shorter downstream links. The non-linear scaling increases the delay of contributions from upstream links and decreases the delay from downstream links compared to the WF. The scaling of the GIUS for mud spreads out the link contributions which slightly reduces the peaks of the GIUS for mud compared to the WF.

The GIUS for sand (Figure 2.5e) is significantly different from the WF with peaks concentrated at a normalized distance of 0.3 and 0.7. Substituting the scaling relation for the channel slope, obtained from the 30-m DEM as

$$S_i = (0.30) A_i^{-0.31}, \tag{2.55}$$

into equation (2.51), simplifies the characteristic velocity for sand transport as a constant times the drainage area to the -0.18 power,

$$u_{s,i} = 0.05 A_i^{-0.18}. \tag{2.56}$$

Therefore, the characteristic velocity generally decreases downstream resulting in a pathway travel-time network with proportionally shorter upstream links (decreased delay of contributions) and longer downstream links (increased delay of contributions)

compared to the pathway-distance network. Contributions from upstream links more quickly enter downstream links, which concentrate the contributions from upstream links and increase the peaks of the GIUS for sand compared to the WF. The structure of the sand response truly arises from the network topology, channel slopes, and sand-transport formulation.

2.5.2 Robustness and Validation of the GIUS for Sand

The timing of the GIUS for sand is highly sensitive to three parameters (D_i, θ_i, and $I_{f,s}$) which appear as linear multipliers in equation (2.19) and therefore uniformly shift the timing of the overall response, without however affecting the shape of the response. The GIUS for sand has been computed using the D50 sand size of D_i = 0.4 mm from riverbed material within the Minnesota River Basin (Figure 2.5e, *U.S. Geological Survey* [2013]). If instead the sand has a different median size, e.g., D_i = 0.3 or 0.5 mm, the timing of the response function changes such that, rather than obtaining peaks at 90 and 265 years (D_i = 0.4 mm), the peaks would occur at 70 and 200 years (D_i = 0.3 mm) or 115 and 330 years (D_i = 0.5 mm). Thus, there is an uncertainty in the timing of the peaks of the GIUS due to uncertainty in the choice of D_i, θ_i, and $I_{f,s}$.

The shape of the GIUS for sand is only affected through the exponents on the upstream drainage area A_i and slope S_i (see equations 2.19 and 2.51) that contribute to the transport time in a non-linear way to rearrange contributions to the GIUS for sand (Figure 2.6). The exponent of the upstream drainage area was varied from 0 to 0.5 and the exponent of slope was varied from 0 to 5/2 (Figure 2.6). Note that the exponents of zero correspond to the width function (Figure 2.6m; A^0S^0), which for different parameters, resulting from the specific transport dynamics, stretches to become the sand response function (Figure 2.6g; $A^{0.285}S^{3/2}$). Increasing the exponent on the upstream drainage area tends to smooth out the contributions to the response, whereas increasing the exponent on slope tends to concentrate contributions into peaks. For most of the

variations in the exponents of the sand response function, the two peaks in the GIUS remain, although shifted, suggesting that bimodality is a relatively robust property of the GIUS for sand for the Minnesota River Basin.

As an attempt to validate the formulation of the GIUS for sand, the best estimate of the rate of total sand transport at the two-year flow Q_2 ("observed"; see section 2.4.7, approximately 120% of the rate of measured suspended-sand transport at the Q_2) was compared to the simulated rate of total sand transport at the Q_2 ("simulated") (Figure 2.7) computed as

$$Q_{s,i} = \frac{0.05}{g^{1/2} R_i^2 D_i} u_{w,i}^2 H_i^{3/2} B_i S_i^{3/2}. \tag{2.57}$$

A few measurements show good agreement between the simulated and observed rates of total sand transport; however, most simulated rates are an order of magnitude larger than the observed rates (Figure 2.7). When comparing the relative differences between the simulated and observed transport rates with the upstream drainage area (Figure 2.7b), the best agreement occurs at sites with large drainage areas and at a few sites with small drainage areas. Note that the simulated $Q_{s,i}$ represents at-capacity transport whereas the observations take into account the actual sediment supply. It is possible that the large discrepancy between rates indicates that the transport formula or parameters used in the transport formula are not appropriate, but we suggest that this comparison may identify supply-limited versus transport-limited parts of the basin. Some upstream parts of the basin might be supply limited (simulated sand-transport capacity >> observed transport), and at downstream links, homogenization of spatial and temporal variability may take place leading to transport-limited conditions (simulated sand-transport capacity = observed transport), which might indicate a potential for storage as any sediment supplied above capacity would go into storage. Nonetheless, where sediment supply may not be a limiting factor, there is relatively good agreement (within an order of magnitude) between the simulated and observed rates of total sand transport.

2.6 Partitioning Contributions to the Sedimentological Response

The GIUS is a system property and represents the response of the system to a spatially uniform input of sediment. Typically, the sediment input in such a large basin would vary spatially and temporally and this would require convolving partitioned and scaled versions of the GIUS to realize the observed sedimentological response at the outlet of the basin. We illustrate how the GIUS can be partitioned and scaled into a sedimentological response by considering a mixture of sediment and contributions from subbasins of the Minnesota River Basin.

The GIUS is specified for a specific grain size, such as the D50 sediment size, but in reality a mixture of sediment sizes is transported concurrently by the river network. Considering the grain-size distribution of sand on the riverbed within the Minnesota River Basin (inset Figure 2.8; [*U.S. Geological Survey*, 2014]), a GIUS for sand can be generated for each individual size, scaled according to relative abundance in the grain-size distribution, and then added together across sizes to obtain the combined response (Figure 2.8). Under the assumption that individual grain-size fractions sort during transport such that the transport of each fraction can be simply treated individually as a response and added together to obtain the combined response (which may not be accurate due to hiding effects [*Wilcock and Crowe*, 2003]), the combined response reflects the GIUS for the mode of the grain-size distribution.

The framework developed herein allows partitioning of the contributions to the GIUS based on any attributes of the geomorphic state, e.g. different subbasins which might have distinct features or sediment contributions. The Minnesota River Basin was partitioned here into two subbasins: the Blue Earth River Basin and the rest of the basin to disentangle the contribution of each to the GIUS at the outlet of the basin (Figure 2.9). During 2002–2006, the Blue Earth River Basin contributed over 50% of the sediment supply to the Minnesota River Basin despite the fact that it only accounts for roughly 20% of the total area [*Wilcock*, 2009]. Therefore, sediment contributions from the Blue Earth River Basin to the GIUS are expected to be larger than from other areas of the

Minnesota River Basin. It is seen from Figure 2.9b that the partitioned contribution from the Blue Earth River Basin to the GIUS for mud corresponds to the central region of the response between normalized distance 0.3 and 0.7. The partitioned contribution from the Blue Earth River Basin to the GIUS for sand concentrates into the first peak at a normalized distance of 0.3 (Figure 2.9c). It is important to note that scaling of the network topology based on the sand-transport process has shifted the contribution of the Blue Earth River Basin from the central region of the WF to the first peak of the GIUS for sand. This highlights that non-linear spatial stretching of the network topology based on the sediment-transport process rearranges contributions to the GIUS in unexpected ways compared to the contributions to the WF.

2.7 Amplification of the Sedimentological Response

As demonstrated in the previous sections, the shape of the GIUS of a basin carries the signature not only of the river network topology but also of the specific hydraulic and stream morphologic characteristics of the channels. As a result, the peak contributions at the outlet of a basin arise from the superposition of inputs that arrive at the outlet from disparate, and even unconnected, parts of the basin. Given the long response times of sediment transport in rivers, which may be of the order of hundreds or thousands of years, one could envision changes occurring in parts of the basin at decadal or longer time scales and the associated response progressing downstream and superimposing on past responses in such a way that leads to unexpected amplifications. In this section we demonstrate this idea using the Minnesota River Basin and its sedimentological response for sand.

Suppose a landscape disturbance event occurs which delivers an instantaneous input of sand (0.4 mm) uniformly over the entire basin at a time $t = 0$ years (d1; Figure 2.10a). Such an event may be extreme precipitation, which detaches sediment and the resulting overland flow entrains and delivers this sediment directly to the river network. This was likely a common mechanism during the late 19th century and early 20th century when agricultural practices largely disturbed the landscape and left the top soil exposed

and vulnerable to erosion. Extreme precipitation may also lead to very high streamflow capable of eroding and recruiting bank material into the channel. This is likely the most common mechanism today for delivering sand to the river network as soil-conservation practices have greatly improved and underground tile drainage has expanded [*Belmont et al.*, 2011].

The sedimentological response at the outlet of a basin for the disturbance event at t = 0 years (d1) is the GIUS for sand for the Minnesota River Basin (dashed line; Figure 2.10b). It is seen that the structure of the GIUS exhibits two peaks which arise from the network topology, channel slopes, and sand-transport formulation. The two prominent peaks suggest that there is a resonant frequency of sediment supply that would lead to an amplification of the response. Given regularly occurring sediment-transporting flows/events, two peaks are manifested in the response at 90 and 265 years (Figure 2.10b). If another landscape disturbance event occurs 175 years after the first which delivers an instantaneous input of sand (0.4 mm) uniformly over the entire basin at a time t = 175 years (d2; Figure 2.10a), the additional contribution to the sedimentological response will be similar to the first but shifted in time (Figure 2.10c). This assumes that disturbance events (or events that deliver sediment) are less frequent than those that transport the sediment through the river network [*Lane et al.*, 2008]. The observed response at the outlet of the basin (Figure 2.10d) is the superposition of the individual responses (Figure 2.10b-c) leading to an amplified sedimentological response, with a greatly increased peak at 265 years and a relatively long duration of high contributions from 250 to 280 years after the initial disturbance (Figure 2.10d). Conceptually, this suggests a 175-year resonance time (resonant frequency with a period of 175 years) for sand (0.4 mm) for the Minnesota River Basin.

While the GIUS conceptualizes the sedimentological response to a uniformly distributed disturbance and input to the river network, in reality these disturbances are more localized within the basin. Amplification of the sedimentological response can still occur if only specific source areas are disturbed instead of the entire landscape. For instance, if the first disturbance event (d1; Figure 2.10a) only disturbed a northwest region of the basin (A; Figure 2.10e) the sedimentological response would be only a

portion (the second peak) of the GIUS (shaded area; Figure 2.10b). If the second disturbance event (d2; Figure 2.10a) only disturbed the Blue Earth River Basin (C; Figure 2.10e) the sedimentological response would be only the portion (the first peak) of the GIUS (shaded area; Figure 2.10c). These seemingly isolated disturbances (in both space and time), would be ordered, delayed, and superimposed into an observed and unexpectedly amplified sedimentological response at the outlet of the basin (shaded area; Figure 2.10d).

When amplification of the sedimentological response occurs, likely there is an interaction between the two peaks that is not simply the sum of the two peaks. If the increased sediment supply to a channel is below the transport capacity, then the supply is transported downstream without a change in channel characteristics (change in channel slope or width). However, if the increased sediment supply overwhelms the transport capacity, which is likely the case, then the channel will aggrade and the change in channel characteristics will act to filter and reduce the peak of the increased sediment supply. Detailed process-based, reach-scale, sediment-transport models are best suited to quantify the specifics of the reach-scale changes due to increased sediment supply. However, this conceptual framework complements detailed process-based approaches by illuminating how inputs of sediment to the river system are structured by the river network and delayed in time due to the sediment-transport process.

The amplification of the sedimentological response could result in greater than expected aggradation of the bed of the river leading to disruption in ecosystem function, increased flood risk, and increased cost associated with remediation. Therefore, the proposed framework has identified an important vulnerability of the Minnesota River Basin to spatial and temporal changes in the basin and suggests that aggregated effects need to be seen within a whole-network framework and not in isolation.

2.8 Concluding Remarks

In this chapter we presented a connectivity-based conceptual framework of environmental response, focusing on the sedimentological response for mud, sand, and gravel. The proposed framework relies on performing a non-linear process-based scaling of the network geometry (link lengths) to convert the network width function into a time response function or process-scaled width function (PSWF) where the process of interest is sediment transport. The process-scaled width function for sediment is the geomorphologic instantaneous unit sedimentograph (GIUS) or the sedimentological response of a basin to an instantaneous unit volume of sediment uniformly entering all links of the network. The proposed framework was applied to the Minnesota River Basin to aid in understanding its long-term sedimentological response to spatially and temporally varying changes in the landscape.

It was shown that the network topology and sediment transport dynamics in the Minnesota River Basin combine to produce a double peaked response function for sand, suggesting that there exists a resonant frequency of sediment supply that could lead to an unexpected downstream amplification of sedimentological response. The two peaks of the sand response function can be attributed to specific areas of the basin, highlighting that the disturbance of one region followed by the disturbance of another region after a certain period of time, may result in an amplification of the effects of the sediment inputs that is otherwise difficult to predict with mechanistic short-time horizon models. The synchronization and amplification of sediment delivery in specific places of a basin may result in greater than expected aggradation of the riverbed triggering disruption in ecosystem functioning, and leading to increased flood risk and increased cost associated with remediation. Therefore, the proposed framework has identified an important vulnerability of the Minnesota River Basin to spatial and temporal structuring of sediment delivery, and can aid in understanding how climatic trends and current and future management decisions may be unexpectedly superimposed on this landscape as it undergoes intensive human management while it is still adjusting to past geologic disturbances.

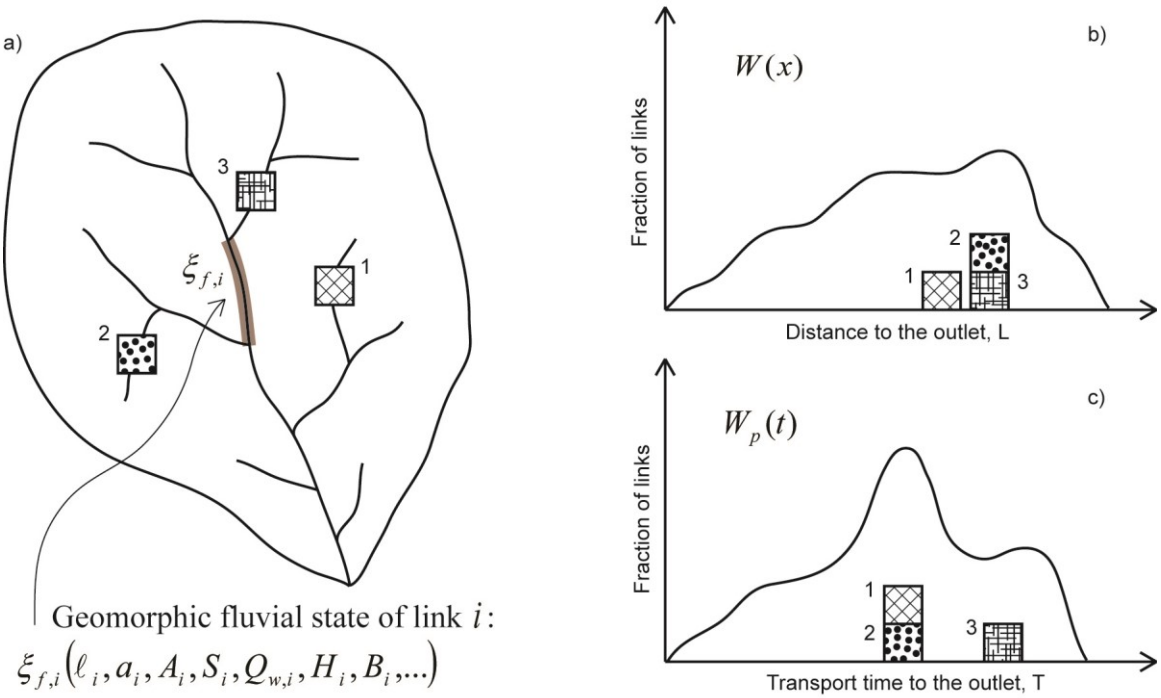

Figure 2.1. Conceptual framework of environmental response. (a) Illustration of a river basin with fluvial channel network. The highlighted segment of the network is a link i corresponding to geomorphic fluvial state $\xi_{f,i}$ with associated attributes. Areas of the basin, such as 1, 2, and 3, sitting at a certain distance from the outlet contribute to (b) a specific structure of the width function $W(x)$. (c) The contribution of these areas to the outlet may be redistributed in the process-scaled width function $W_p(t)$ based on the characteristics of the process of interest. The resulting environmental response function is a complex transformation of the original width function that depends on the river network topology and the attributes of the geomorphic fluvial states $\xi_{f,i}$ for all i links.

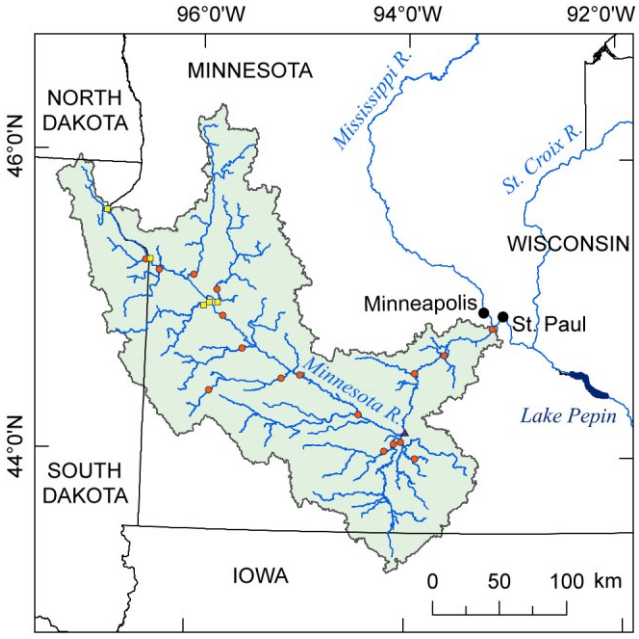

Figure 2.2. Location map of the Minnesota River Basin. Twenty-three U.S. Geological Survey (USGS) streamflow-gaging stations (circles, squares, and triangle) used in the hydraulic geometry scaling analysis (see section 2.4.3), USGS streamflow-gaging station 05325000, Minnesota River at Mankato, Minnesota (triangle) used in estimating the intermittency factor for sand transport (see section 2.4.4), and 18 USGS streamflow-gaging stations (circles and triangle) used in estimating the rate of total sand transport from suspended-sediment measurements (see section 2.4.7).

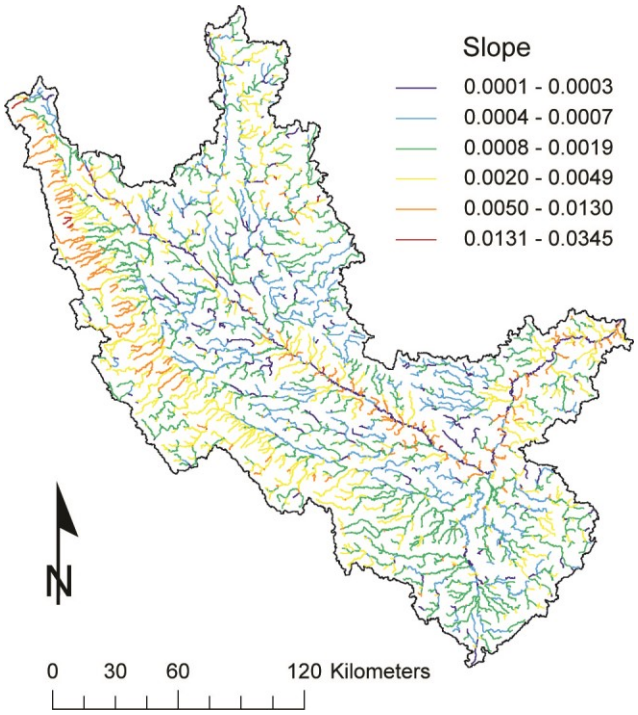

Figure 2.3. Slope of each link in the network. Highest slopes occur in the knickzones of tributaries entering the mainstem Minnesota River and in the northwestern part of the basin. Note that slopes less than 0.0001 were set to this value; this occurred primarily along the lower mainstem Minnesota River. The spatial distribution of link slopes vividly illustrates the geologic legacy of this basin with important implications for spatially variable sediment generation and transport.

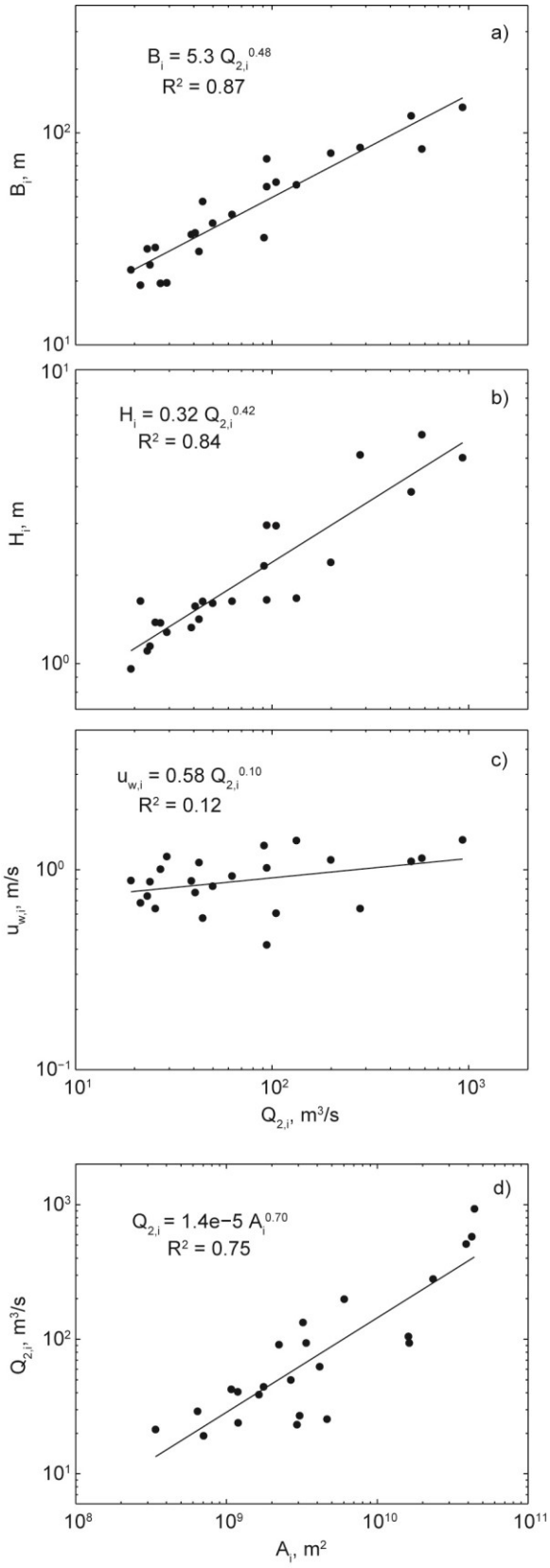

Figure 2.4. Hydraulic geometry scaling based on field measurements at 23 U.S. Geological Survey streamflow-gaging stations in the Minnesota River Basin (see Figure 2.2 for gage locations) of (a) channel width, (b) flow depth, and (c) streamflow velocity versus the two-year recurrence interval peak flow (obtained from a frequency analysis of annual peak flows for each station). (d) Scaling of the two-year recurrence interval peak flow versus drainage area.

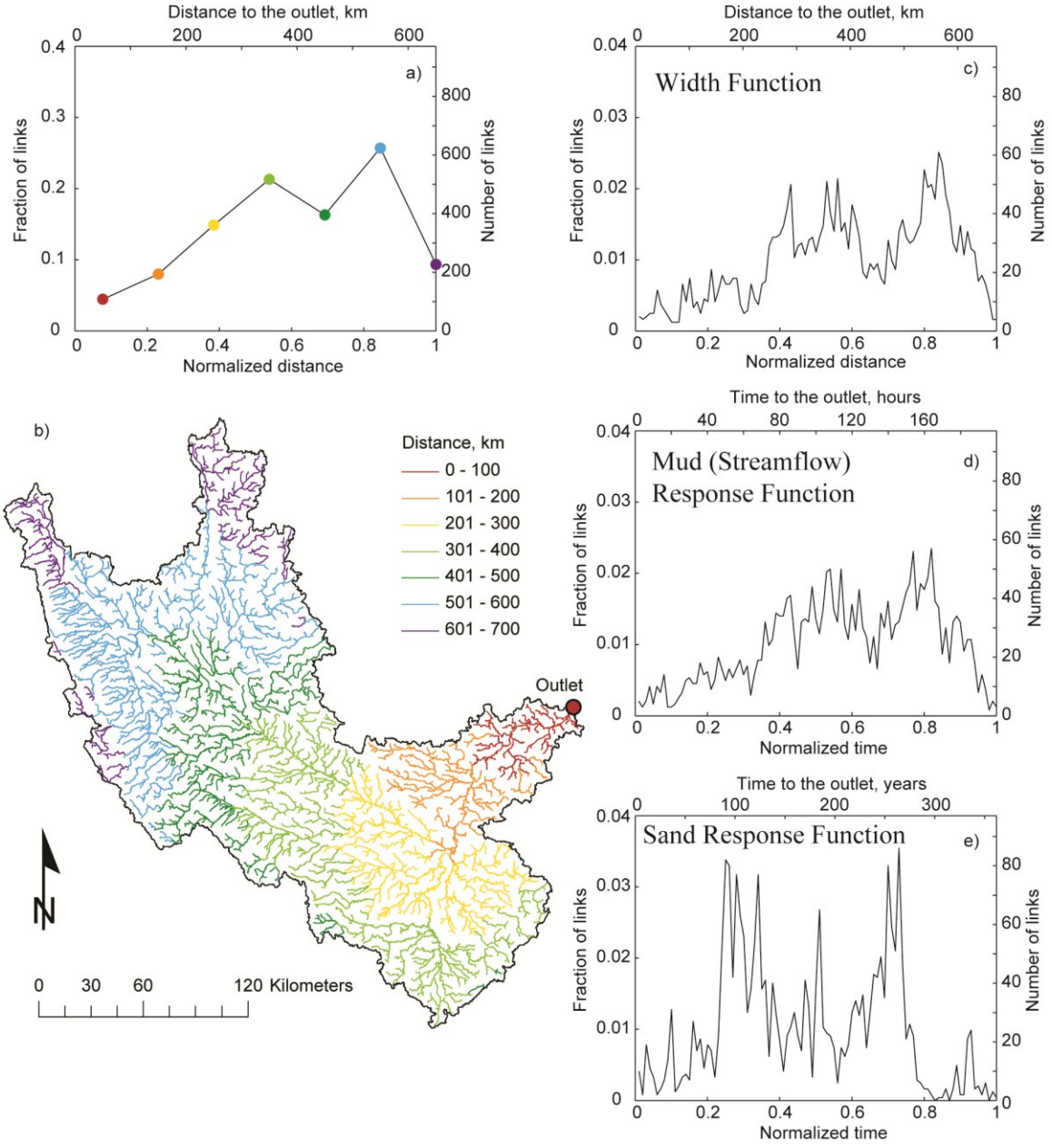

Figure 2.5. Width function and process-scaled width functions of the Minnesota River Basin. (a) Width function within 7 discretized distance bands of the Minnesota River Basin corresponding to the (b) map of distances from each link to the outlet. (c) Width function within 100 discretized distance bands showing more fine-scale detail. (d) Process-scaled width function or geomorphic instantaneous unit sedimentograph for mud (streamflow). (e) Process-scaled width function or geomorphic instantaneous unit sedimentograph for sand (0.4 mm).

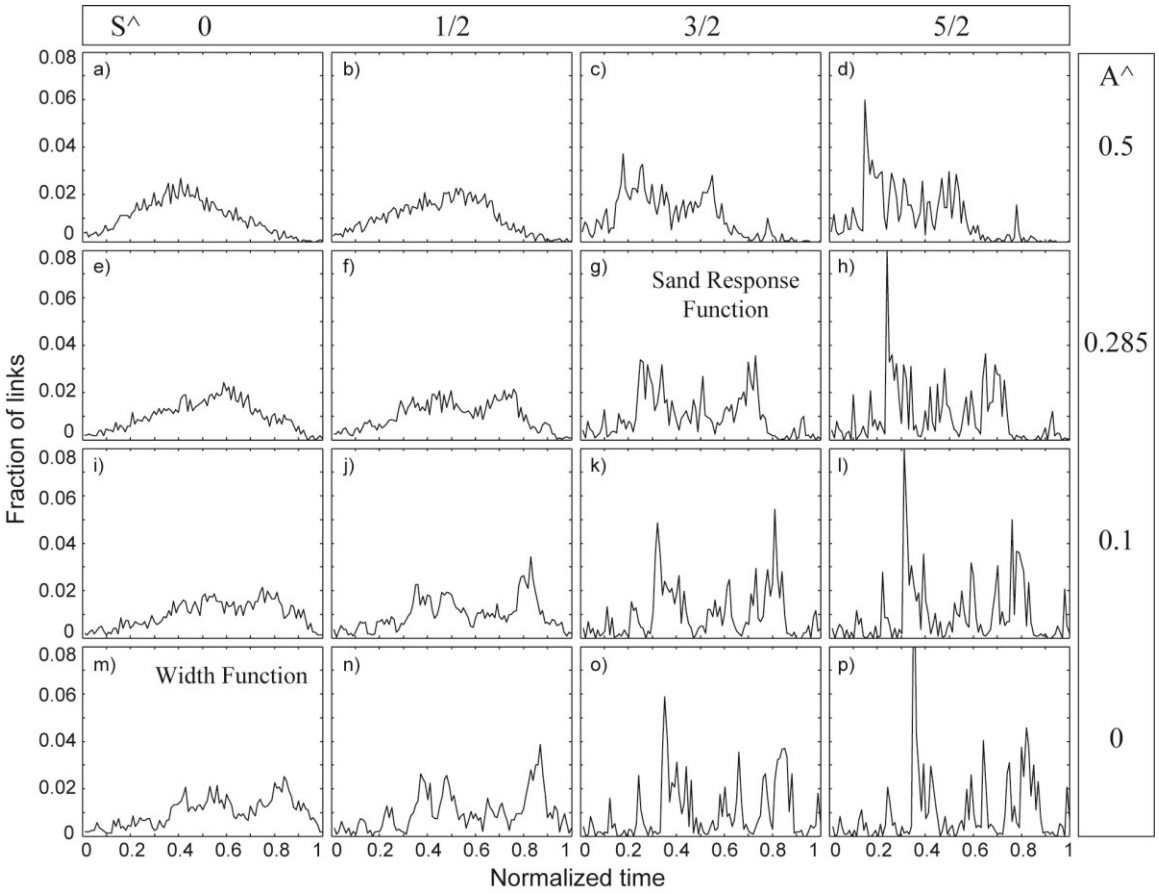

Figure 2.6. Sensitivity of the shape of the sand response function (geomorphologic instantaneous unit sedimentograph, GIUS). The sand response function arises from a characteristic velocity scaling $\sim A^{0.285}S^{3/2}$ (panel g; see equation 2.51) due to the exponents on upstream drainage area and slope that rearrange contributions to the GIUS for sand compared to the width function (panel m; A^0S^0). The exponent of upstream drainage area was varied from 0 to 0.5 (increases vertically) and the exponent of slope was varied from 0 to 5/2 (increases horizontally). Note that for most of the variations in exponents around the sand response function (panel m) the two peaks in the GIUS remain, although shifted, suggesting that this is a relatively robust property of the GIUS for sand for the Minnesota River Basin.

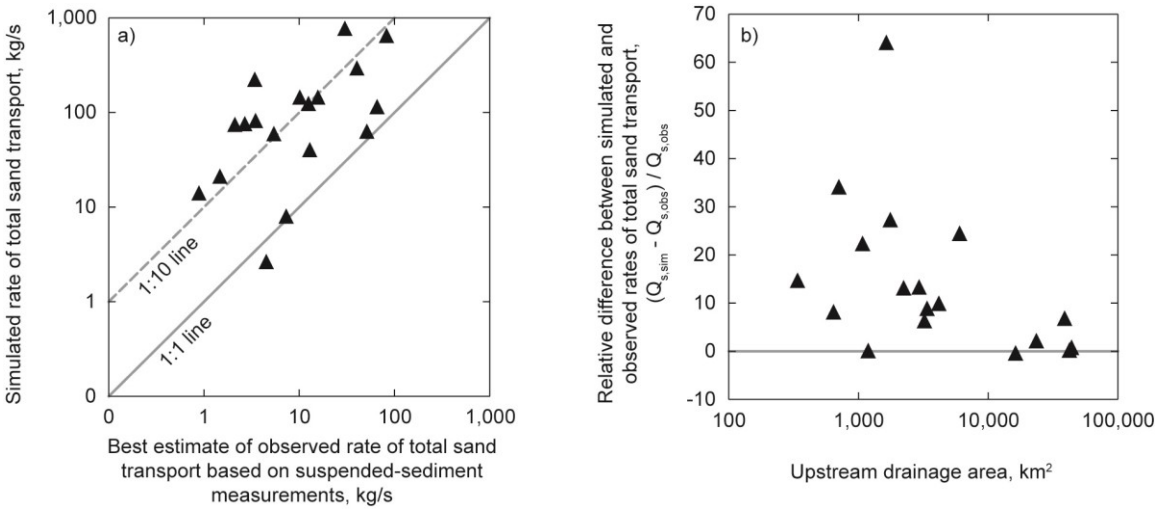

Figure 2.7. Comparison of the observed to simulated rates of total sand transport. (a) The best estimate of the rate of total sand transport at the Q_2 ("observed"; see section 2.4.7, approximately 120% of the measured rate of suspended-sand transport at the Q_2) was compared to the simulated rate of total sand transport at the Q_2 ("simulated"; see equation 2.57). (b) Relative difference between simulated and observed rates of total sand transport compared to upstream drainage area. Note that the simulated rate of total sand transport represents at-capacity transport, independent of sediment supply, whereas the observations take into account spatially variable sediment supply as well as transported-limited behavior in the system. Likely this comparison identifies supply-limited (large discrepancy) versus transport-limited (small discrepancy) parts of the basin.

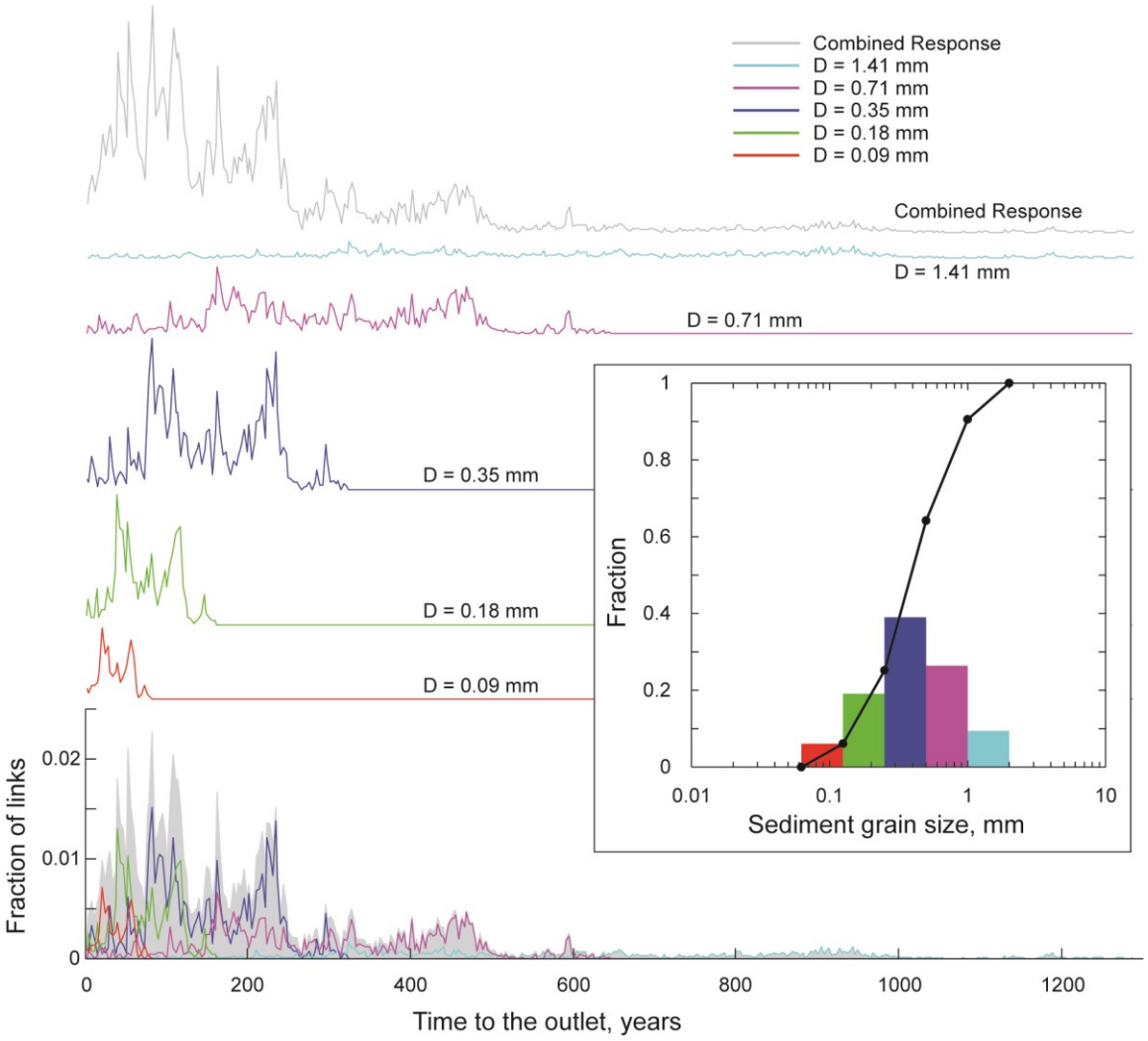

Figure 2.8. The geomorphologic instantaneous unit sedimentograph (GIUS) for the grain-size distribution of sand on the riverbed within the Minnesota River Basin (see inset for grain-size distribution). The GIUS for the sand distribution was generated for each individual size, scaled according to relative abundance in the grain-size distribution, and then added together across sizes to obtain the combined response. Individual size responses and the combined response are offset vertically for ease of comparison. Note that the combined response reflects the GIUS for the mode of the grain-size distribution.

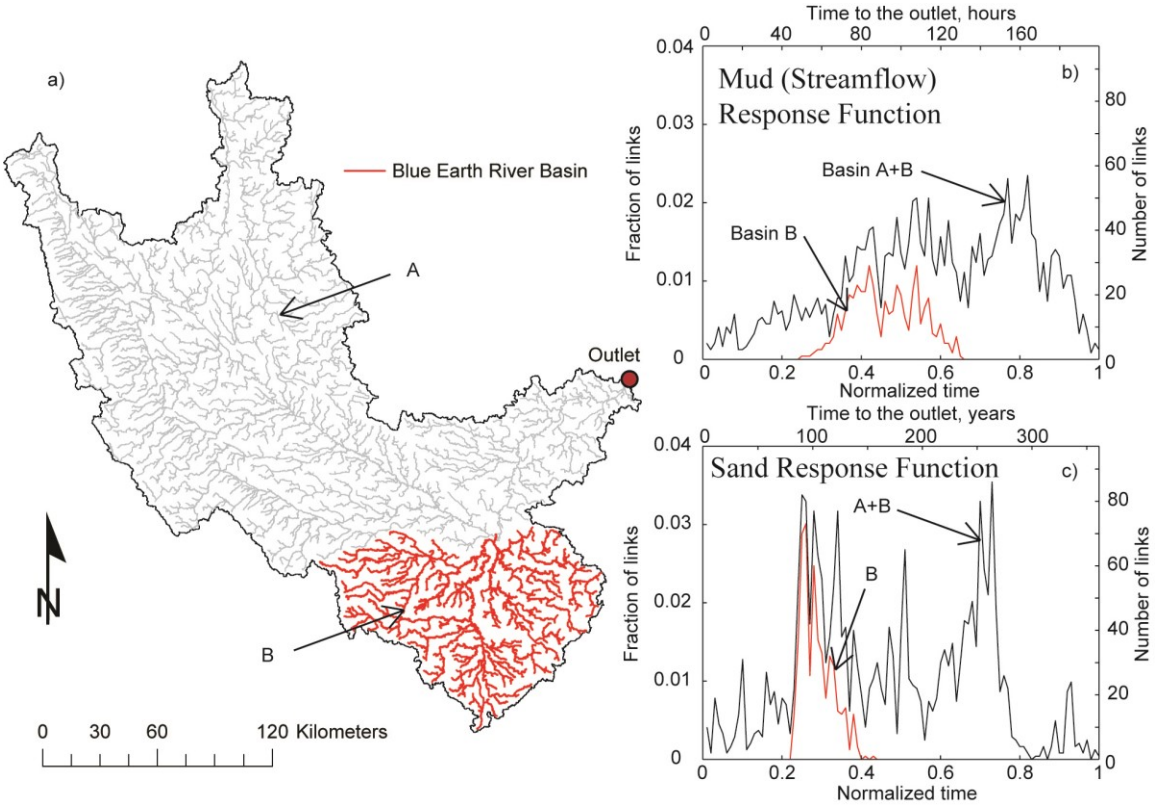

Figure 2.9. Partitioning contributions to the sedimentological response highlights critical sediment source areas. (a) The partition of the Blue Earth River Basin (B) and the rest of the basin (A). (b) Sedimentological response for mud for the entire basin (A+B) and for the Blue Earth River Basin (B). (c) Sedimentological response for sand (0.4 mm) for the entire basin (A+B) and for the Blue Earth River Basin (B).

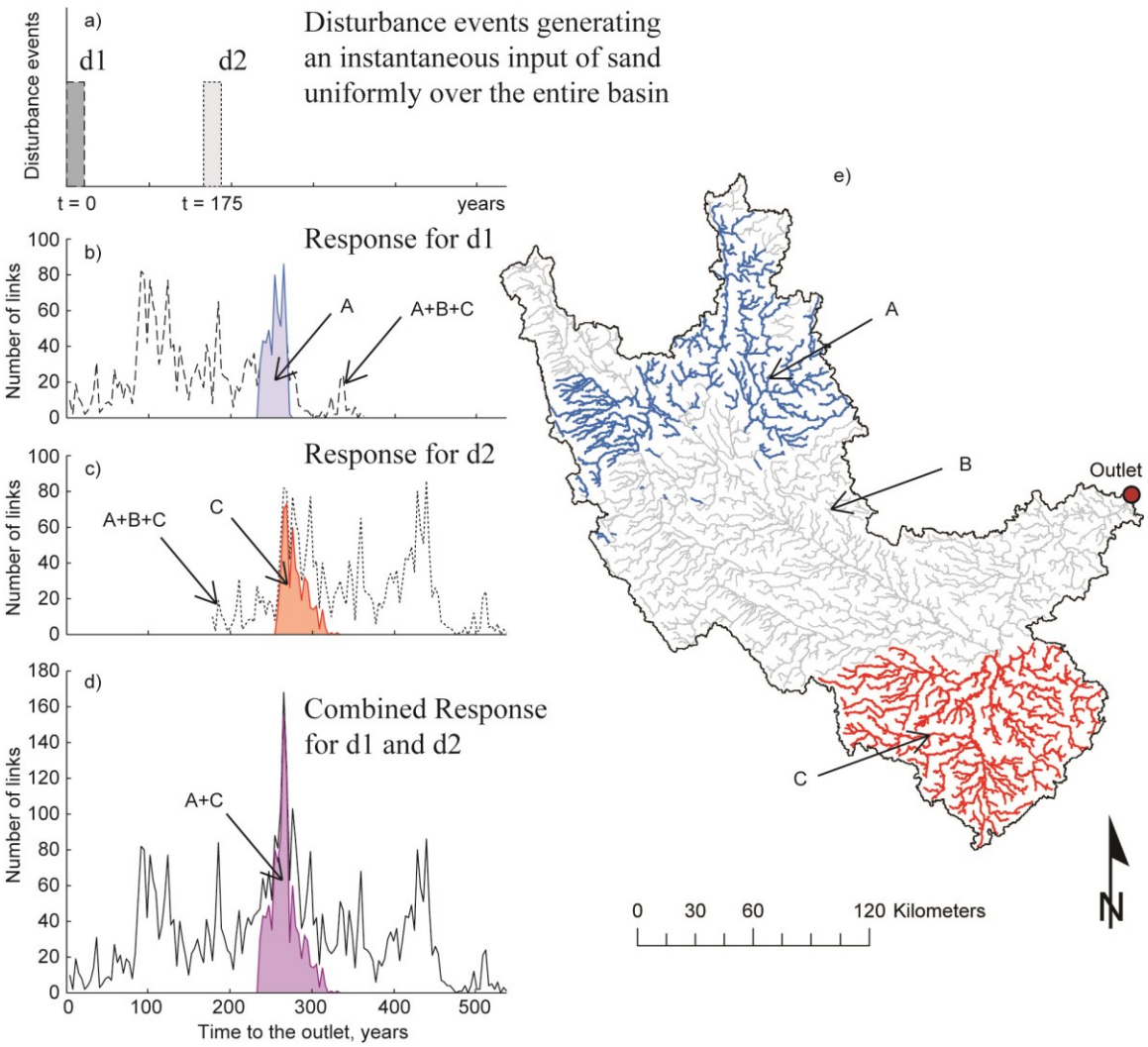

Figure 2.10. Synchronization of sediment fluxes can lead to amplification of the response for the Minnesota River Basin. (a) Disturbance of the landscape leading to two instantaneous inputs of sand (0.4 mm; uniformly over the basin) at 0 years (disturbance 1 or d1) and 175 years (disturbance 2 or d2). (b) Sedimentological response corresponding to d1; entire basin response [dashed line; basins A+B+C in (e)] and region corresponding to the second peak of the sand response [shaded area; basin A in (e)]. (c) Sedimentological response corresponding to d2; entire basin response [dotted line; basins A+B+C in (e)] and Blue Earth River Basin [shaded area; basin C in (e)]. (d) Superimposed response for sand [sum of (b) and (c)] into an observed response (line) resulting in amplification of the effects of the sediment inputs. (caption continued on next page)

(caption for Figure 2.10 continued) Amplification can also occur if only the regions contributing to the peaks of the response [basin A in (b) and basin C in (c)] are disturbed and responses superimposed [shaded area; A+C]. (e) Partition of the basin into 3 regions: the region corresponding to the first peak of the sand response (C, Blue Earth River Basin), second peak of the sand response (A), and the rest of the basin (B).

Chapter 3

Dynamic Connectivity in a Fluvial Network for Identifying Hotspots of Geomorphic Change

Dynamical processes occurring on the hierarchical branching structure of a river network tend to heterogeneously distribute fluxes on the network, often concentrating them into "clusters," i.e., places of excess flux accumulation. Here, we put forward the hypothesis that places in the network predisposed (due to process dynamics and network topology) to accumulate excess sediment over a considerable river reach and over a considerable period of time reflect locations where a local imbalance in sediment flux may occur thereby highlighting a susceptibility to potential fluvial geomorphic change. We develop a dynamic connectivity framework which uses the river network structure and a simplified Lagrangian transport model to trace fluxes through the network and integrate emergent "clusters" through a cluster persistence index (CPI). The framework was applied to sand transport in the Greater Blue Earth River Network in the Minnesota River Basin. Three hotspots of fluvial geomorphic change were defined as locations where high rates of channel migration were observed and places of high CPI coincided with two of these hotspots of possibly sediment-driven change. The third hotspot was not identified by high CPI, but instead is believed to be a hotspot of streamflow-driven change based on additional information and the fact that high bed shear stress coincided with this hotspot. The proposed network-based dynamic connectivity framework has the potential to place

dynamical processes occurring at small scales into a network context to understand how reach-scale changes cascade into network-scale effects, useful for informing the large-scale consequences of local management actions.

3.1 Introduction

River basins are drained by networks of hierarchically connected channels which serve as the primary pathways for transport of environmental fluxes. The branching network structure (defined here by the network topology and its associated geometry, i.e., link lengths) serves as a template upon which environmental fluxes of water, sediment, nutrients, etc. are conveyed and organized both spatially and temporally within the basin. It has been recognized that the river network plays a central role in structuring ecosystem processes and functions by heterogeneously distributing fluxes on the network often leading to critical places and times where excess fluxes accumulate or altered system functionality emerges [e.g., *Benda et al.*, 2004a; *Campbell Grant et al.*, 2007; *Carrara et al.*, 2012; *McCluney et al.*, 2014]. This emergent behavior is difficult to predict with reductionist approaches, e.g., too detailed, fine resolution, small spatial and temporal extent, and over-parameterized physically-based models, and requires simpler system-level models that capture the essential elements of the system.

Such system-based conceptual models, which explicitly consider the network structure and simplified process dynamics have been at the heart of hydrologic response frameworks. Major advances include the development of the instantaneous unit hydrograph (IUH) and geomorphologic IUH theories [e.g., *Rodriguez-Iturbe and Valdes*, 1979; *Gupta et al.*, 1980], the width function formulation of the unit hydrograph [e.g., *Kirkby*, 1976; *Troutman and Karlinger*, 1985; *Gupta et al.*, 1986; *Mesa and Mifflin*, 1986; *Marani et al.*, 1991], river network transport models based on stochastic Kolmogorov equations [e.g., *Gupta et al.*, 1986; *Rinaldo et al.*, 1991; *Marani et al.*, 1991], and also theories of scaling of the hydrologic response [e.g., *Mantilla et al.*, 2006; *Furey and Gupta*, 2007; *Gupta et al.*, 2010]. Apart from the flux of water, similar concepts of system response have also been used for the computation of fluxes of

sediment [e.g., *Lee and Yang*, 2010; *Czuba and Foufoula-Georgiou*, 2014] as well as nutrients [e.g., *Botter et al.*, 2006; *Rinaldo et al*., 2006b] at the outlet of a basin. These system-based conceptual models allow investigation of emergent behavior in terms of the timing and magnitude of peak response of a flux as well as tracing the origin of that flux from disparate basin-wide contributions (e.g., see chapter 2 or *Czuba and Foufoula-Georgiou* [2014] for a recent application). However, focusing on the response at the basin outlet only does not help in identifying where and when critical hotspots, defined as places of excess flux accumulation, might emerge on the network.

Identification of hotspots on a river network requires a model that tracks a flux explicitly on the river network, providing a continuous description of its spatiotemporal evolution at all locations and all times. Such an approach often necessitates simplifying the process dynamics in order to model the flux at the basin scale and over long periods of time. A number of models exist that explicitly track a flux on the river network focusing on bed-material sediment [*Benda and Dunne*, 1997a; *Benda et al.*, 2004b], nitrate and denitrification [*Alexander et al.*, 2009], phytoplankton and nutrient limitation on biomass [*Istvánovics et al.*, 2014], invasion of zebra mussels [*Mari et al.*, 2011], spreading of cholera [*Bertuzzo et al.*, 2008], distribution of benthic invertebrates [*Ceola et al.*, 2014], and distribution of biodiversity of freshwater fish species [*Muneepeerakul et al*., 2008; *Bertuzzo et al.*, 2009]. While not an explicit focus of these models, it is argued here that the space-time distribution of a flux on the network generated by these models can be used to identify hotpots.

In this chapter, we are mostly concerned about identifying hotspots of fluvial geomorphic change. Fluvial geomorphic change (e.g., changes to channel planform, channel width, roughness, or slope) often occurs where there is a local imbalance of sediment and water fluxes, conceptually embodied through (an expanded) Lane's balance [e.g., *Dust and Wohl*, 2012]. This imbalance drives fluvial geomorphic change through physical mechanisms such as bank erosion, channel incision, and aggradation. Hotspots of fluvial geomorphic change are then locations where these changes are occurring at much higher rates than are occurring throughout the rest of the basin. The identification of potential hotspots of fluvial geomorphic change at the network scale has only focused

on identifying confluences susceptible to change based on their position in the network [e.g., *Benda et al.*, 2004a, 2004b]. These works are an important step forward, but much can still be learned by incorporating simplified process-dynamics that would allow assessment of changes that may occur in specific river reaches rather than just at confluences.

A specific type of fluvial geomorphic change associated with a change in channel planform is channel migration. Channel migration has been described as being driven by one of two mechanisms depending on whether outer-bank erosion or inner-bank deposition is taking the lead: (1) streamflow-driven bank-pull, i.e., more rapid erosion of the outer bank forcing deposition on the point bar along the inner bank, and (2) sediment-driven bar-push, i.e., more rapid accretion of the point bar along the inner bank forcing erosion of the outer bank [*Parker et al.*, 2011; *van de Lageweg et al.*, 2014; *Eke et al.*, 2014]. The identification of hotspots of channel migration has typically been limited to pinpointing specific bends of river reaches [e.g., *Lagasse et al.*, 2004; *Abad and Garcia*, 2006; *Motta et al.*, 2012]. However, in the larger spatial context of a river network, we hypothesize that it may be possible to identify hotspots of channel migration driven by the bar-push mechanism by identifying reaches where sediment persists within a river network. This hypothesis forms the basis of this work and it is tested using a simplified model of transport and independently collected field observations of channel migration.

In chapter 2, we developed a network-based, sediment-transport model following a Lagrangian perspective and used it to compute the sedimentograph at the outlet of a basin (defined as the sediment response function to a uniformly distributed input of sediment throughout the basin). In this chapter, we extend this framework to interrogate the system not only at its outlet response but also within it, i.e., its internal dynamics. That is, we seek to understand how sediment is organized and where sediment accumulates due to the combined effects of transport dynamics (accounting for slopes, channel morphology, bed shear stress, grain size, etc.) and river network structure (topology and associated geometry). Specifically, we present a dynamic connectivity framework for describing the organization of a flux on a network (section 3.2) and then apply this framework to sand transport in the Greater Blue Earth River Basin in Minnesota (section 3.3). We show how

this framework can be used to assess the persistence of mass within different reaches of a network and ultimately identify hotspots of fluvial geomorphic change associated with observed high rates of channel migration (section 3.4). This framework was then used to pinpoint the sources of sediment contributing to large clusters which can be useful information for management decisions (section 3.5). Finally, we close with some concluding remarks (section 3.6).

3.2 Dynamic Connectivity Framework

The term "connectivity" as applied in geomorphology and hydrology has had a number of different definitions (for a review of recent literature addressing hydrological connectivity see *Bracken et al.* [2013] and sediment connectivity see *Bracken et al.* [2015] and also *Heckmann et al.* [2015]). In the context of sediment connectivity, these definitions generally refer to the degree to which sediment is able to move between different landscape features. Most recently, *Bracken et al.* [2015] defines "sediment connectivity" as, "the integrated transfer of sediment across all possible sources to all potential sinks in a system over the continuum of detachment, transport, and deposition, which is controlled by how the sediment moves between all geomorphic zones: on hillslopes, between hillslopes and channels, and within channels." Herein we use the term "connectivity" in the general sense of the definition as "being connected" and apply it in the context of fluxes on a network. We consider two fluxes "connected" if they are in close spatial proximity along the river network (how close is close enough is discussed in sections 3.2.3 and 3.3.3) and refer to "connectivity" as the state of two or more fluxes being connected. Then by "dynamic connectivity" we refer to how the connectivity of fluxes changes in time.

The proposed framework for considering the dynamic connectivity of a flux involves establishing the network (section 3.2.1), tracking a flux on the network (section 3.2.2), and then quantifying the dynamic connectivity of the flux from its spatial organization on the network (section 3.2.3). The flux we consider herein is sand, i.e., sediment with grain size of 0.062-2 mm.

3.2.1 River Network

Let the river network be defined as a directed network of connected links where direction of flow is uniquely defined. Each link i represents a segment of the river network between a source and a junction (a source link), two successive junctions, or a junction and the basin outlet. Junctions are the points at which two links join and connect to one downstream link, sources are the points farthest upstream in the network, and the outlet is the point farthest downstream in the network. Each link i is assigned a "geomorphic state" ξ_i with physical attributes corresponding to that state. Although this framework can be used for any connected flow paths (e.g., hillslope or subsurface paths), herein we only consider a fluvial channel network, thus every link corresponds to the geomorphic fluvial state $\xi_{f,i}$ with geomorphologic and hydraulic attributes of the link (Figure 3.1a), i.e., $\xi_{f,i}(\ell_i, a_i, A_i, S_i, Q_{w,i}, H_i, B_i, \ldots)$, where the geomorphologic attributes include link length ℓ_i [L], directly contributing area a_i [L^2], upstream drainage area A_i [L^2], and link slope S_i; and the hydraulic attributes include streamflow $Q_{w,i}$ [L^3T^{-1}], cross-section average depth H_i [L], width B_i [L], etc. While not indicated explicitly, attributes of the geomorphic fluvial state $\xi_{f,i}$ may also be a function of time to capture possible time-varying properties of the system.

3.2.2 Transport Dynamics

The theoretical basis of the proposed transport formulation rests on the link between Eulerian and Lagrangian transport formalisms by which one can establish the relation between the space-time trajectories of an ensemble of inputs to the network at an initial time to the arrival (or travel) time distribution at a fixed location [e.g., *Rinaldo and Rodriguez-Iturbe*, 1996]. The proposed framework uses a Lagrangian formulation of transport where "parcels" are injected at different locations in the basin at an initial time t_0 and their trajectories are followed over space and time. A parcel is a fundamental unit transported on the network and represents a collection of particles that can be physically

treated as a coherent unit. Adopting established notation, let us denote by $m(\boldsymbol{X}_0, t_0)$ the initial mass of a parcel injected at time t_0 at an initial position $\boldsymbol{X}_0 = \boldsymbol{X}(t_0)$ and let $\boldsymbol{X}(t)$ denote its trajectory defined by the Lagrangian coordinate of the parcel at time t. Acknowledging uncertainties and natural variability in the transport process, the trajectory $\boldsymbol{X}(t)$ of a parcel can be seen as a random function $g(\boldsymbol{X}, t)$, called the displacement probability density function (pdf), where $g(\boldsymbol{X}, t)d\boldsymbol{X}$ characterizes the probability that a parcel is in location $(\boldsymbol{X} - d\boldsymbol{X}, \boldsymbol{X} + d\boldsymbol{X})$ at time t [e.g., *Rinaldo and Rodriguez-Iturbe*, 1996]. Considering an ensemble of parcels traveling over different pathways along the branching river network, the travel time formulation of the hydrologic response relies on establishing the relation between the displacement pdf $g(\boldsymbol{X}, t)$ and the travel time pdf $f(t)$ at a fixed control section, here the outlet of a basin, although any point in the basin can act as the outlet of a smaller subbasin. To establish this relation, first we must define a fixed control section in the transport volume V [L^3] such that all parcels injected into V are transported past the control section. The arrival time T_a [T] of a parcel at the control section is also a random variable characterized by the probability that a parcel originating from $\boldsymbol{X}_0$ at t_0 has already crossed the control section at time t, i.e., $P(T_a < t) = P(t; \boldsymbol{X}_0, t_0)$. Eulerian and Lagrangian approaches are thus linked as

$$P(T_a < t) = 1 - \int_V g(\boldsymbol{X}, t; \boldsymbol{X}_0, t_0)\, d\boldsymbol{X}, \tag{3.1}$$

where the travel time pdf is given by

$$f(t) = \frac{dP(T_a < t)}{dt}. \tag{3.2}$$

A detailed account of this development has been described by *Rinaldo and Rodriguez-Iturbe* [1996].

We consider an instantaneous and spatially uniform input of sediment throughout the basin; this allows us to probe the system and quantify its response and the space-time organization of fluxes that emerges as a system property due to network topology and process dynamics. In other words, a uniform input transported though the network will

reveal the system predisposition for recurring local patterns and locations where flux accumulates and persists, important indicators of sediment-driven fluvial geomorphic change. For simplicity, we attribute the instantaneous spatially uniform input of sediment to the basin as an instantaneous input at the upstream end of every link. Although the directly contributing area to every link might differ and thus the quantity of sediment input to every link might be spatially variable, here we assume it constant (without loss of generality) and call each input a "parcel" of sediment (with each parcel indexed by a unique index k) as p_k all with the same mass m [M] (Figure 3.1b). In other words, each parcel represents a hillslope contribution of sediment associated with the link in which the parcel was first introduced.

The Lagrangian framework of transport moves all these instantaneously released parcels at time $t = t_0$ through the network according to the specific process dynamics. At every time t, we track the location of each parcel p_k, i.e., its Lagrangian trajectory $\boldsymbol{X}_{p_k}(t)$. If the original river network has N links then N parcels $p_1, p_2, \ldots, p_N$ were released at time $t = t_0$ at locations $\mathcal{X}_0(t_0) = \{\boldsymbol{X}_{p_1}(t_0), \boldsymbol{X}_{p_2}(t_0), \ldots, \boldsymbol{X}_{p_N}(t_0)\}$, which in our case are the coordinates of the upstream junctions of all links. As the parcels move downstream, at any time t we will have a collection of Lagrangian parcel locations as $\mathcal{X}(t) = \{\boldsymbol{X}_{p_1}(t), \boldsymbol{X}_{p_2}(t), \ldots, \boldsymbol{X}_{p_N}(t)\}$. Through transport on the hierarchical branching river network, these parcels become spatially organized and this organization changes dynamically over time (Figure 3.1c-d). This set of parcel trajectories embeds a measure (here parcel mass m at locations $\mathcal{X}(t)$ and 0 everywhere else) on the underlying network. For each link, we can then compute the total mass $m_i(t)$ in link i at time t as

$$m_i(t) = \sum_{\substack{\text{parcels } p_k \\ \text{in link } i \\ \text{at time } t}} m . \tag{3.3}$$

The displacement pdf $g(\boldsymbol{X}, t)$ of each parcel is established based on the dynamics of sand transport. A pathway $\gamma_i = \{\xi_i, \ldots, \xi_\Omega\}$ that a parcel introduced into link i will follow before reaching the basin outlet Ω is defined as the set of geomorphic states from

ξ_i (short hand notation for $\xi_{f,i}$) through the network to the outlet (i.e., $\xi_i \rightarrow \ldots \rightarrow \xi_\Omega$). The time t_i a parcel spends in geomorphic state ξ_i can equally well be thought of as a travel time through, or residence time within, geomorphic state ξ_i. The travel time t_i is a random variable which can be described by the pdf $f_{\xi_i}(t)$ that embodies the dynamics (and inherent variability) of sand transport. In the formulation considered herein, the travel time t_i is described deterministically following the derivation presented in chapter 2 based on an elaborate analysis of sand transport assuming: 1) uniform (normal) flow, 2) that *Engelund and Hansen's* [1967] sediment-transport formula represents the sand-transport process (neglecting the shear stress partition for bedforms), 3) hydraulic geometry scaling of streamflow depth, width, and velocity, 4) an intermittency of flows that transport the majority of sediment, 5) that sediment supply does not exceed transport capacity, and 6) that sediment does not enter long-term floodplain storage. An overview schematic of this formulation is presented in Figure 3.2. See chapter 2 for a detailed discussion of the formulation and its limitations.

Under this formulation, the travel time $t_{s,i}$ [T] of a sand parcel p_k in a geomorphic fluvial state $\xi_{f,i}$ was computed as the time it takes a sand parcel to move through a link of length ℓ_i at a bulk sand transport velocity $u_{s,i}$ [LT^{-1}] as

$$t_{s,i} = \frac{\ell_i}{u_{s,i}}. \tag{3.4}$$

The bulk sand transport velocity $u_{s,i}$ was obtained by decomposing the volumetric transport rate of sand $Q_{s,i}$ [L^3T^{-1}] into a velocity and two length scales as

$$Q_{s,i} = u_{s,i}(\theta_i H_i)B_i, \tag{3.5}$$

where H_i [L] is the channel depth of link i, B_i [L] is the channel width of link i, and θ_i is a scale factor such that together $(\theta_i H_i)$ defines a characteristic vertical length scale for sand transport where the majority of sand transport takes place. After combining equations for channel hydraulics, sand transport, and volumetric transport rate of sand (see Figure 3.2), the bulk sand transport velocity is given as

$$u_{s,i} = \frac{0.05}{\theta_i \, g^{1/2} R_i^2 D_i} u_{w,i}^2 H_i^{1/2} S_i^{3/2} , \tag{3.6}$$

where g [LT^{-2}] is the acceleration due to gravity, R_i is the submerged specific gravity of sediment in link i, D_i [L] is the sediment grain size in link i, and $u_{w,i}$ [LT^{-1}] is the streamflow velocity of link i. By further incorporating hydraulic geometry relations that parameterize $u_{w,i}$ and H_i as functions of upstream drainage area A_i at a characteristic flow, accounting for an intermittency of flows $I_{f,s}$ that transport the majority of sediment based on that characteristic flow [*Paola et al.*, 1992; *Parker*, 2004], and substituting equation (3.6) into equation (3.4), the travel time $t_{s,i}$ of a sand parcel p_k in a geomorphic fluvial state $\xi_{f,i}$ can be obtained as

$$t_{s,i} = \frac{\theta_i \, g^{1/2} R_i^2 D_i}{0.05 \alpha_{u_w A}^2 \alpha_{HA}^{1/2} I_{f,s}} \ell_i A_i^{-(2\beta_{u_w A} + \beta_{HA}/2)} S_i^{-3/2} , \tag{3.7}$$

where $\alpha_{u_w A}$ and α_{HA} are empirically derived coefficients and $\beta_{u_w A}$, and β_{HA} are empirically derived exponents of the hydraulic geometry scaling relations.

Sand-transport dynamics have been reduced to physically based time delays in a way that greatly simplifies the flux computation such that each sand parcel p_k moves through a geomorphic fluvial state $\xi_{f,i}$ with a travel time $t_{s,i}$. After a parcel spends $t_{s,i}$ amount of time in geomorphic fluvial state $\xi_{f,i}$, it transitions to the immediately downstream link where it spends some amount of time before transitioning again. When considering long-term storage in an adjacent floodplain geomorphic state, there may be a probability of first entering into long-term floodplain storage before returning back to the fluvial channel and then on to the downstream link. But in this formulation, by neglecting long-term floodplain storage of sand and only considering transport below capacity, the travel time $t_{s,i}$ of a sand parcel in a geomorphic fluvial state $\xi_{f,i}$ represents a lower bound on the fastest time scale for sand to transport through the system.

In the network context, the travel time $T_{s,i}$ along pathway γ_i is the sum of travel times through each of the geomorphic states comprising the pathway as

$T_{s,i} = t_{s,i} + \ldots + t_{s,\Omega}$. In theoretical formulations, the travel times $\{t_{s,i} + \ldots + t_{s,\Omega}\}$ are often considered independent random variables such that the derived distribution $f_{\gamma_i}(t)$ of the sum of the travel times $\{t_{s,i} + \ldots + t_{s,\Omega}\}$ can be written as the convolution of the individual travel time pdfs as $f_{\gamma_i}(t) = f_{\xi_i} * \ldots * f_{\xi_\Omega}$. Herein, we do not seek analytical solutions as the physical properties of every link are explicitly considered and are too complex to be described analytically.

Within this transport formulation, it is relatively simple to incorporate functional dependencies between attributes of a geomorphic state ξ_i and attributes of a parcel p_k traveling in link i, as well as the accumulation of mass $m_i(t)$ in that link i due to the transport of other parcels. For instance, the transport of coarse sediment through a fluvial channel depends on the slope of the channel which depends on the accumulation of sediment in the channel (i.e., mass of all parcels in a link) which circles back to affect the slope of the channel. Additionally, an excessive accumulation of sediment in a link or high streamflow (when considering both water and sediment fluxes simultaneously) may be used to signal the input of more sediment to the network through a bank-erosion mechanism. Each of these variables can be updated in our framework at any time t depending on the state of any of the other variables. Thus this transport formulation can couple geomorphic properties with density-dependent transport together with autogenic inputs, all within a network context.

3.2.3 Dynamic Connectivity

We are interested in quantifying the "dynamic connectivity" of these parcels as they are organized on the network and how this connectivity changes over time. Specifically, we are interested in defining "clusters" describing where mass coalesces into a connected extent of the network at a given time t. Within the proposed transport formulation which tracks individual parcels over links of the network, clusters can be defined in two ways: (1) using links as the elementary distance unit or (2) using the actual distance between adjacent parcels as the distance unit.

(1) *Link definition*: This definition is based on assigning the mass m of a parcel to the link within which the parcel trajectory $\boldsymbol{X}(t)$ at time t falls. Two adjacent links are considered connected at time t if both links have at least one parcel in them. Then a cluster is defined as the set of consecutively connected links (Figure 3.1e-f). This definition can be modified by changing the mass threshold to more than one parcel per link depending on the problem at hand.

(2) *Inter-parcel distance definition*: Two situations can arise using the link definition that one might want to avoid: (1) the presence of one parcel in a very long link at time t that augments a cluster or (2) the absence of parcels in a very short link at time t that breaks up a cluster. Both of these situations arise due to the variable discreteness of the measuring unit (link length). Therefore, we apply a continuous distance measure which is the actual distance between adjacent parcel p_k and p_l computed along the network, i.e.,

$$d_{k,l}(t) = \left| \boldsymbol{X}_{p_k}(t) - \boldsymbol{X}_{p_l}(t) \right|_{\substack{Along \\ Network}}, \tag{3.8}$$

called the inter-parcel distance $d_{k,l}(t)$ [L]. Then by selecting a threshold distance d^* [L] we define a cluster by considering the set of all adjacent parcels (upstream and immediately downstream parcels along the network) whose inter-parcel distances $d_{k,l}(t)$ are $\leq d^*, \forall p_k, p_l$ parcels within the cluster (Figure 3.1g-h).

Although we have implemented both definitions, herein we only report clusters defined by the inter-parcel distance definition and denote $C_j(t)$ as the cluster j that at time t was composed of the set of parcels with inter-parcel distances of at most d^* (a procedure to compute d^* is discussed in section 3.3.3). Once a cluster has been defined we compute its total mass $M_j(t)$ [M] as the sum of all parcel masses within the cluster, i.e.,

$$M_j(t) = \sum_{\substack{\text{parcels } p_k, p_l \\ \text{in cluster } j \\ \text{at time } t}} m, \quad \text{s.t. } d_{k,l}(t) \leq d^*, \tag{3.9}$$

and its total length $L_j(t)$ [L] as the sum of (upstream and immediately downstream

along the network) inter-parcel distances, i.e.,

$$L_j(t) = \sum_{\substack{\text{parcels } p_k, p_l \\ \text{in cluster } j \\ \text{at time } t}} d_{k,l}(t), \quad \text{s.t. } d_{k,l}(t) \le d^*. \tag{3.10}$$

At any time t, many distinct clusters within the network may exist forming a set of clusters, each with its own properties of mass and length. From the perspective of a link, clusters form, grow, move by, or break apart through time. The hypothesis is that locations where sediment accumulates (forming clusters of a length exceeding several link lengths) and persists for a considerable period of time are more prone to fluvial geomorphic change, and thus may potentially identify hotspots of fluvial geomorphic change. To test this hypothesis we define a "cluster persistence index" (CPI) or CPI_i [MT] (to denote a specific value of the index for link i) which considers on every link i the cumulative effects of all clusters j that have occupied that link from time t = 0 until all parcels have left the system as

$$CPI_i = \int_{\substack{\text{over all} \\ \text{times } t}} M_j^{(i)}(t)\, dt, \tag{3.11}$$

where the superscript (i) denotes all clusters $M_j^{(i)}(t)$ that occupy link i at time t. Because the spatial extent of clusters is defined continuously on the network (i.e., using the inter-parcel distance definition and not the discrete link definition), the cluster persistence index can also be defined continuously on the network, although here we only evaluate the CPI_i at each link i.

The CPI is analogous to an impulse from classical mechanics, where an impulse is the integral of a force over time (with units of force × time) representing the change in linear momentum over that time. Instead of the integral of a force, the CPI is the integral of the mass of any cluster spanning link i over all times (with units of mass × time) representing the persistence of mass over time. In this way the CPI identifies areas where mass has a tendency to persist that may induce sediment-driven fluvial geomorphic change. It is important to note that the CPI is not directly related to geomorphic work or stream power. Power is the rate of doing work (with units of force × velocity) and within

the context of stream power is $\rho g Q_{w,i} S_i$ [e.g., see *Leopold et al.*, 1964]. Stream power then is the rate of energy dissipation against the stream bed or banks by the flowing water per unit downstream length. Hotspots of streamflow-driven fluvial geomorphic change can be identified by stream power or bed shear stress ($\tau_{b,i} = \rho g H_i S_i$ [$ML^{-1}T^{-2}$]), whereas hotspots of sediment-driven fluvial geomorphic change can be identified by the persistence of sediment through the CPI_i. The longer sediment persists in a reach, the more likely it is that sediment accretion on point bars is forcing erosion of the outer bank, leading to channel migration through the so-called bar-push mechanism.

3.3 Application to the Greater Blue Earth River Basin

The dynamic connectivity framework was applied to sand transport on the Greater Blue Earth River Network. Section 3.3.1 includes a history of the basin, presenting the motivation for identifying potential hotspots of fluvial geomorphic change. Then in applying the framework, section 3.3.2 includes a description of the fluvial channel network and the parameterization of the travel-time formulation for sand transport. Finally, section 3.3.3 includes a description of sand transport on the river network, and quantification of the dynamic connectivity and the emergence of clusters of sand.

3.3.1 Landscape History

The Greater Blue Earth River Basin, which comprises the Watonwan, Blue Earth, and Le Sueur River Basins, drains about 9,200 km^2 of Minnesota and Iowa and is a tributary to the Minnesota River (Figure 3.3a-b). This basin has been sculpted by glaciers and post-glacial processes, with two notable geomorphic processes [see *Gran et al.*, 2013]. The first occurred during glacial retreat with the formation of a proglacial lake known as Glacial Lake Minnesota [*Ojakangas and Matsch*, 1982], which covered a portion of the Greater Blue Earth Basin (Figure 3.3c-d; the approximate historical extent of historical Glacial Lake Minnesota was determined as the extent of the glaciolacustrine environment by *Hobbs and Goebel* [1982]). The second began around 13,400 years ago with the

carving of the Minnesota River valley after Glacial Lake Agassiz drained catastrophically through the proto-Minnesota River [*Clayton and Moran*, 1982]. This event lowered the base level of the Greater Blue Earth River creating a knickpoint, or sharp increase in channel gradient, at the mouth of the river. Over time this knickpoint has migrated 35-40 km upstream creating a knickzone (extent shown as 40 km from the basin outlet in Figure 3.3d and f) of rapidly incising channels disconnected from their floodplains [*Gran et al.*, 2009, 2011b, 2013; *Belmont*, 2011; *Belmont et al.*, 2011]. Upstream of the knickzone, streams meander through low-gradient uplands (Figure 3.3d-f) that were historically dotted with poorly drained wetlands [*Marschner*, 1974].

Throughout the basin, wetlands were drained beginning in the late 1800s for agriculture. The construction of surface ditches and installation of subsurface drain tiles continued as agriculture expanded throughout the basin. As of 2011 agriculture accounted for 85% of the land use in the basin [*Jin et al.*, 2013]. While an extensive subsurface drainage system has reduced erosion from upland fields, a consequence was the creation of more erosive rivers and an increase in sediment erosion from near-channel sources such as banks and bluffs [*Belmont et al.*, 2011; *Schottler et al.*, 2014]. The Greater Blue Earth River Basin has historically exported a disproportionally large amount of sediment compared to surrounding basins [*Kelley and Nater*, 2000], and as of 2002-2006 contributed over 50% of the sediment supply to the Minnesota River despite only accounting for roughly 20% of the total area [*Wilcock*, 2009]. Since European settlement, sediment export from this basin has skyrocketed, increasing by over an order of magnitude in just over a century [*Kelley and Nater*, 2000]. While near-channel sources of sediment have been identified as the culprit [*Belmont et al.*, 2011], management actions require an identification of hotspots to prioritize management actions [*Gran et al.*, 2011a].

3.3.2 Network Extraction and Sand Transport Formulation

Applying the dynamic connectivity framework to this basin first requires extracting the river network. The Greater Blue Earth River Network was obtained from the National

Hydrography Dataset Plus Version 2 (NHDPlusV2) [*McKay et al.*, 2012; *Horizon Systems*, 2014]. The process of converting the NHDPlusV2 network into a useable network for this analysis included clipping the NHDPlusV2 network to the basin extent, removing isolated and secondary channels, and establishing a new set of links, with one link between tributary junctions, and with attributes mapped or recomputed for the extent of the new link from the original NHDPlusV2 network. This process created a new network derived from the NHDPlusV2 network (Figure 3.3) with each link connecting to one downstream link and either zero or two upstream links, and with attributes: index of link i, index of downstream link, link length ℓ_i, upstream drainage area A_i, elevation of upstream and downstream ends of each link, and channel slope S_i (note all slopes less than 0.0001 were set to this value). Link lengths for this Greater Blue Earth River Network varied from 30 m to 25 km (mean = 4 km, median = 3 km, with an exponential distribution). Every link in this network was treated as a fluvial channel (i.e., geomorphic fluvial state) and all attributes of the geomorphic fluvial state were treated as constant in time.

Next, the travel time $t_{s,i}$ of a sand parcel p_k in a geomorphic fluvial state $\xi_{f,i}$ was reduced to a function of only network properties by assigning parameters specific to the Greater Blue Earth River Basin. These parameters included: g = 9.81 m·s^{-2}, θ_i = 0.1 ($\forall i$), R_i = 1.65 ($\forall i$), D_i = 0.0004 m ($\forall i$; D50 size of sand from riverbed material [*U.S. Geological Survey*, 2014]), $\alpha_{u_w A}$ = 0.20, $\beta_{u_w A}$ = 0.07, α_{HA} = 0.0029, β_{HA} = 0.29 (computed at the two-year recurrence interval peak flow Q_2 and using streamflow and channel cross-sectional properties of 23 stations; here A_i is specified in m^2, H_i in m, and $u_{w,i}$ in m·s^{-1}), and $I_{f,s}$ = 0.175 (computed from a flow-duration curve; see chapter 2 for details). Substituting these parameters into equation (3.6) reduces the bulk sand transport velocity $u_{s,i}$ to

$$u_{s,i} = 0.32 A_i^{0.285} S_i^{3/2}, \tag{3.12}$$

where $u_{s,i}$ is given in meters per second. Similarly, substituting these parameters into

equation (3.7) reduces the travel time $t_{s,i}$ of a sand parcel p_k in a geomorphic fluvial state $\xi_{f,i}$ to

$$t_{s,i} = 18\ell_i A_i^{-0.285} S_i^{-3/2}, \tag{3.13}$$

where ℓ_i is specified in meters and thus $t_{s,i}$ is given in seconds (Figure 3.2).

Using equation (3.13) to specify how a parcel moves through each link of the network, the locations of sand parcels were then computed at a time step of about 23 days (which arose by using a time step of 4 days for transport at a constant Q_2 and accounting for the intermittency factor of 0.175) such that several time steps were required before most parcels moved through each link of the network. The time step here merely serves as the discrete time interval at which the parcel locations are being "viewed" during the continuous parcel transport through the network. This time step does not affect how parcels are transported in any way because there are no feedbacks amongst the number of parcels in a link, parcel transport, and the attributes of the fluvial geomorphic state in this application.

3.3.3 Dynamic Connectivity and Emergent Clusters of Sand

An instantaneous spatially uniform input (at time $t = 0$) of sand parcels, each representing a hillslope contribution, was "organized" by the river network structure and process dynamics into a spatially heterogeneous distribution on the network as time evolved (Figure 3.4). Early on (time 0.4 years), sand parcels were distributed throughout the basin and over time (time 4 years) sand concentrated in downstream channels. Eventually (by time 40 years), sand concentrated in the mainstem channels and remained there for some time before all inputs left the basin.

The arrival time distribution of sand at the outlet of the basin is the sand response function (Figure 3.5c; see chapter 2). The sand response function captures the combined network structure and process dynamics through time delays of sand transport on the network. This is in contrast to the network width function (Figure 3.5a), which captures the distance distribution of each link of the network to the outlet. Sand transport

dynamics embodied by equation (3.13), rearrange and reorder hillslope contributions compared to uniform velocity transport on the network (given by the network width function). This effect was not only apparent in the redistribution of mass in the sand response function compared to the width function, but also in the spatial distribution of contributions to the outlet where more mass arrived sooner than the distance alone would explain (Figure 3.5). This speaks for the non-linear "stretching" of distance to time arising from the process dynamics on the river network. It also highlights the process-dependent nature of the "coarse-graining" of the landscape, i.e., partitioning the basin in spatial units that contribute almost simultaneously to the outlet. Furthermore, the sand response function illustrates the complex response of sediment yield at the outlet of a basin to a disturbance event, even under uniform input and simplified process dynamics, in accordance with other modeling literature [e.g., Wainwright, 2006].

Internally within the network before all sand arrived at the outlet, the location of each parcel was tracked through time and the inter-parcel distance $d_{k,l}(t)$ between every parcel and its nearest downstream parcel was measured for all times. This captured the nearest upstream and downstream inter-parcel distances between all parcels in the system at all times. At each time step, the pdf of inter-parcel distance was obtained and is plotted in Figures 3.6a-d. In these figures the pdfs were rescaled by setting their modes to one to allow a better visual representation of their time evolution (modes were assigned the same color). An interesting abrupt shift in the mode of the pdfs of inter-parcel distance (loosely referred to as a "phase transition") was observed. This phase transition occurred around 0.4 years and shifted the most probable inter-parcel distance from about 4 km when parcels were relatively far apart to about 100 m when parcels came close to each other by around 4 years (see Figure 3.6a-d, where the vertical lines correspond to 0.4, 4, and 40 years). These two length scales of inter-parcel distance (4 km and 100 m) emerged from the process dynamics on the hierarchical branching network: the 4-km length scale arose from a characteristic scale of link lengths (4 km is the mean of the link length distribution), and the 100-m length scale arose from system dynamics positioning parcels close together over time. Based on the separation of these two length scales of inter-parcel distance, we set a distance threshold of $d^* = 1$ km (long-dashed horizontal line,

Figure 3.6d) for defining a cluster. By setting this distance threshold, clusters only form when the system dynamics bring parcels within close proximity. The evolution of all clusters was then tracked over time throughout the river network. At each time step, there was a distribution of cluster sizes. Specifically, the number of clusters and a few statistics describing spatial cluster size (maximum, 90^{th} percentile, and median) are shown in Figure 3.6e-f.

Early on (before time 0.4 years), small clusters formed as parcels were transported to downstream links. The number of clusters achieved a maximum around 0.4 years, just before the beginning of the phase transition of inter-parcel distance (Figure 3.6). During this time, clusters were spread throughout the branches of the network (Figure 3.7a), while over time parcels transported farther downstream forming larger and fewer clusters. The maximum spatial cluster size formed around 4 years, after the phase transition of inter-parcel distance (Figure 3.6). At this time clusters were more concentrated in downstream channels but could still be found throughout the basin (Figure 3.7b).

Multiple peaks of the maximum spatial cluster size occurred through time (Figure 3.6f). The first major peak around 4 years (see Figure 3.7b) and the second around 10 years were both concentrated in the same location along the Watonwan River. These multiple peaks corresponded to hillslope contributions from two different source areas each coalescing into a large cluster at this location before moving through the system. The third major peak of the maximum spatial cluster size occurred around 40 years (Figure 3.6f) and corresponded to a reach of the Blue Earth River (Figure 3.7c). Note the large temporal fluctuations of the (short-lived) max cluster size and the more robust in time 90^{th} percentile and median cluster sizes. Our CPI is by definition highest when both a large size cluster exists and also has a long temporal persistence at the same location, as this increases the potential for sediment-driven fluvial geomorphic change. Eventually the cluster size statistics go to zero as all of the sand parcels leave the system.

3.4 Identifying Hotspots of Fluvial Geomorphic Change

The question posed here is whether, within the dynamic connectivity framework, the emergence of sediment clusters that are integrated through time into the CPI can be used as a tool for (a) identifying hotspots of fluvial geomorphic change and (b) gaining insight into the possible driving mechanisms of this change. In our basin we used channel migration as a measure of fluvial geomorphic change and specifically focused on three places within the basin where high rates of channel migration have been observed (defined as hotspots). Channel migration data were measured within 20-m increments for the downstream portions of the Watonwan, Blue Earth, Maple, and Le Sueur Rivers by comparing the movement of digitized river channels from 2 sets of aerial photographs from 1938 and 2005 to provide an average migration rate over the time period 1938-2005 (Figure 3.8a; all channel migration data shown have been spatially averaged using a 5-km smoothing window) [*Belmont et al.*, 2011; *Bevis*, 2015]. The spatial pattern of channel migration was heterogeneously distributed on the river network, with three specific reaches of high rates of change (here denoted as h1, h2, and h3) along the Watonwan (h1), Blue Earth (h2), and Le Sueur (h3) Rivers (Figure 3.8a).

The CPI (equation 3.11), integrates the evolution of clusters in the Greater Blue Earth River Network following an instantaneous spatially uniform input to all links of the network, and identifies areas of the network where mass concentrates and persists due to time delays on the hierarchical branching river network structure. As discussed before, the purpose of using an instantaneous spatially uniform input was to probe the system and examine its emergent space-time organization, e.g. critical locations where inputs slow down and cluster together (as identified by high CPI), revealing a system property due to network topology and process dynamics. We seek to test the hypothesis that places of high CPI can be used to identify observed hotspots of sediment-driven channel migration. It is seen from Figure 3.8 that the CPI was capable of identifying hotspots h1 and h2 on the Watonwan and Blue Earth Rivers, respectively, that occurred upstream of the knickzone. This might suggest that these hotspots occurred because of a persistence of sediment, forcing channel migration through the bar-push mechanism [*Parker et al.*,

2011; *van de Lageweg et al.*, 2014; *Eke et al.*, 2014].

It is noted that in making cause and effect interpretations, it is important to examine the system predisposition for geomorphic change (as performed above) in view of the possibly heterogeneous spatiotemporal inputs which might negate such a predisposition. For example, an asynchronous timing of sediment supply might ameliorate or even break down the persistence of sediment clustering, depending on the time scales of sediment pulsing versus the time scales of transport. In our case, numerical experiments by randomly varying the starting positions of parcels within the length of each link and also by increasing sediment input at locations where bluffs adjoin the river network (the major sources of accelerated sediment input in this basin), have clearly demonstrated that this is not the case, and that the locations of high CPI are fairly robust. This issue is further discussed in section 3.5 where unraveling the sources of clusters is proposed as a means for guiding management decisions.

As can be seen from Figure 3.8, the CPI qualitatively matches the observed channel migration rate upstream of the knickzone in both the Watonwan and Blue Earth Basins with one exception. At about 15 km upstream of the mouth of the Blue Earth River, CPI was very large but the observed channel migration rate was low (see Figure 3.8d). This is the site of Rapidan Dam on the Blue Earth River, which in the network had a very low slope, representative of the reservoir surface. Obviously the reservoir is not migrating and thus the local context must always be considered in interpreting the results of the analysis.

Hotspot h3 on the Le Sueur River that occurred within the knickzone was not identified by a high magnitude of CPI (Figure 3.8). This might suggest that a different mechanism, such as the streamflow-driven bank-pull mechanism [*Parker et al.*, 2011; *van de Lageweg et al.*, 2014; *Eke et al.*, 2014], was responsible for the amplified migration in hotspot h3. Indeed, the bank-pull mechanism is expected to occur in reaches with high bed shear stress capable of both eroding the channel banks and rapidly transporting supplied sediment downstream, such as in the knickzone where hotspot h3 lies. Bed shear stress $\tau_{b,i}$ was computed for the entire network as $\tau_{b,i} = \rho g H_i S_i$ (where

ρ = 1000 kg·m^{-3}) and is shown in Figure 3.9a; the area with the highest bed shear stress corresponded to hotspot h3 on the Le Sueur River, providing support for the idea that streamflow-driven erosion rather than sediment persistence may drive channel migration here. Bed shear stress was low at hotspots h1 and h2 on the Watonwan and Blue Earth Rivers, respectively, corroborating the hypothesis that channel migration here is driven by a different mechanism than streamflow-driven erosion.

Further support for the bank-pull mechanism in contributing to the geomorphic change associated with hotspot h3 was provided by the finding that incision of this portion of the Le Sueur River over the Holocene was most accurately modeled as a detachment-limited (or supply-limited) system in which downstream coarsening also played a role in setting the modern longitudinal profile [*Gran et al*., 2013]. Additionally, detailed measurements and field observations of eroding bluffs in this portion of the Le Sueur River suggest that undercutting and toe erosion drive bluff retreat, i.e., channel migration into bluffs, and because these bluffs maintain steep faces and do not lie back over time suggests that the river quickly removes any material deposited at the toe of the bluff [*Day et al*., 2013]. Together these observations suggest that this portion of the Le Sueur River is more than capable of transporting any sediment supplied downstream without allowing sediment to persist for a long period of time. Therefore, in this reach of the Le Sueur River (around hotspot h3) the most likely mechanism of channel migration is the bank-pull mechanism. It is also known that in the knickzone of the Le Sueur River, large bluffs contribute a substantial amount of sediment to the river network [*Belmont et al.*, 2011] and thus it is also possible that spatiotemporal heterogeneity of sediment supply, which was not considered herein, may also play a large role in forming this hotspot. Further investigation into all hotspots is necessary to provide more evidence for the causative mechanisms leading to the observed high rates of channel migration.

Geomorphic disturbances can be amplified at and just downstream of confluences due to the high frequency and magnitude of sediment fluctuations from punctuated tributary inputs, and also directly upstream of confluences due to presence of a wider, low gradient reach that is more susceptible to geomorphic change (suggested by the network dynamics hypothesis of *Benda et al.*, [2004a, 2004b]). However, we caution that

the potential for fluvial geomorphic change to occur farther downstream should not be overlooked. For instance, if the receiving stream is capable of transporting the sediment delivered to a confluence farther downstream, then the aggregating effects of these inputs may not manifest into fluvial geomorphic change until the transport capacity of the stream is reduced, such as at a break in slope or at a large increase in channel width. In this case, fluvial geomorphic change may not occur in direct proximity to the confluence although the merging of inputs at the confluence may be responsible for augmenting the sediment flux. This was exemplified by hotspot h2 of fluvial geomorphic change that occurred on the Blue Earth River over 14 km downstream from the nearest major confluence (Figure 3.8a).

We note that hotspot h2 on the Blue Earth River would not have been identified by considering confluence effects alone and that it was only identified by considering simplified process dynamics explicitly on the network. Granted, the heterogeneous distribution of slopes on the network was the primary factor leading to the identification of these hotspots. But it was not obviously apparent from a map of channel slopes (Figure 3.3d) specifically where hotspots of fluvial geomorphic change might arise. Only by incorporating physically-based process dynamics that amplify variations in geomorphic properties, such as channel slope, through non-linear relations within the specific hierarchical arrangement of these properties on the network, were we able to highlight critical hotspots of fluvial geomorphic change (Figure 3.8).

The dynamic connectivity framework provides a means for assessing potential hotspots of fluvial geomorphic change at the network scale and is ideally suited to be used as a rapid identification tool for identifying potential reaches susceptible to fluvial geomorphic change. This framework has advantages over the static spatial metrics such as channel slope (Figure 3.3d) or bed shear stress (Figure 3.9a) through which the identification of all hotspots was not readily apparent (as discussed above). To identify all potential hotpots, one should investigate both reaches of high CPI and also reaches of high bed shear stress (or high stream power, which is closely related). Then this approach can also be useful for hypothesis testing, by suggesting which mechanism of channel migration may be driving change in various locations. Once hotspots are identified using

this framework, more detailed investigations can be performed at the reach scale to further understand causative mechanisms and to better inform potential management actions.

3.5 Unraveling the Source of a Cluster

If hotspots of fluvial geomorphic change can be identified through the emergence of large persistent clusters of mass on the network, the next question is how this information can be used to inform potential management actions. Large clusters that formed at time 4 years (corresponding to h1 on the Watonwan River, Figure 3.10a) and 40 years (corresponding to h2 on the Blue Earth River, Figure 3.10b) after an instantaneous uniform input of sand to all links of the network were unraveled backwards in time to identify their source contributions (at time 0, Figure 3.10c). As these are the largest clusters formed, they are the clusters responsible for the largest contributions to the CPI and the coalescing of their mass may most strongly exacerbate channel migration at these locations. By identifying the source contributions that synchronize on the network to form clusters, management efforts could be taken to reduce sediment generation of these specific source areas or break the synchronization of these contributions before they coalesce into an aggregated mass with a potential to affect fluvial geomorphic change.

Potential management options might include efforts to reduce the erosion at the source (through bank protection measures for bank sources or vegetative buffer strips for upland sources), break the synchronization of arrival of sediment (through construction of riparian wetlands that alter specific reach hydraulics), or mitigate the effects (through bank protection measures for the eroding bank or sediment removal where the bar-push mechanism drives erosion). Depending on the network structure and process dynamics, the potential management options available may differ.

For instance, the large cluster that formed on the Watonwan River (coincident with hotspot h1) formed early on (within 4 years of the input) and thus reflected a proximal upstream source (Figure 3.10). Here there was a short lead time before the cluster formed but the source areas were distributed between two branches. Efforts to break the

synchronization of these inputs here before they form a cluster may be possible through alteration of the geomorphic properties affecting the travel time through one of the branches, but would likely have to be carried out prior to any disturbance due to the short lead time of cluster formation. However, we caution that any efforts to break the synchronization of a potential cluster should be fully investigated to ensure that a larger cluster would not likely form at a different time.

Alternatively, the large cluster that formed on the Blue Earth River (coincident with hotspot h2) formed later on (40 years after the input) and thus reflected a distal upstream source (Figure 3.10). Here there was a long lead time before the cluster formed but the source area was more scattered amongst several subnetworks. Multiple efforts might be required to break the synchronization of these inputs here before they form a cluster due to the distributed nature of the source area, although these efforts could be carried out after a disturbance due to the long lead time of cluster formation. Control of source inputs may be most feasible given the distributed nature of the source area because variations between different subnetworks may make source control more readily possible in some subnetworks than others.

These examples of unraveling source contributions that synchronize at a given location to affect geomorphic change are meant to be illustrative of the type of information that can come out of this framework rather than as a suggestion of where to manage to reduce channel migration in this basin. Once system specific information on spatiotemporal inputs can be considered (available from direct observations, mapping of sediment-generating landscape features, sediment budgets, etc.), then it is possible to verify whether indeed these unraveled source contributions are the main cluster-contributing sediment sources or whether these sources may be overwhelmed by larger sediment sources elsewhere in the basin.

The dynamic connectivity framework provides a network-scale context to process dynamics operating at smaller scales for informing basin management. While not a focus herein, this framework is capable of assessing how changes to the network, in either network structure or through properties such as channel width, at a local scale may cascade into larger changes at the network scale.

3.6 Concluding Remarks

The dynamic connectivity framework presented herein takes a network as a template upon which a flux evolves through time. We suggest that the spatial organization of fluxes into clusters can tell us something about system functioning. This framework is general enough to account for different types of networks as well as time varying properties of the system. Herein, this framework was applied to sand transport on the Greater Blue Earth River Network in Minnesota to assess the potential for using the emergence of sediment clusters, which were integrated through time into a cluster persistence index (CPI), to identify hotspots of fluvial geomorphic change. High values of CPI represent areas where sediment has a tendency to persist on the network, which may be related to sediment-driven fluvial geomorphic change. Of the three hotspots of fluvial geomorphic change (defined as locations where observed rates of channel migration were high), two of these hotspots coincided with high CPI. The third hotspot was not identified by high CPI, but instead was believed to be a hotspot of streamflow-driven change based on additional information and the fact that high bed shear stress coincided with this hotspot. Nonetheless, the dynamic connectivity framework provides a network perspective of dynamical processes that occur at smaller scales, useful for understanding how reach-scale changes cascade into network-scale effects and for informing management actions.

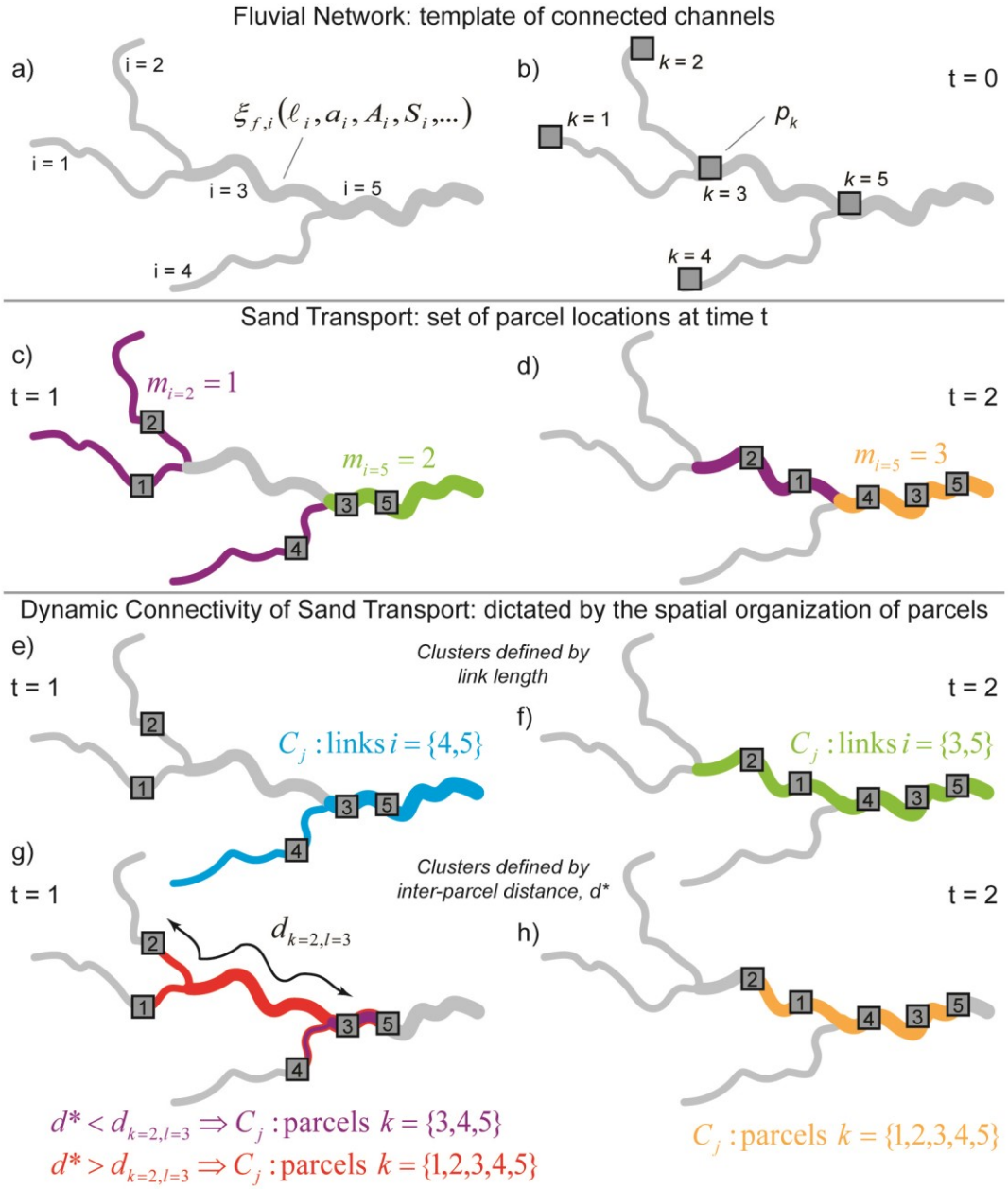

Figure 3.1. Overview of the dynamic connectivity framework. The framework involves: (a) establishing the river network where each link i is assigned a fluvial geomorphic state $\xi_{f,i}$; (b) tracking a flux on the network as a set of locations of the parcels p_k (each of mass $m = 1$) on the network, shown here at times $t = 0$, (c) $t = 1$, and (d) $t = 2$; and then quantifying the dynamic connectivity of the flux from the spatial organization of the parcels on the network, shown as clusters C_j (caption continued on next page)

(caption for Figure 3.1 continued) defined by both link length at times (e) $t = 1$ and (f) $t = 2$ and also inter-parcel distance (d^*) at times (g) $t = 1$ and (h) $t = 2$. See text for cluster definitions.

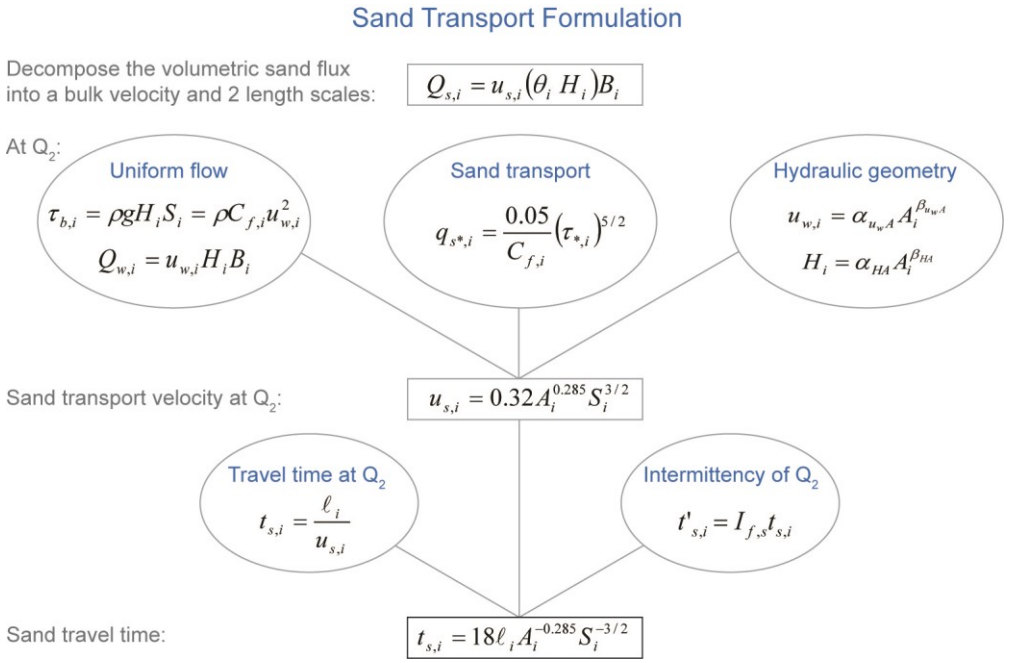

Figure 3.2. Overview of the formulation of sand travel time ($t_{s,i}$) through a fluvial geomorphic state (here link i, with its geomorphic and hydraulic properties). The reduced form of the sand transport velocity and sand travel time incorporates parameters specific to the Blue Earth River Basin. The characteristic flow considered in these computations is the two-year recurrence interval peak flow or Q_2. See text for definitions.

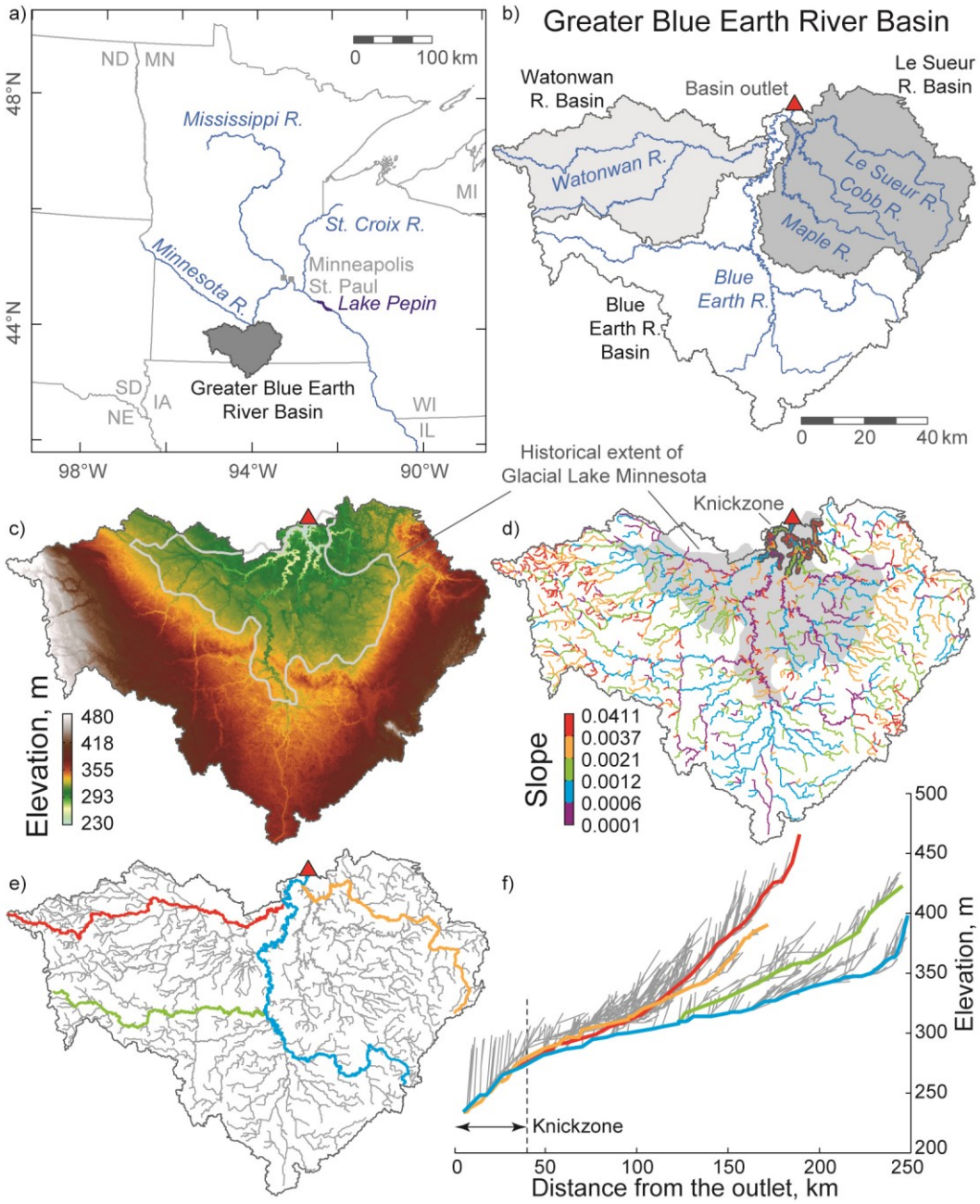

Figure 3.3. Location and description of the Greater Blue Earth River Network. (a) Location map of the Greater Blue Earth River Basin in Minnesota and Iowa comprising the (b) Watonwan, Blue Earth, and Le Sueur River Basins. (c) Elevation map of the basin and (d) slopes of the network. The approximate historical extent of Glacial Lake Minnesota (determined as the extent of the glaciolacustrine environment by *Hobbs and Goebel* [1982]) is outlined in (c) and shaded in (d). (caption continued on next page)

(caption for Figure 3.3 continued) The knickzone in the lower 40 km of the network from the basin outlet is identified in (d) as the highlighted portion of the network. (e) Traces along the network shown as (f) long profiles. The thin lines show the long profile for every link in the network to the outlet and a few traces are highlighted.

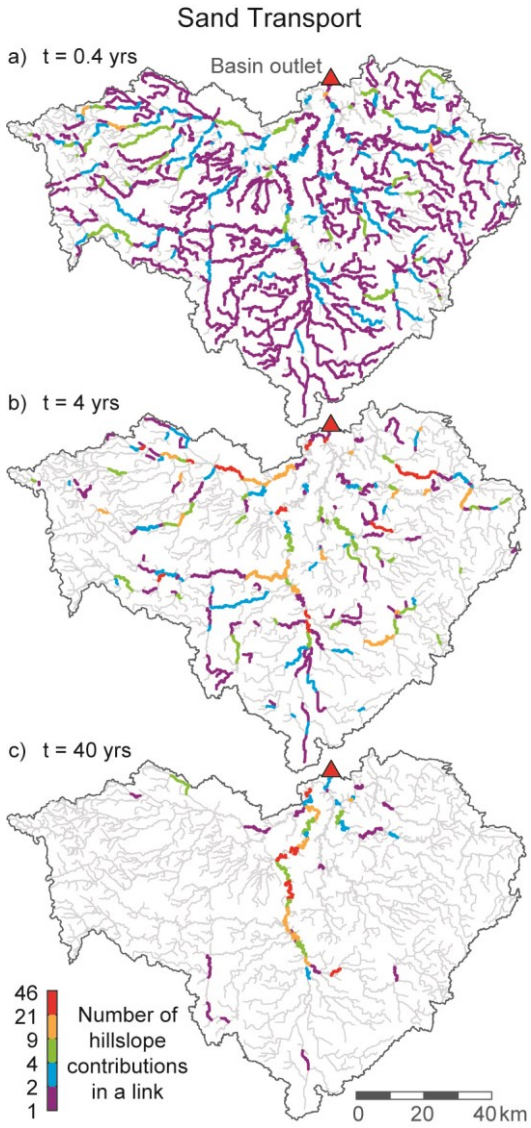

Figure 3.4. Sand transport on the Greater Blue Earth River Network. Organization of sand transported on the network at time (a) 0.4, (b) 4, and (c) 40 years after an instantaneous uniform input (each considered as a hillslope contribution) to all links of the network at $t = 0$.

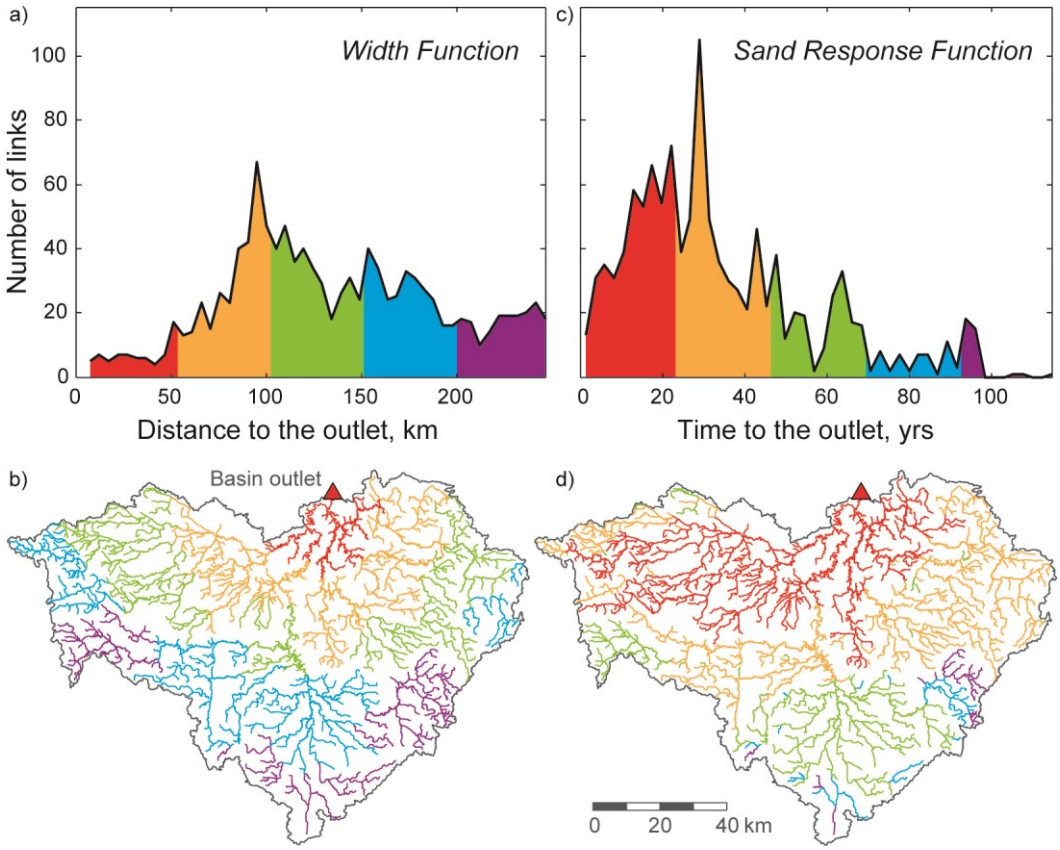

Figure 3.5. Distance and travel time distributions of each link to the outlet in the Greater Blue Earth River Network. The distance distribution of each link to the outlet was partitioned into different distance bands shown as (a) the network width function and (b) mapped spatially on the network. The travel time distribution of each link to the outlet was partitioned into different travel time bands shown as (c) the sand response function and (d) mapped spatially on the network. Colors correspond between (a) and (b) and separately for (c) and (d).

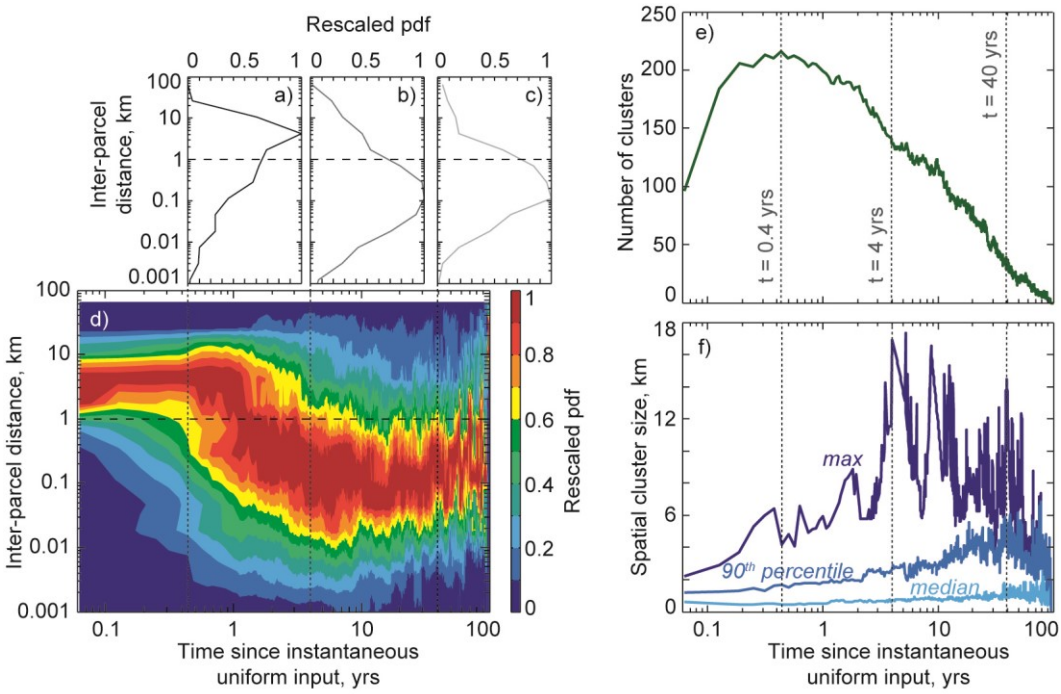

Figure 3.6. Temporal evolution of inter-parcel distance (distance between a parcel and its immediately downstream parcel) and cluster statistics. The rescaled probability distribution function (pdf) of inter-parcel distance (rescaled such that the mode of the pdf was set equal to 1) at time (a) 0.4, (b) 4, and (c) 40 years after an instantaneous uniform input at $t = 0$ to all links of the network. (d) Stacked pdfs of rescaled inter-parcel distance for all times to form a contour plot. The long-dashed horizontal line denotes the threshold distance (d^*) used in the (inter-parcel distance) cluster definition, i.e., two parcels less than d^* distance apart belong to the same cluster. (e) Number of clusters formed over time and (f) cluster size statistics of maximum, 90th percentile, and median spatial cluster size.

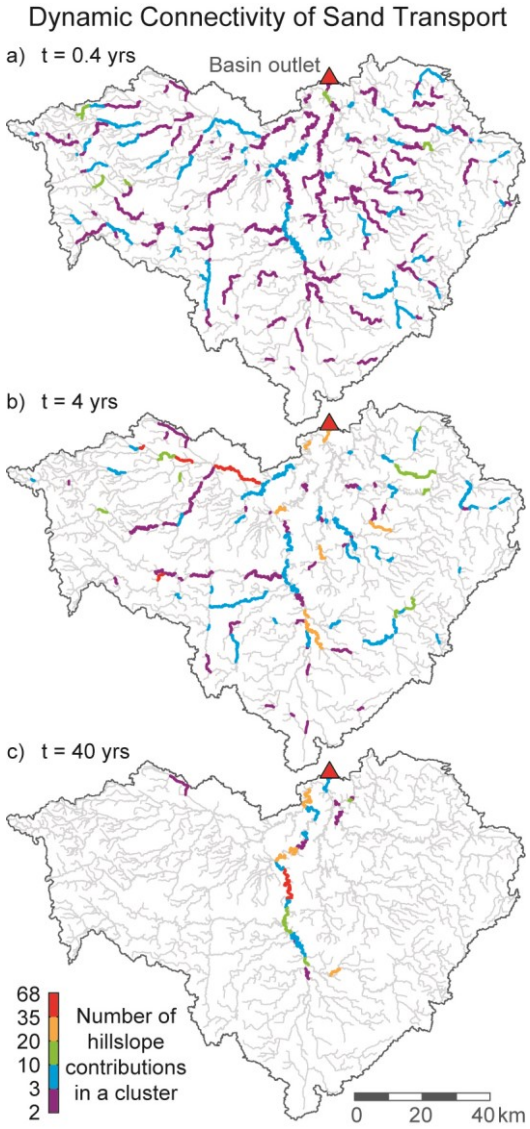

Figure 3.7. Dynamic connectivity of sand transport on the Greater Blue Earth River Network. Organization of sand transported on the network into clusters at time (a) 0.4, (b) 4, and (c) 40 years after an instantaneous uniform input (each considered as a hillslope contribution) to all links of the network at $t = 0$. Clusters were defined using an inter-parcel distance (distance between a parcel and its immediately downstream parcel) equal to 1 km although they are shown here as spanning entire links. The color corresponds to the number of hillslope contributions within each cluster.

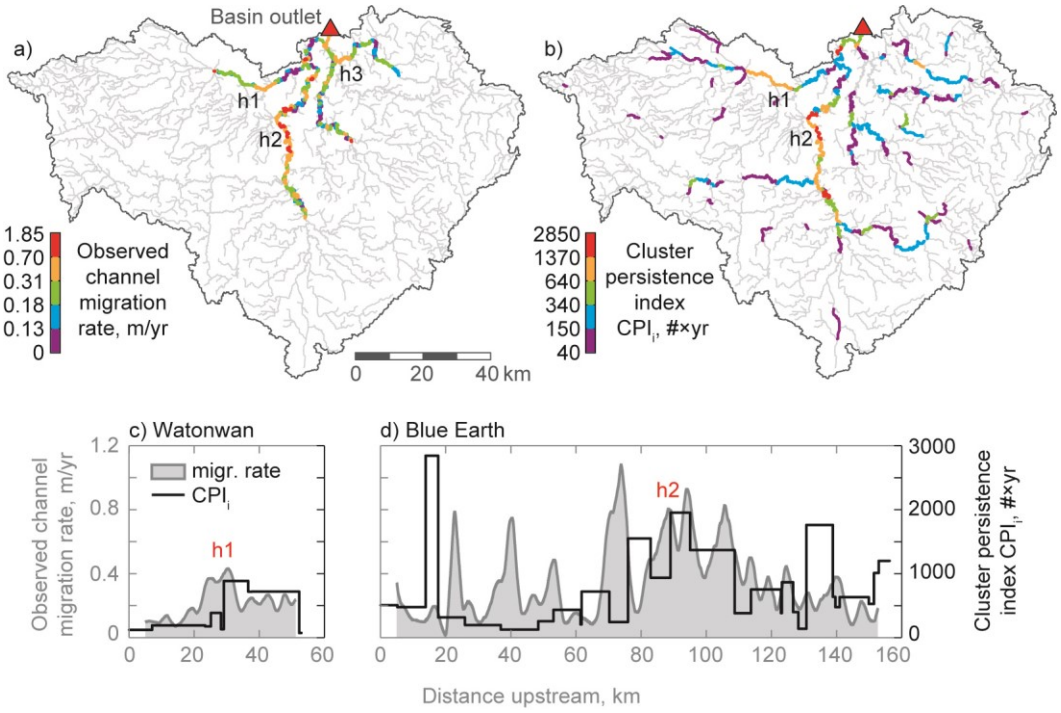

Figure 3.8. Identification of hotspots of fluvial geomorphic change in the Greater Blue Earth River Network using the cluster persistence index (CPI). (a) Observed channel migration rate 1938-2005 shown spatially averaged using a 5-km smoothing window [*Belmont et al.*, 2011; *Bevis*, 2015]. Hotspots (h1, h2, h3) of fluvial geomorphic change were defined as locations where the observed channel migration rate was much higher than was occurring throughout the rest of the basin. (b) CPI as computed by our model (see text for definition). High values of CPI coincide with hotspots h1 and h2 suggesting that CPI can be used to identify these hotspots of sediment-driven fluvial geomorphic change. Hotspot h3 (streamflow-driven) was not identified by CPI and reasons are discussed in the text (see also Figure 3.9). Detailed comparisons of the observed channel migration rate (shaded; corresponds to the left y-axis) and cluster persistence index (line; corresponds to the right y-axis) for the (c) Watonwan River which contains hotspot h1 and (d) Blue Earth River which contains hotspot h2.

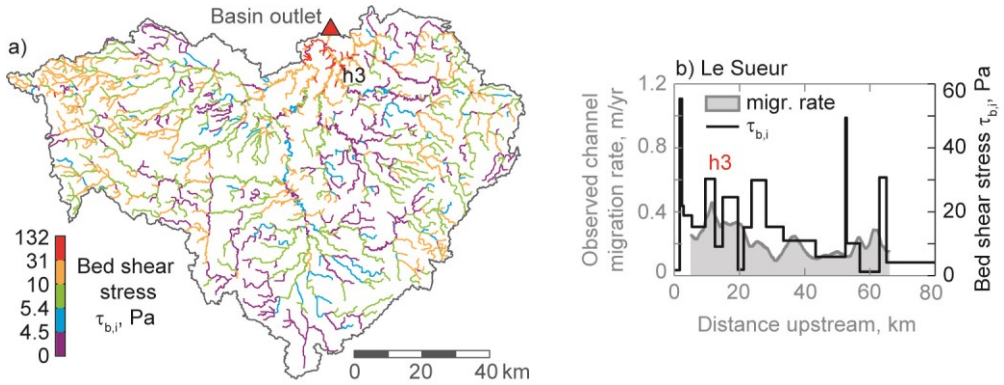

Figure 3.9. Identification of hotspot of fluvial geomorphic change in the Greater Blue Earth River Network using bed shear stress. (a) Bed shear stress at the two-year recurrence interval flow. Hotspot h3 of fluvial geomorphic change was defined as the location along the Le Sueur River where the observed channel migration rate was much higher than was occurring throughout the rest of the river (see Figure 3.8a). It is seen that the streamflow-driven hotspot h3 was well predicted by high values of bed shear stress. (b) Detailed comparison of the observed channel migration rate (shaded; corresponds to the left y-axis) and bed shear stress (line; corresponds to the right y-axis) for the Le Sueur River.

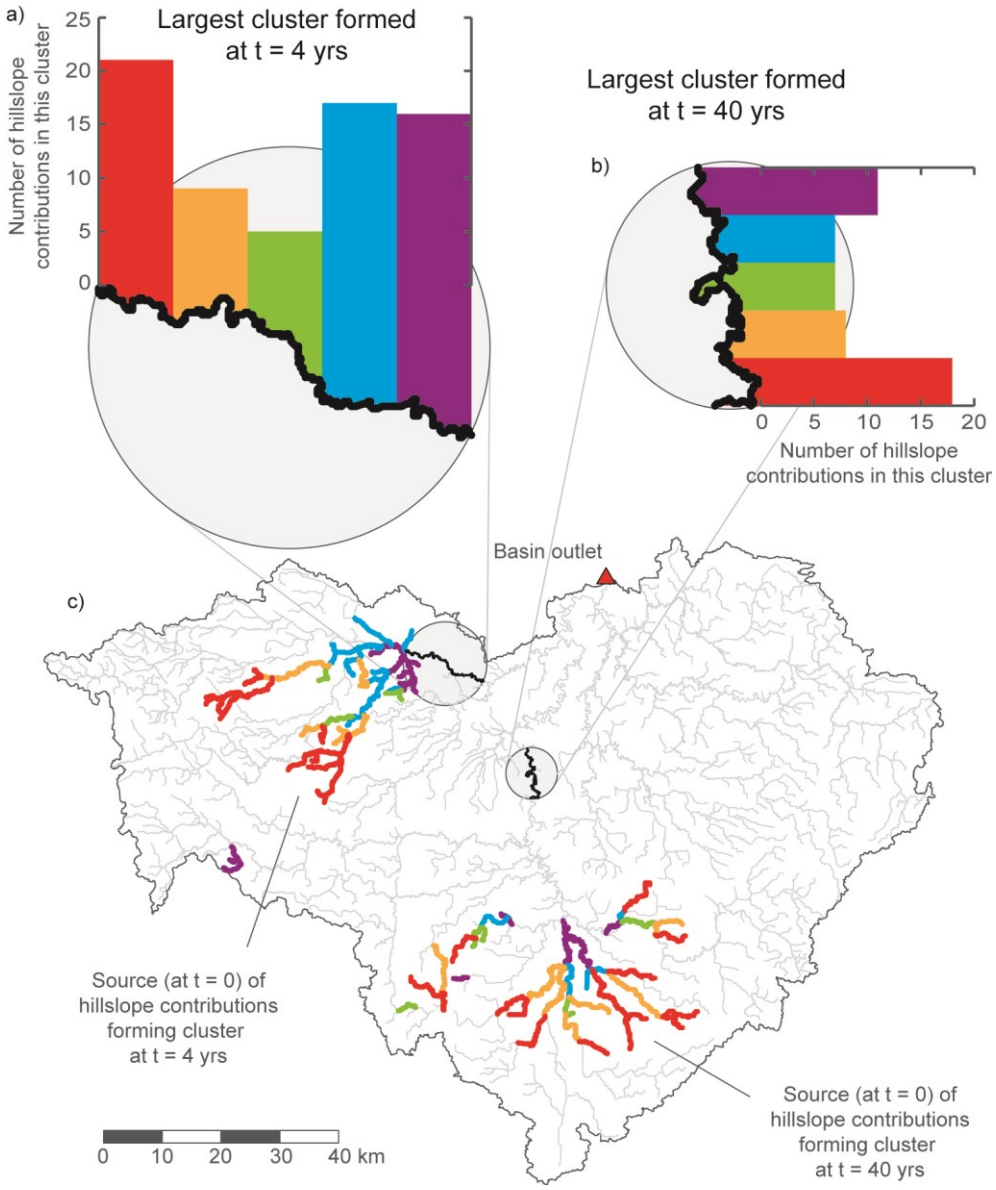

Figure 3.10. Unraveling the source contributions of two large clusters formed at different times. The largest cluster formed at time (a) 4 years (length ≈ 17 km) and (b) 40 years (length ≈ 15 km). The colored bars are the histogram of hillslope contributions within each cluster, where each color corresponds to a specific source area (at time 0) of the hillslope contributions composing the cluster, shown with the same colors in (c). This process-specific coarse-graining of the landscape allows the identification of space-time sources of sediment which eventually coalesce downstream due to the specific river network topology and flux dynamics.

Chapter 4

Interplay between Spatially-Explicit Sediment Sourcing, Hierarchical River-Network Structure, and In-Channel Bed-Material Sediment Transport and Storage Dynamics

High-resolution topography provides a basis for accurately mapping sediment sources, identifying pathways by which sediment moves through a watershed, and quantifying the physiographic characteristics of river channels and floodplains. Paired with field measurements, these data quantify the spatial distribution, magnitude, and frequency of sediment inputs to a basin, which may reveal a vastly heterogeneous potential for sediment generation that should be incorporated into watershed-scale, sediment-transport models. Herein, we present a network-based model for bed-material sediment that combines spatially-explicit sediment sourcing with in-channel transport and storage dynamics on a river network. We use the model to simulate the transport and storage of bed-material sand over a 600-year time period in the Greater Blue Earth River Basin in Minnesota. We show how to compute analytically the time-averaged bed-sediment thickness for each link of an entire river network for any spatial distribution of inputs, with or without accounting for in-channel storage. Under supply-limited conditions, we

show how to compute analytically the time-averaged pdf of bed-sediment thickness. Under transport-limited conditions, (1) the time-averaged pdf of bed-sediment thickness is heavy tailed where the magnitude of fluctuations depends on the strength of feedback between the volume of sediment placed in storage and the resulting slope and (2) the timeseries of bed-sediment thickness is periodic with dominant period inversely proportional to the volumetric flux, which sets the timescale for the bed to adjust. The timeseries of bed-sediment thickness is the result of dynamics on a network in propagating, altering, and amalgamating sediment inputs in sometimes unexpected ways.

4.1 Introduction

Near-channel sediment sources now dominate in many agricultural landscapes [*Belmont et al*., 2011; *Massoudieh et al*., 2013; *Kronvang et al*., 2013; *Neal and Anders*, 2015]. Studies employing a variety of approaches including bedload and suspended load monitoring, setting bank-erosion pins, aerial photograph analysis, and sediment fingerprinting have found near-channel erosion to dominate over agricultural field erosion in a range of environments from the Le Sueur River in southern Minnesota (2,880 km^2; 78% agriculture; 70% near-channel erosion of bluffs, banks, and ravines) [*Belmont et al*., 2011] to Mill Stream, a tributary of the Chesapeake Bay in Maryland (32 km^2; 74% agriculture; 83-99% bank erosion) [*Massoudieh et al*., 2013] to the River Odense in Denmark (486 km^2; 71% agriculture; 90-94% bank erosion) [*Kronvang et al*., 2013] to Wildcat Slough in central Illinois (61 km^2; 99% agriculture; 40-65% bank erosion) [*Neal and Anders*, 2015]. The finding that near-channel sediment sources often dominate may be surprising as sediment generated in agricultural landscapes has historically been primarily sourced from upland fields [*Trimble*, 1981, 1983; *Belmont et al*., 2011]. At least in the Le Sueur River Basin, an expansion and intensification of agricultural drainage has both decreased surface runoff and erosion and increased crop yields, but at the expense of delivering more water to ditches, streams, and rivers than in the past resulting in amplified streamflows and more erosive rivers [*Blann et al*., 2009; *Belmont et al*., 2011; *Schottler et al*., 2014; *Foufoula-Georgiou et al*., 2015].

As near-channel sediment sources become increasingly recognized as dominant in modern agricultural landscapes, the modeling frameworks used to simulate sediment transport at the watershed scale must also undergo a shift. Conventional watershed-scale, sediment-transport models have primarily been developed for use in agricultural landscapes, where upland soil erosion is assumed to be the primary sediment source. Such models estimate upland soil erosion using the universal soil loss equation [*Renard et al.*, 1997] and apply a sediment-delivery ratio to estimate watershed sediment yield (e.g., HSPF see *Shenk and Linker* [2013] and SWAT see *Gassman et al*. [2007]). While efforts have been made to incorporate near-channel sediment sources into these models, representation of sediment-transport processes remains nascent.

However, a few network-based modeling frameworks exist that can easily incorporate near-channel sediment sources [*Benda and Dunne*, 1997; *Jacobson and Gran*, 1999; *Wilkinson et al*., 2006; *Czuba and Foufoula-Georgiou*, 2014, 2015; *Gran and Czuba*, 2016; *Schmitt et al*., 2016]. The seminal work is that of *Benda and Dunne* [1997a] where stochastically-forced sediment inputs were routed through a 215 km^2 river network in the Oregon Coast Range via a sediment mass-balance approach. Distributed inputs to their network model included (1) landslides, debris flows, and fluvial scour from bedrock hollows in first and second order channels; (2) soil creep along the toe of hillslopes; (3) landslides from bedrock hollows that laterally enter a reach; and (4) bank erosion of debris-flow fans and terraces. *Jacobson and Gran* [1999] developed a simple network routing model of the 5,200 km^2 Current River Basin in the Ozarks of Missouri to explain how gravel inputs delivered to first-order channels through widespread land-use change and then subsequently routed through the network could explain the spatial distribution of gravel bars in the basin. *Wilkinson et al.* [2006] computed the spatial distribution of bed-material sediment accumulation in the 29,000 km^2 Murrumbidgee River Basin in southeast Australia by comparing the total bed-material sediment supply from gullies, river banks, and upstream tributaries against the sediment transport capacity in each reach.

More recently, the network-based framework of *Czuba and Foufoula-Georgiou* [2014, 2015] (see also chapter 2 and 3) was used to route sand-sized sediment through the

channel network of the 44,000 km^2 Minnesota River Basin (or a subbasin: the 9,200 km^2 Greater Blue Earth River Basin) in southern Minnesota via physically-based time delays quantified by physiographic and channel dynamic properties. While developments are still ongoing, this framework has the potential to incorporate any type of sediment input along the river network as well as storage processes. *Gran and Czuba* [2016] incorporated a sediment budget of the Greater Blue Earth River Basin [*Bevis*, 2015] along with an in-channel storage process into the network-based framework of *Czuba and Foufoula-Georgiou* [2014, 2015] primarily to assess how sediment pulses (in excess of a background supply) are affected by river-network structure. Additionally, the network-based CASCADE (CAtchment Sediment Connectivity And DElivery) modeling framework of *Schmitt et al.* [2016] identifies sediment cascades that establish the connectivity between a specific source and its multiple sinks. The CASCADE model was applied to the 51,000 km^2 Da River Basin within Vietnam, China, and Laos to quantitatively analyze the sediment connectivity of the basin. The work of *Schmitt et al.* [2016] provides some important new developments for network-based, sediment-transport models including the specification of the full grain-size distribution of bed-material sediment and adding so-called competition functions for determining which grain sizes to transport in a given reach.

With the availability of detailed topography from lidar data, we can accurately map the sources of sediment and pathways by which sediment moves through a watershed [*Passalacqua et al*., 2012, 2015]. In some basins, this may reveal a vastly heterogeneous potential for sediment generation (e.g., location of bluffs, ravines), and paired with field measurements, allows one to quantify the magnitude and frequency of sediment generation for all sediment-generating features identified on the landscape. Furthermore, physiographic characteristics of the channels (e.g., slope, width) can be extracted from the detailed topography to compute the rate of sediment movement through, and transport capacity of, various reaches. This is the essence of network-based, sediment-transport models which have the potential to explore synchronizations (see chapter 2), emergence of hotspots of geomorphic change (see chapter 3), and also test alternative scenarios for management decisions.

The purpose of this chapter is to develop a network-based model of bed-material sediment and extensively describe its implementation in the Greater Blue Earth River Basin in southern Minnesota. This model combines spatially-explicit sediment sourcing with in-channel transport and storage dynamics (Figure 4.1) within the network-based framework of *Czuba and Foufoula-Georgiou* [2014, 2015] described in chapters 2 and 3. We analytically derive the quasi-steady-state, spatio-temporal characteristics of bed-sediment thickness from the mechanistic underpinnings of the model and the hierarchical structure of the river network – all without the need for numerical simulations. We then use the model to simulate the transport and storage of bed-material sediment over a 600-year time period and the spatio-temporal characteristics of bed-sediment thickness. Furthermore, we use the model to isolate the influence of river-network structure on bed-material sediment dynamics in propagating, altering, and amalgamating the emergent, large temporal fluctuations and periodicities of bed-sediment thickness.

4.2 Network-Based Modeling Framework for Bed-Material Sediment

The network-based modeling framework described in chapter 2 is a first-order approach to understanding the transport dynamics of an environmental flux along a network by combining system connectivity with major transport and transformation processes. As applied to bed-material sediment herein, the result is a Lagrangian transport model of sediment on a river network (section 4.2.1) where sediment is supplied in space and time (section 4.2.2), transported downstream via physically-based time delays (section 4.2.3), and stored in-channel whenever transport capacity is exceeded (section 4.2.4). The resulting model of bed-material sediment lends itself to some analytical insights that are described in section 4.2.5. Basic elements of the model are described in this section; further details regarding the application of the model to the study basin are described in section 4.3.

4.2.1 Network of Connected Flowpaths

A network of connected flowpaths forms the basis of the model. Herein we focus on a river network conceptualized as a set of connected links. Each link i represents either a segment of river channel between tributaries and/or lakes or a lake that intersects the river network with each link associated with a set of unique topologic, physiographic, and hydrodynamic attributes. For instance, a river channel would have at least the following attributes: index of link i, index of upstream and downstream links, link length ℓ_i [L], directly contributing area a_i [L^2], upstream drainage area A_i [L^2] (i.e., the sum of a_i for all links upstream of and including link i), elevation of the bed at the upstream end of the link $\eta_{i,t}$ [L], and channel slope $S_{i,t}$; herein, both $\eta_{i,t}$ and $S_{i,t}$ vary in time, and thus include a subscript t. Additional attributes associated with transport and storage dynamics can be computed from or parameterized by these attributes (see sections 4.2.3, 4.2.4, and 4.3.4).

4.2.2 Spatial and Temporal Supply

An individual input to the network is referred to as a parcel, defined as an arbitrary volume V_p [L^3] or mass $\rho_s V_p$ [M] of sediment that conceptually moves through the system as a coherent unit (where ρ_s [ML^{-3}] is the sediment density). Spatially, parcels can be input anywhere along the length of any link. Temporally, these inputs can recur based on a specified interarrival time distribution.

4.2.3 Transport Dynamics

An individual parcel of sediment is conceptualized as moving through a link via a physically-based time delay. Herein, we summarize the travel-time derivation for bed-material sand transport from chapter 2 that represents the travel time $t_{s,i,t}$ [T] of a sand parcel to move through link i at a particular time t in the absence of storage (an additional time delay due to storage is handled separately and is described in section

4.2.4). This travel time $t_{s,i,t}$ was computed as the time it takes a sand parcel to move through a link of length ℓ_i at a bulk sand transport velocity $u_{s,i,t}$ [LT^{-1}] as

$$t_{s,i,t} = \frac{\ell_i}{u_{s,i,t}}. \tag{4.1}$$

The bulk sand transport velocity $u_{s,i,t}$ was obtained by decomposing an estimate of the volumetric transport rate of sand $Q_{s,i,t}$ [L^3T^{-1}] into a velocity and an area through which the majority of sand transport takes place as

$$u_{s,i,t} = \frac{Q_{s,i,t}}{(\theta_i H_i) B_i}, \tag{4.2}$$

where H_i [L] is the flow depth of link i, B_i [L] is the channel width of link i, and θ_i is a scale factor such that together $(\theta_i H_i)$ defines a characteristic vertical length scale for sand transport (guidance on the selection of θ_i is provided in section 2.4.5). Through equations for uniform (normal) flow hydraulics and *Engelund and Hansen's* [1967] sediment-transport formula, a volumetric transport rate of sand $Q_{s,i,t}$ can be estimated, substituted into equation (4.2), and the result rearranged (see chapter 2 for details) as

$$u_{s,i,t} = \frac{0.05}{\theta_i g^{1/2} R_i^2 D_i} u_{w,i}^2 H_i^{1/2} S_{i,t}^{3/2}, \tag{4.3}$$

where g [LT^{-2}] is the acceleration due to gravity, R_i is the submerged specific gravity of sediment in link i, D_i [L] is the sediment grain size in link i, and $u_{w,i}$ [LT^{-1}] is the streamflow velocity in link i.

Substitution of equation (4.3) into equation (4.1) yields

$$t_{s,i,t} = \frac{\theta_i g^{1/2} R_i^2 D_i}{0.05} \ell_i u_{w,i}^{-2} H_i^{-1/2} S_{i,t}^{-3/2} \tag{4.4}$$

which describes the travel time of a sand parcel through a link according to streamflow hydraulics specified by $u_{w,i}$ and H_i. While not explicitly stated, any variable can be specified as a function of spatial location for a given link i, vary with time t, or specified as a function of other variables/parameters. Only those variables that are allowed to vary

with time in the model described herein are given the time index t, although it is important to note that this is not restrictive to only these variables/parameters. This means that equation (4.4) or equation (4.3) can be used to simulate the transport of sediment under explicit time-varying hydraulics.

4.2.4 Storage Dynamics

Both lake and in-channel storage are simulated in the present model. Lakes directly connected to the channel network act as bed-material sinks, and thus any sand parcels that enter a lake are removed from the system. In-channel storage of parcels occurs whenever transport capacity is exceeded, the excess volume aggrades the bed and thus adjusts the slope and thereby affects transport. These storage dynamics were briefly described by *Gran and Czuba* [2016], but here we go into more mathematical detail.

The volumetric transport rate of sand $Q_{s,i,t}$ as computed from *Engelund and Hansen's* [1967] sediment-transport formula defines transport capacity. We can think about this transport capacity in the context of the model in a few different ways. By combining equations (4.1) and (4.2) and rearranging, the potential volumetric transport rate of sand or transport capacity can be written as

$$Q_{s,i,t} = \frac{\ell_i (\theta_i H_i) B_i}{t_{s,i,t}} \tag{4.5}$$

which is the volume of the active transport layer within a link divided by the travel time to move through that link. As sand parcels are transported along the network, at any time t we can determine the total volume of sand from all parcels in each link i and refer to this volume as $V_{s,i,t}$ [L^3]. Then, the most straightforward way to incorporate transport capacity is to conceptualize transport capacity as the maximum volume of sediment χ_i [L^3] that can be moved at any one time through a link i as

$$\chi_i = \ell_i (\theta_i H_i) B_i . \tag{4.6}$$

Alternatively, we can compute a bed-sediment thickness $h_{s,i,t}$ [L] as

$$h_{s,i,t} = \frac{V_{s,i,t}}{B_i \ell_i \left(1 - \lambda_p\right)} \tag{4.7}$$

where λ_p is the porosity of the bed-material sediment and the term $\left(1 - \lambda_p\right)$ effectively increases the volume occupied by the parcels on the bed due to pore space present in the subsurface deposit. All thicknesses associated with bed-material sediment herein include the $\left(1 - \lambda_p\right)$ term that accounts for sediment porosity of the resulting deposit. The equivalent bed-sediment thickness at capacity $H_{s,i}$ [L] (Figure 4.2a) is given by

$$H_{s,i} = \frac{\theta_i H_i}{\left(1 - \lambda_p\right)}. \tag{4.8}$$

At every time t the total parcel volume $V_{s,i,t}$ in each link i was compared to the volumetric transport capacity χ_i of that link. Whenever the total parcel volume exceeded transport capacity, the parcels contributing to the excess volume $V_{s,i,t}^{stor}$ [L^3] defined as

$$V_{s,i,t}^{stor} = \begin{cases} V_{s,i,t} - \chi_i, & \text{if } V_{s,i,t} > \chi_i \\ 0, & \text{otherwise} \end{cases} \tag{4.9}$$

are assigned to in-channel storage. Specifically, the first subset of parcels to arrive into the link (following first-in last-out) whose cumulative volume is at least $V_{s,i,t}^{stor}$, are assigned to a conceptual subsurface-storage layer by "freezing" those parcels' transport through the link (i.e., they did not move while in storage). Once other parcels exit the link additional parcels could return from storage to active transport (following last-in first-out), but only enough parcels as to not exceed transport capacity. This "freezing" of parcels above capacity results in an additional time delay to the travel time of a parcel through a link due to transport limitations associated with transient in-channel storage. Any parcels placed into in-channel storage can subsequently be released, allowing the bed to return to its initial profile. However, new sediment inputs were not generated from the bed during supply-limited conditions. Instead, the bed was assumed to be armored at its initial profile with a coarse lag deposit or by bedrock, and simulations then captured the dynamics of sand moving over a non-erodible substrate.

Whenever in-channel storage occurs, the excess volume or storage volume $V_{s,i,t}^{stor}$ is

placed in such a way as to increase the channel slope of link i where storage occurs and simultaneously decreases the channel slope in the two directly upstream channel links (referred to with link indices $u1$ and $u2$). Specifically, $V_{s,i,t}^{stor}$ is used to adjust the bed elevation $\eta_{i,t}$ at the upstream end of link i by conceptually placing this storage volume in one, two, or three wedges depending on the number of channel links directly upstream of link i (see Figure 4.2b). One wedge is located in link i, pinned at the downstream end, and its elevation was only adjusted at the upstream end ($\eta_{i,t}$). Additional wedges (one or two) were located in upstream channel links if those channel links existed; the elevation of the wedge in upstream links is only adjusted at the downstream end ($\eta_{i,t}$) and is pinned at the upstream end. The sediment parcels in storage always reside in link i, but this conceptual placement of that storage volume ensures continuity of bed elevations for computing slopes. Where there were two upstream channel links, the bed elevation $\eta_{i,t}$ is adjusted as

$$\eta_{i,t} = \eta_{i,0} + \frac{2V_{s,i,t}^{stor}}{\left(B_i \ell_i + B_{u1} \ell_{u1} + B_{u2} \ell_{u2}\right)\left(1-\lambda_p\right)} \tag{4.10}$$

where $\eta_{i,0}$ [L] is the initial elevation at the upstream end of link i at time $t = 0$. We assume sufficiently low slopes such that ℓ_i represents the three-dimensional distance between ends of a link is approximately equal to the two-dimensional horizontal distance between the ends of a link (Figure 4.2b). An initial elevation $\eta_{i,0}$ is used here rather than at the previous time step because $V_{s,i,t}^{stor}$ defines the total volume of sediment in storage and not the incremental volume. For the case of only one upstream channel link $u1$, equation (4.10) would only contain two $B\ell$ terms, instead of three, with indices i and $u1$; and in the absence of any upstream channel links, equation (4.10) would only contain the $B_i \ell_i$ term.

Once $\eta_{i,t}$ is computed for all links at time t, then the channel slope $S_{i,t}$ is updated everywhere as

$$S_{i,t} = \frac{\eta_{i,t} - \eta_{d,t}}{\ell_i} \tag{4.11}$$

where $\eta_{d,t}$ denotes the elevation at the downstream end of link i, as the index d denotes the index of the link directly downstream of link i. In this formulation the elevation of the downstream end of the most downstream link in the network (at the outlet) is fixed at its initial value through time. The change in slope affects the travel time $t_{s,i,t}$ via equation (4.4), which then affects the volumetric transport rate of sand or transport capacity via equation (4.5). It is important to note that in this formulation in-channel storage does not affect the volume of sediment transported at capacity χ_i, but alters the speed at which parcels move through a given channel link. The effects of storage are not only local to an individual link, but also propagate to channel links directly upstream.

4.2.5 Analytical Insights

At any time t, the bed-sediment thickness $h_{s,i,t}$ is composed of an active-transport layer $h_{s,i,t}^{act}$ [L] and a storage layer $h_{s,i,t}^{stor}$ [L] (see Figure 4.2a) as

$$h_{s,i,t} = h_{s,i,t}^{act} + h_{s,i,t}^{stor}. \tag{4.12}$$

Similarly, the time-averaged bed-sediment thickness $\overline{h}_{s,i}$ [L] is given by the sum of the time-averaged active-transport layer thickness $\overline{h}_{s,i}^{act}$ [L] and a time-averaged storage layer thickness $\overline{h}_{s,i}^{stor}$ [L] as

$$\overline{h}_{s,i} = \overline{h}_{s,i}^{act} + \overline{h}_{s,i}^{stor}. \tag{4.13}$$

Also note that

$$\overline{h}_{s,i}^{act} = \begin{cases} H_{s,i}, & \text{if } \overline{h}_{s,i}^{stor} > 0 \\ \overline{h}_{s,i} \le H_{s,i}, & \text{if } \overline{h}_{s,i}^{stor} = 0 \end{cases} \tag{4.14}$$

which states, on average, that whenever in-channel storage occurs the active layer transports sediment at capacity and whenever in-channel storage does not occur sediment is transported at a rate that is less than capacity.

When in-channel storage is not considered or if it is unimportant (i.e., not disrupting the transport of parcels through a link) in the present and upstream links, then we can compute the pdf of $h_{s,i,t}^{act}$ as $f\left(h_{s,i,t}^{act}\right)$, which for this case is equivalent to the pdf of $h_{s,i,t}$ as $f\left(h_{s,i,t}\right)$. When in-channel storage occurs, we can compute $\bar{h}_{s,i}$. However, if we shift the values of $f\left(h_{s,i,t}^{act}\right)$ by $\bar{h}_{s,i}^{stor}$ we preserve $\bar{h}_{s,i}$ and provide an estimate of $f\left(h_{s,i,t}\right)$ referred to as $\hat{f}\left(h_{s,i,t}\right)$, where the "^" denotes only an estimate, that assumes the in-channel storage process preserves the structure of a Poisson arrival process. This estimated pdf $\hat{f}\left(h_{s,i,t}\right)$ provides a useful baseline to compare against once in-channel storage becomes important and where subsequently the Poisson arrival process breaks down. Throughout the remainder of this section we describe how these aspects of bed-sediment thickness can be computed analytically without the need for numerical simulations. These analytical results are useful because they not only establish the mathematical relation between bed-sediment thickness, sediment supply, sediment transport, and channel characteristics, but also provide a way to obtain some results quicker and simpler through direct analytical computation rather than through numerical simulations.

We must first decompose an arbitrary magnitude input from a sediment-generating feature into a number of parcels each with volume V_p that are each then independently delivered to the network with an exponential interarrival time distribution with rate parameter λ [T^{-1}] (and thus mean and standard deviation of interarrival times equal to λ^{-1} [*Durrett*, 2012]). Breaking the inputs in this way means that the arrival of parcels to link i, including those generated internally and from upstream, will follow a Poisson arrival process with rate λ_i [T^{-1}] as

$$\lambda_i = n_i \lambda \tag{4.15}$$

where n_i is the total number of inputs of volume V_p upstream of link i but downstream of any lakes directly connected to the network (Figure 4.2c); because the sum of independent Poisson random variables is also Poisson with a rate that is the sum of the

rates of the individual Poisson random variables [*Durrett*, 2012].

At quasi-steady state, once a parcel arrives to a link it remains in that link, on average, for a duration of $\bar{t}_{s,i}$ [T], which is the time-averaged travel time for a sand parcel to move through a link. In the absence of in-channel storage, slope never changes, and thus $\bar{t}_{s,i}$ is equivalent to the initial travel time $t_{s,i,0}$ at time $t = 0$. According to the Poisson arrival process, the number of parcels N_i within link i for duration $\bar{t}_{s,i}$ is given by the Poisson distribution $f\left(k_p;\lambda_i\bar{t}_{s,i}\right)$ as

$$f\left(k_p;\lambda_i\bar{t}_{s,i}\right)=\Pr\left[N_i(t+\bar{t}_{s,i})-N_i(t)=k_p\right]=\frac{\left(\lambda_i\bar{t}_{s,i}\right)^{k_p}e^{-\left(\lambda_i\bar{t}_{s,i}\right)}}{k_p!} \tag{4.16}$$

where $k_p = 0, 1, 2, \ldots$ and with both mean and variance equal to $\lambda_i\bar{t}_{s,i}$ [*Durrett*, 2012]. The probability distribution function (pdf) of the bed-sediment thickness active-transport layer $f\left(h_{s,i,t}^{act}\right)$ is then just a scaled Poisson distribution as

$$f\left(h_{s,i,t}^{act}\right)=\frac{V_p f\left(k_p;\lambda_i\bar{t}_{s,i}\right)}{B_i\ell_i\left(1-\lambda_p\right)}. \tag{4.17}$$

On average, the volume of sediment in link i is given by $V_p\lambda_i\bar{t}_{s,i}$ and the quantity $V_p\lambda_i$ represents the volumetric supply rate of sediment to link i. Therefore, the time-averaged bed-sediment thickness of the active-transport layer $\bar{h}_{s,i}^{act}$ is given by

$$\bar{h}_{s,i}^{act}=\frac{V_p\lambda_i\bar{t}_{s,i}}{B_i\ell_i\left(1-\lambda_p\right)}=\frac{V_p n_i\lambda\bar{t}_{s,i}}{B_i\ell_i\left(1-\lambda_p\right)}. \tag{4.18}$$

These analytical results refer to the bed-sediment thickness of the active-transport layer because we must assume that $V_p\lambda_i$ is the average volumetric supply rate both arriving and departing at a given time. However for transport-limited links, the bed must first adjust in order to transport the supply.

We can compute how much the bed-sediment thickness would need to increase in order to pass the supply by the following iterative procedure. First we compute the relative capacity RC_i^{iter} of a given link i, where *iter* denotes the current iteration, by

comparing the rate of sediment supply to the rate of sediment transport as

$$RC_i^{iter} = \frac{V_p \lambda_i \widetilde{t}_{s,i}^{iter}}{\ell_i (\theta_i H_i) B_i}, \tag{4.19}$$

where $\widetilde{t}_{s,i}^{iter}$ [T] is the travel time for a sand parcel to move through a given link i that is iterated upon, as the "~" denotes an iterated value. The component of $\widetilde{t}_{s,i}^{iter}$ via equation (4.4) that is iterated upon is the slope $\widetilde{S}_i^{iter}$ and for the first iteration $\widetilde{S}_i^1$ is the initial slope $S_{i,0}$. The links where $RC_i^{iter} > 1$ will ultimately aggrade, so this identifies the channels that must adjust their slopes to pass the supply. This means that the volumetric transport rate of sand (equation 4.5) must adjust to balance the supply rate as

$$\frac{\ell_i (\theta_i H_i) B_i}{t_{s,i}^*} = V_p \lambda_i, \tag{4.20}$$

where $t_{s,i}^*$ [T] is the travel time for a sand parcel to move through a given link when transport balances supply, as the superscript "*" denotes a value computed when transport balances supply. The channel slope S_i^* that a link must adjust to in order to pass the sediment supply is given by substituting equation (4.4) into equation (4.20) and rearranging as

$$S_i^* = \left(\frac{V_p \lambda_i g^{1/2} R_i^2 D_i}{0.05 B_i u_{w,i}^2 H_i^{3/2}} \right)^{2/3}. \tag{4.21}$$

Thus wherever $RC_i^{iter} > 1$, the elevation $\widetilde{\eta}_i^{iter}$ [L] at the upstream end of the link must increase to achieve a slope of S_i^* as

$$\widetilde{\eta}_i^{iter+1} = \widetilde{\eta}_i^{iter} + \ell_i \left(S_i^* - \widetilde{S}_i^{iter} \right), \tag{4.22}$$

and for the first iteration $\widetilde{\eta}_i^1$ is the initial bed elevation $\eta_{i,0}$. Once all of the elevations have been adjusted for all links above capacity to $\widetilde{\eta}_i^{iter+1}$, then channel slope can be recomputed for the entire network via equation (4.11) to $\widetilde{S}_i^{iter+1}$. An increase in slope in one link simultaneously decreases the slope in the directly upstream links, and because

the subsequent decrease in slope may put that link above capacity, we have to iterate this procedure until $RC_i^{final} \le 1$. It is important to note that for links that have adjusted their slopes following this procedure, one must use the final iterated value for $\widetilde{t}_{s,i}^{final}$ (via $\widetilde{S}_i^{final}$) for $\bar{t}_{s,i}$ in order to accurately compute $f\left(h_{s,i,t}^{act}\right)$ via equation (4.17) and $\overline{h}_{s,i}^{act}$ via equation (4.18) in the context of in-channel storage.

In the formulation described herein, the same storage volume is converted into bed elevation and bed-sediment thickness in different ways. When this volume is converted into bed elevation for the purpose of adjusting channel slopes, we conceptually place that volume in three wedges (one in link i and the other two in upstream links; Figure 4.2b), but when we refer to that same storage volume in the context of bed-sediment thickness, we place the entirety of that storage volume uniformly across the bed of link i (Figure 4.2a). Through this iterative procedure we have calculated an adjusted bed elevation at which all links are capable of transporting the supply $\widetilde{\eta}_i^{final}$ that we now need to convert to the time-averaged bed-sediment thickness of the storage layer $\overline{h}_{s,i}^{stor}$ as

$$\overline{h}_{s,i}^{stor} = \frac{\left(\widetilde{\eta}_i^{final} - \eta_{i,0}\right)\left(B_i \ell_i + B_{u1} \ell_{u1} + B_{u2} \ell_{u2}\right)}{2 B_i \ell_i} . \tag{4.23}$$

4.3 Application to the Greater Blue Earth River Basin

The network-based modeling framework for bed-material sediment was applied to the Greater Blue Earth River Basin. The landscape setting is first described in section 4.3.1. Details on the application of the framework to this basin include a description of the river network (section 4.3.2), the specific spatial distribution and magnitude of sediment inputs derived from a sediment budget (section 4.3.3), and the transport and storage dynamics (section 4.3.4). This section ends with an overview of model simulations (section 4.3.5).

4.3.1 Landscape Setting

The Greater Blue Earth River Basin includes the Le Sueur River Basin and drains 9,200 km^2 of southern Minnesota and northern Iowa to the Minnesota River (Figure 4.3). The basin was glaciated multiple times throughout the Pleistocene, the effects of which exert considerable control on geomorphic dynamics today [see *Ojakangas and Matsch*, 1982 and *Gran et al*., 2013]. During glacial retreat, a proglacial lake, known as glacial Lake Minnesota, formed across a large portion of the Greater Blue Earth River Basin depositing fine surficial sediments [*Ojakangas and Matsch*, 1982]. When glacial Lake Agassiz drained through its southern outlet 13,400 years ago to carve the present-day Minnesota River valley [*Clayton and Moran*, 1982], the base-level of the Greater Blue Earth River was lowered by roughly 70 m. This lowering created a knickpoint, or sharp increase in channel slope, at the outlet of the river that has since migrated 40-60 km upstream (Figure 4.3), leaving a rapidly incising knickzone in its wake [*Gran et al.*, 2009, 2013; *Belmont*, 2011; *Belmont et al.*, 2011].

Like many Midwestern U.S. landscapes, agriculture is the dominant (85%) land-use in the basin [*Jin et al*., 2013]. Many of the wetlands that once dotted the landscape have been drained beginning in the late 1800s by surface ditches and subsurface drain tiles. The extensive subsurface drainage system has reduced surface erosion from upland fields, but at the expense of amplifying streamflows, accelerating near-channel erosion of downstream banks and bluffs, and initiating stream morphologic changes such as channel widening [*Belmont et al.*, 2011; *Lenhart et al*., 2013; *Schottler et al.*, 2014; *Foufoula-Georgiou et al*., 2015]. While the Greater Blue Earth River Basin has historically exported a large amount of sediment compared to surrounding basins, the amount of sediment deposited downstream in Lake Pepin has increased by about an order of magnitude in just over a century [*Kelley and Nater*, 2000]. This is in part due to the presence of large bluffs adjacent to the river that make sediment generation in the basin highly sensitive to changes in streamflow. However, turbidity is just one of many water-quality impairments in the basin [*MPCA*, 2014] contributing to a decline in macroinvertebrates, sensitive fish species, and native mussels [*Kirsch et al*., 1985;

Musser et al., 2009; *Carlisle et al*., 2013; *Hansen et al*., 2016].

4.3.2 Network of River Channels and Lakes

The underlying structure of the model is the river network, obtained from the National Hydrography Dataset Plus Version 2 (NHDPlusV2) [*McKay et al.*, 2012; *Horizon Systems*, 2014]. Lakes were obtained from the waterbody feature of the NHDPlusV2 dataset [*McKay et al.*, 2012; *Horizon Systems*, 2014]. Only lakes that intersect the river network and have surface area >0.04 km^2 were incorporated into the network as individual lake links (Figure 4.3). The NHDPlusV2 network was preprocessed by (1) clipping to the extent of the Greater Blue Earth River Basin; (2) removing isolated and secondary channels; (3) establishing a new set of links with index i, with a link defined between tributary junctions, as the intersection of a lake with the network, or between a lake and a junction; and (4) mapping or computing attributes for each link from the original NHDPlusV2 network. The final network was composed of 1,360 links including 107 lakes.

4.3.3 Inputs from a Sediment Budget

Fine sediment (silt and clay) budgets of the Greater Blue Earth River Basin [*Bevis*, 2015] and the Le Sueur River Basin [*Gran et al*., 2011a; *Belmont et al*., 2011] constrain the location, magnitude, and frequency of sediment inputs from bluffs, streambanks, ravines, and uplands (mainly low-gradient agricultural fields). Bed material throughout the Greater Blue Earth River Basin is primarily sand and only sand is represented in the model. Grain-size distributions measured for all sediment source areas were used to estimate sand inputs based on sources in the fine sediment budget. Although gravel in the bed material can play a role in setting bed roughness and in slowing channel incision [*Gran et al.*, 2013], gravel is only a small portion of the bedload and is not tracked here. Inputs from bluffs, ravines, and uplands (Figure 4.4) are incorporated into the present model. Net sediment contributions from streambank erosion and floodplain deposition are a smaller component of the sediment budget. Representation of these exchange

dynamics requires further developments of the model [e.g., *Lauer and Willenbring*, 2010; *Viparelli et al*., 2013; *Lauer et al*., 2016] and is beyond the scope of the present study.

4.3.3.1 Bluffs

Bluffs were defined in this basin by *Belmont et al.* [2011] as areas along active channels that had greater than 3 m of relief within a 9 m × 9 m moving window. Bluffs in the Greater Blue Earth River Basin are as tall as 70 m and flank roughly 50% of the active-channel corridor within the knickzone. Bluffs separated from the river channel by terraces were excluded from the sediment source inventory (Figure 4.4). Nearly 3,500 individual bluffs were mapped from 3 m lidar data in the Greater Blue Earth River Basin. According to the sediment budget [*Gran et al*., 2011a; *Belmont et al*., 2011; *Bevis*, 2015], the mass erosion rate of sand from each bluff ($M_{s,b}$ [MT^{-1}] in Mg/yr; where the subscript s denotes sand and the subscript b denotes a bluff) was calculated as

$$M_{s,b} = e_b A_b f_{s,till} \rho_{till} \tag{4.24}$$

where e_b [LT^{-1}] is the long-term, subbasin-average bluff erosion rate in m/yr (ranging from 0.05 to 0.25 m/yr) determined through repeat aerial photo analysis of bluff crests between 1938 and 2005 or 2008 as described in *Day et al.* [2013] and *Bevis* [2015], A_b [L^2] is the individual bluff surface area projected onto a vertical plane in m^2, $f_{s,till}$ is the fraction of sand in the till (0.35), and ρ_{till} [ML^{-3}] is the average bulk density of the till (1.8 Mg/m^3). Even though all bluffs are not composed of till, we treat them as such with minimal error. The total mass erosion rate of sand from all bluffs in the Greater Blue Earth River Basin was computed as 270,000 Mg/yr and was spatially distributed according to Figure 4.5a.

4.3.3.2 Ravines

Ravines were defined in this basin by *Belmont et al.* [2011] as steep ephemeral channels that connect the low-gradient uplands to deeply-incised valleys. Ravines deliver most of their sediment load during high-magnitude precipitation events before crops are fully

established in spring and early summer and are often dry by late summer. Nearly 340 individual ravines were mapped from 3 m lidar data in the Greater Blue Earth River Basin (Figure 4.4). Field monitoring of five ravines in the lower Le Sueur River Basin as part of the sediment budgeting work by *Belmont et al.* [2011] was used to determine an average annual ravine yield. According to the sediment budget [*Gran et al*., 2011a; *Belmont et al*., 2011; *Bevis*, 2015], the mass erosion rate of sand from each ravine ($M_{s,r}$ [MT^{-1}] in Mg/yr; where the subscript r denotes a ravine) was calculated as

$$M_{s,r} = A_r Y_r f_{s,till} \tag{4.25}$$

where A_r [L^2] is the incised area of an individual ravine in m^2 and Y_r [ML^2T^{-1}] is the average annual ravine yield (0.0034 $Mg/m^2/yr$) set as a constant for all ravines. Not all ravines incise through till, but are treated as such with minimal error. The total mass erosion rate of sand from all ravines in the Greater Blue Earth River Basin was computed as 24,000 Mg/yr and was spatially distributed according to Figure 4.5b.

4.3.3.3 Uplands

Uplands contribute sediment primarily from agricultural fields. Each link has a corresponding upland area for a total of 1,360 upland areas. An analysis of total suspended solids data measured at two gages upstream of the knickzone in the Le Sueur River Basin combined with sediment fingerprinting as part of the sediment budgeting work by *Belmont et al.* [2011] was used to determine an average annual upland yield. According to the sediment budget [*Gran et al.*, 2011a; *Belmont et al*., 2011; *Bevis*, 2015], the mass erosion rate of sand from each upland area ($M_{s,u}$ [MT^{-1}] in Mg/yr; where the subscript u denotes an upland) was calculated as

$$M_{s,u} = a_i Y_u f_{s,soil} \tag{4.26}$$

where a_i is the upland area or incremental contributing area to link i in m^2, Y_u [ML^2T^{-1}] is the annual upland yield (0.00002 $Mg/m^2/yr$) set as a constant for all uplands, and $f_{s,soil}$ is the fraction of sand in the soil (either 0.10 for glaciolacustrine deposits, 0.35 for glacial till, or 0.50 for glacial outwash and Holocene alluvium; *STATSGO2* [2015], see Figure

4.5c). The total mass erosion rate of sand from all uplands in the Greater Blue Earth River Basin was computed as 57,000 Mg/yr and was spatially distributed according to Figure 4.5c. Note that the extent of glaciolacustrine deposits reflects the approximate historical extent of glacial Lake Minnesota.

4.3.4 Transport and Storage Dynamics

Herein, hydraulic geometry relations were used to parameterize $u_{w,i}$ and H_i at bankfull flow (specifically at the two-year recurrence interval peak flow) as a function of upstream drainage area A_i. With the streamflow hydraulics held as a constant bankfull, the travel time in equation (4.4) was converted to real time through an intermittency factor $I_{f,s}$ [*Paola et al.*, 1992; *Parker*, 2004] that denotes the fraction of time per year that continuous bankfull flow would yield the mean annual sand load (see chapter 2 for details). Therefore, equation (4.4) becomes

$$t_{s,i,t} = \frac{\theta_i g^{1/2} R_i^2 D_i}{0.05 \alpha_{u_w A}^2 \alpha_{HA}^{1/2} I_{f,s}} \ell_i A_i^{-(2\beta_{u_w A} + \beta_{HA}/2)} S_{i,t}^{-3/2} \tag{4.27}$$

where $\alpha_{u_w A}$ and α_{HA} are empirically derived coefficients and $\beta_{u_w A}$, and β_{HA} are empirically derived exponents of the hydraulic geometry scaling relations for flow velocity and depth. In this way, bed-material sediment transport is decoupled from the daily variability of streamflow hydraulics, which greatly simplifies the calculations. The result averages over the intermittent short periods with intense transport and long periods with low transport to provide a continuous long-term (more than tens of years) probabilistic-average transport of sediment.

The travel time $t_{s,i,t}$ of a sand parcel to move through a link was reduced to a function of only network properties by assigning parameters specific to the Greater Blue Earth River Basin. These parameters included: g = 9.81 m·s^{-2}, θ_i = 0.1 ($\forall i$; assuming the majority of sand transport occurs in the lower 10% of the flow depth, see also section 2.4.5), R_i = 1.65 ($\forall i$), D_i = 0.0004 m ($\forall i$; D50 size of sand from riverbed material

[*U.S. Geological Survey*, 2014]), $\alpha_{u_w A}$ = 0.20, $\beta_{u_w A}$ = 0.07, α_{HA} = 0.0029, β_{HA} = 0.29 (computed at the two-year recurrence interval peak flow and using streamflow and channel cross-sectional properties of 23 stations; here A_i is specified in m^2, H_i in m, and $u_{w,i}$ in m·s^{-1}; see section 2.4.3 for details), and I_f = 0.175 (computed from a flow-duration curve; see section 2.4.4 for details). Substituting these parameters into equation (4.27) reduces the travel time $t_{s,i,t}$ to

$$t_{s,i,t} = 18\ell_i A_i^{-0.285} S_{i,t}^{-3/2}, \tag{4.28}$$

where ℓ_i is specified in meters and thus $t_{s,i,t}$ is given in seconds.

For storage in lakes, upstream drainage area and lake volume were used to compute, through an empirical relation, trapping efficiencies for fine sediment [*Brown*, 1943; *Bevis*, 2015]. The average fine sediment trapping efficiency for the lakes included in the model was 91% [*Bevis*, 2015]. Thus, the sand trapping efficiency for these lakes was assumed at 100% and any sand parcels that entered a lake were removed from the system.

4.3.5 Overview of Simulation

The model simulation began at time t = 0 and ran for 600 years. Sediment parcels were introduced independently to each link according to the spatial pattern and magnitude as specified by the sediment budget (Figure 4.5d) with parcel volume V_p = 10 m^3 for all parcels and following an exponential interarrival time distribution with λ = 1 yr^{-1} (to align with annualized sediment budget input volumes). For example, an input with rate of 63 m^{3}yr^{-1} would be broken into six parcels each as independent inputs recurring through time with interarrival times randomly selected from an exponential distribution with a mean of one year. Parcels can be input each with different magnitude (e.g., 63 m^{3}yr^{-1}), but were input in this way to match the assumptions of constant parcel volume, independent inputs, and equivalent interarrival time distributions used in deriving the analytical results. The parcel volume was selected to balance a volume as small as

possible with a computationally manageable number of parcels; over 600 years nearly eight million parcels were tracked through the system.

The time step in the model was set at 18.25 days so that 20 time steps yielded one year. Parcels were tracked as they moved through each link according to a time delay given in equation (4.28); the average travel time through a link was just over one year. If at any time there were more parcels in a given link than could be moved at capacity (equation 4.9), then a subset of parcels would enter in-channel storage, and the slope of that link and directly upstream links would be adjusted at the next time step. It took less than 200 years for an input at the farthest location to exit the basin at the outlet, for the bed sediment to build up in channel links, and for the bed adjustment to achieve quasi-steady state. Thus, all statistics computed from the simulation model only include results between time 200 and 600 years.

Mass of sediment was interchanged into volume of sediment using a sediment density ρ_s = 2.65 Mg/m^3, and a bed-sediment porosity λ_p = 0.4 [*Wu and Wang*, 2006] was applied in order to determine bed-sediment thickness. A minimum channel slope of 0.00001 was imposed in the model. Also the effect of Rapidan Dam, located on the Blue Earth River near the basin outlet, was removed by selecting a channel slope for the links upstream and downstream of the dam that linearly connected the bed elevations between unaffected upstream and downstream points. Bed elevations were then recomputed from the basin outlet in order to establish consistency between $\eta_{i,0}$ and $S_{i,0}$. A lower limit for transport capacity, set as the maximum volume of sediment χ_i that can be moved at any one time through a link (equation 4.6), was set at 50 m^3 so at least a few parcels could move through a link at any time. Due to the presence of some very short links in the network (<300m) that arose between closely-spaced tributaries, some links had a very small capacity resulting in an artificial "bottleneck" in the network. To circumvent this issue, a minimum capacity for these short links was set as the maximum of (i) the capacity of the link computed via equation (4.6), (ii) the capacity of directly upstream links, or (iii) 100 m^3.

The simulation model as described herein with distributed inputs routed through the

network and with in-channel storage is referred to as the "network, in-channel storage" model. To confirm the analytical results, we also ran the model with the in-channel storage mechanism turned off and we refer to this as the "network, no in-channel storage" model. To isolate the role of network hierarchical structuring, we maintain the full dynamics described in the "network, in-channel storage" model, but isolate each link from any potential non-Poissonian arrival of inputs and refer to this as the "single link, in-channel storage" model. Specifically, we treat each link in isolation by directly supplying inputs to that link following a Poisson arrival process with an exponential interarrival time distribution with parameter λ_i given by equation (4.15) that accounts for the amount and rate of supply from upstream and directly to the link, but without any temporal restructuring of parcels potentially happening farther upstream due to the in-channel storage process. The storage reservoir for adjusting the slope of the link still accounts for the width and length of directly upstream reaches (as in equation (4.10) and Figure 4.2b). Although the downstream end of the link remains fixed and thus any in-channel storage in the directly downstream link is not allowed to affect the slope of any upstream links.

4.4 Analytical and Simulated Bed-Material Sediment Dynamics

To first verify that the model was working as expected, the "network, no in-channel storage" model was run. Interarrival times of sediment parcels to each link in the network arrived following an exponential distribution with parameter λ_i as in equation (4.15). Additionally, the number of parcels within each link (or bed-sediment thickness) had a Poisson distribution with parameter $\lambda_i \bar{t}_{s,i}$ as in equation (4.16) (results not shown).

Before running the model the initial ratio of sand supply relative to transport capacity $RC_i^{iter=1}$ (equation 4.19) was computed to show where in the network transport capacity was exceeded (Figure 4.6a). Following the iterative procedure outlined in

section 2.5, bed elevations and thus slopes were adjusted until $RC_i^{final} \leq 1$, for this basin four iterations were necessary. The links where sediment accumulates and increases channel slope are identified in Figure 4.6b by the bed-sediment thickness of the storage layer $\overline{h}_{s,i}^{stor}$. Although not indicated, the links directly upstream of the links identified in Figure 4.6b have lower slopes due to the adjustment in bed elevation. The final RC_i^{final} values where bed elevations have been adjusted throughout the network are shown in Figure 4.6c. Note that any $RC_i^{iter=1} > 1$ in Figure 4.6a are the locations where sediment is stored as $\overline{h}_{s,i}^{stor}$ in Figure 4.6b and whose RC_i^{final} values become equal to one in Figure 4.6c.

Model simulations for the "network, in-channel storage" model of bed-sediment thickness are shown in Figure 4.7. The mean bed-sediment thickness $\overline{h}_{s,i}$ throughout the river network shows that reaches along the mainstem rivers just upstream of the knickzone accumulate bed-material sediment (Figure 4.7a; shown as analytical mean bed-sediment thickness). The simulated mean bed-sediment thickness confirms the analytical result (Figure 4.7b). The reaches with relatively greater bed-sediment thickness (under a temporally-recurrent forcing, spatially distributed according to Figure 4.5) are consistent with those areas identified in chapter 3 as hotspots of channel migration.

In-channel storage considerably alters the structure of the timeseries of bed-sediment thickness from that expected from the structure of the inputs (shown for four channel links of the network in Figure 4.7c-f). Where in-channel storage does not play a large role, the pdf $f\left(h_{s,i,t}\right)$ of simulated bed-sediment thickness (solid bars) is nearly the same as the estimated pdf $\hat{f}\left(h_{s,i,t}\right)$ assuming no in-channel storage (dashed line; Figure 4.7e). However, where in-channel storage does play a large role, the pdf of bed-sediment thickness is very different from $\hat{f}\left(h_{s,i,t}\right)$ estimated from a Poisson distribution. Periodicities are created in the timeseries (Figure 4.7c, d, and f) with different timescales that are much greater than that of the sediment supply forcing timescale of one year. The pdfs $f\left(h_{s,i,t}\right)$ of simulated bed-sediment thickness also have much heavier tails than

would be predicted by a Poisson distribution. In fact, an asymmetric pdf with a very long tail was found for the link highlighted in Figure 4.7f, which looks much different in character than the others shown, and a tri-modal pdf was found for the link highlighted in Figure 4.7d, related to its close proximity to a few major upstream tributaries. For much of the remainder of this chapter, we focus on describing the characteristics of the system that give rise to the emergent behavior of bed-sediment thickness, specifically heavy tails in the pdf and periodicity in the timeseries.

In order to separate the temporal variability of bed-sediment thickness that is internally generated by a single link from the variability that is propagated, amplified, or dampened from upstream links in the network, simulation results from the "single link, in-channel storage" model were compared to those from the "network, in-channel storage" model. Recall that for a Poisson distribution with parameter $\lambda_i \bar{t}_{s,i}$, the mean and variance are both equal to $\lambda_i \bar{t}_{s,i}$. Thus, the coefficient of variation (*COV*) defined as the ratio of the standard deviation to the mean is given by

$$COV = \frac{\sqrt{\lambda_i \bar{t}_{s,i}}}{\lambda_i \bar{t}_{s,i}} = \left(\lambda_i \bar{t}_{s,i}\right)^{-1/2}. \tag{4.29}$$

Where in-channel storage is unimportant, the *COV* of simulated bed-sediment thickness should follow equation (4.29). The *COV* of simulated bed-sediment thickness computed from the "network, in-channel storage" model and from the "single link, in-channel storage" model follows equation (4.29) for many links (Figure 4.8a; each point represents one link). But a number of links deviate from this line indicating that their temporal variability of bed-sediment thickness is much larger than for the estimated pdf $\hat{f}\left(h_{s,i,t}\right)$ assuming no in-channel storage, i.e., the in-channel storage process is responsible for creating larger temporal variability of bed-sediment thickness. We have quantified this deviation *dCOV* by the relative difference between the *COV* of simulated bed-sediment thickness and the *COV* predicted by equation (4.29) (Figure 4.8b) as

$$dCOV = \frac{\dfrac{\sigma_{h_s,i}}{\bar{h}_{s,i}^{act}} - \left(\lambda_i \bar{t}_{s,i}\right)^{-1/2}}{\left(\lambda_i \bar{t}_{s,i}\right)^{-1/2}}, \tag{4.30}$$

where $\sigma_{h_s,i}$ [L] is the standard deviation of the simulated bed-sediment thickness $h_{s,i,t}$. The mean of the simulated bed-sediment thickness of the active-transport layer $\bar{h}_{s,i}^{act} = \bar{h}_{s,i} - \bar{h}_{s,i}^{stor}$ is used rather than $\bar{h}_{s,i}$ because the variability of $\sigma_{h_s,i}$ is related to $\bar{h}_{s,i}^{act}$ for a Poisson distribution (recall discussion in section 4.2.5).

The deviation *dCOV* from only the "single link, in-channel storage" model simulations was then plotted against other variables (Figure 4.8c-d) to understand what internal link factors led to the emergence of such large temporal variability in bed-sediment thickness. Perhaps unsurprisingly, we see that the deviation *dCOV* arises in links at capacity (Figure 4.8c), confirming that the in-channel storage process, which is activated most often for links at capacity, is responsible for creating large temporal variability of bed-sediment thickness. Furthermore, if we select those links for which the relative capacity RC_i^{final} is greater than 0.995 (shown in the inset of Figure 4.8c), we see that the magnitude of *dCOV* is proportional to $\ell_i\left(B_i\ell_i + B_{u1}\ell_{u1} + B_{u2}\ell_{u2}\right)$ (Figure 4.8d), which is the term that determines the strength of the feedback between the volume of sediment in storage and the resulting slope (related to the term in equation (4.10), the extra ℓ_i arises due to the conversion from bed elevation to slope via equation (4.11)).

Each link in the network was classified based on its temporal variability of bed-sediment thickness from the "network, in-channel storage" model and from the "single link, in-channel storage" model. Links with a *dCOV* greater than a value of 0.2 (see dashed line in Figure 4.8b) are referred to as having a large variability or variability greater than Poisson, and less than this value are referred to as having variability consistent with the Poisson distribution $\hat{f}\left(h_{s,i,t}\right)$ assuming no in-channel storage or Poisson variability for short. Each link was then classified (Figure 4.8e) as either: *Generator* – links for which both models showed variability greater than Poisson; *Propagator* – links for which the network model showed variability greater than Poisson

but not so for the single-link model; *Unrealized* – links for which the single-link model showed variability greater than Poisson but not so for the network model; or *Poisson* – links for which both models showed Poisson variability. Note that the generators in Figure 4.8e are the locations at capacity shown in Figure 4.6c. Propagators are downstream of generators as these links are largely transmitting the structure of the supply from upstream. Links classified as unrealized are also generally downstream of generators where the structure of the supply from the upstream network has been altered in such a way to prevent the temporal variability of bed-sediment thickness from becoming greater than Poisson.

An asymmetric distribution of bed-sediment thickness about the mean (as seen in Figure 4.7f) arises wherever bed elevation returns to its initial value $\eta_{i,0}$. Thus, when the channel slope of this link returns to its initial value $S_{i,0}$ (Figure 4.9b) the bed-sediment thickness does not decrease further, resulting in an asymmetry (Figure 4.9a). To show that this is in fact responsible for the asymmetry, we reran the simulation with an initial slope of $S_{i,0}/2$. By doing so, the bed must first build up and increase the slope enough to pass the sediment supply. The bed ultimately builds up to a level where fluctuations in bed elevation never return to the initial bed elevation, and the result is that the bed-sediment thickness becomes symmetric about the mean (Figure 4.9c-d). We also note that the pdf of bed-sediment thickness (Figure 4.9c) remains heavy tailed.

The tri-modal distribution $f\left(h_{s,i,t}\right)$ of bed-sediment thickness seen in Figure 4.7d (also shown in Figure 4.10a) arises due to the creation, alteration, and propagation of the structure of the sediment supplied from upstream. Just upstream of this link, we see similar periodicity in bed-sediment thickness but with a bimodal distribution (Figure 4.10b) and also the other directly upstream link has variability consistent with the Poisson distribution $\hat{f}\left(h_{s,i,t}\right)$ assuming no in-channel storage (classified as Poisson; see Figure 4.10h). The amalgamation and reprocessing of the bed-material flux from these two upstream links gives rise to the tri-modal distribution within the link shown in Figure 4.10a.

Even though only bed-sediment thickness is shown in Figure 4.10, the difference between the flux in and flux out can be seen from the change in bed-sediment thickness through time, and thus when the flux from one link arrives in the directly downstream link. We generally see that when the bed-sediment thickness in a given link is at a local maximum, the bed-sediment thickness in the directly downstream link is at a local minimum. This shows that when a link begins to evacuate sediment, the downstream link begins to accumulate that sediment (akin to sediment pulse movement described in *Gran and Czuba* [2016]). Although, it is important to remember that the arrival of sediment to any one link is dictated by the supply from two directly upstream links and internal generation. So the structure of the bed-sediment thickness in one link does not necessarily directly translate into the structure of the bed-sediment thickness in a directly downstream link. However throughout many of the links shown in Figure 4.10, we see that the underlying structure of the bed-sediment thickness (e.g., periodicity) is largely translated downstream. This structure becomes altered progressing downstream depending on the relative magnitude of additional sediment supplied to the link (e.g., see Figure 4.10e-g).

Another ubiquitous characteristic of bed-sediment thickness, where in-channel storage is important, is periodicity. We quantified the dominant period T [T], for links with a $dCOV > 0.2$ (see Figure 4.8b), as the maximum power of the Fourier transform of simulated bed-sediment thickness between 200 and 600 years and show this spatially for the "single link, in-channel storage" model and the "network, in-channel storage" model (Figure 4.11a and b, respectively). We see that the dominant period generally decreases downstream (Figure 4.11a) and decreases as the volumetric rate of sediment supply $V_p \lambda_i$ increases (Figure 4.11c). Even though we focus on the dominant period, it is important to note that multiple frequencies can be important. For instance, for the three timeseries shown in Figure 4.10e-g, we have computed their power spectra in Figure 4.11d. The two upstream links have dominant periods of 5 years, but the downstream link has a dominant period of 3 years. The period of 5 years is also present in the downstream link but due to the propagation, alteration, and amalgamation of the sediment inputs from upstream and generated internally, the period of 3 years arises and dominates this multiscale timeseries

of bed-sediment thickness.

4.5 Discussion

We have shown how to obtain analytically the time-averaged bed-sediment thickness for each link of an entire river network for any spatial distribution of inputs, with or without accounting for in-channel storage. Furthermore, in the absence of in-channel storage or where a given link and all upstream links are supply limited, we can compute analytically the time-averaged pdf of bed-sediment thickness, which is directly related to the structure of the inputs. Where in-channel storage occurs or for transport-limited conditions, the temporal variability of bed-sediment thickness is larger than that estimated for the Poisson distribution $\hat{f}\left(h_{s,i,t}\right)$ assuming no in-channel storage.

Wilkinson et al. [2006] were able to correctly predict the presence or absence of bed-material accumulation in 71% of mapped links in their network using a similar approach as described herein for calculating the analytical mean bed-sediment thickness. This provides us with some confidence in our predicted mean bed-sediment thicknesses even though we do not provide a validation of our estimates. One reason we do not field verify these model results is that any measurements of bed-sediment thickness will represent the value at an instant in time and not a true average over at least tens of years as would be consistent with our model. In the field, the "instantaneous" bed-sediment thickness would need to be averaged over a reach and the lower boundary (coarse lag deposits or bedrock) would need to be easily identified. The bed-sediment thickness as defined in the model was somewhat arbitrarily set as the depth above an initial profile that is not necessarily at the level of a coarse lag or bedrock. More importantly, we recognize that channels may adjust transport capacity in more ways than we have represented in the model, specifically as adjustments in channel planform, geometry, and roughness. This makes the comparison difficult and explains why *Wilkinson et al.* [2006] compared their results to a simple mapping of the percentage of the bed covered by bed material. The model results are useful, nevertheless as indicators of locations in the

channel network where channel adjustment (via slope or otherwise) is needed, possibly on a temporally varying basis, to transport the amount and type of sediment supplied by the available flow.

Herein we see the emergence of heavy tails in the pdf and periodicity in the timeseries of bed-sediment thickness that arises due to in-channel sediment storage and associated transport-time delay. Heavy-tailed distributions of bed-sediment thickness have been also simulated in other network-based, bed-material transport models with an in-channel storage component [*Benda and Dunne*, 1997a]. Whenever a reach approaches at-capacity transport, then the in-channel storage dynamic becomes activated. It is for these reaches where we see the largest fluctuations in bed-sediment thickness compared to that estimated from the Poisson distribution $\hat{f}\left(h_{s,i,t}\right)$ assuming no in-channel storage (Figure 4.8c) and the magnitude depends on the strength of the feedback between the volume of sediment placed in storage and the resulting slope (Figure 4.8d). Furthermore, the timeseries of bed-sediment thickness for these reaches is periodic, with the dominant period decreasing downstream and with increasing volumetric supply rate of sediment. The volumetric supply rate essentially sets how long it takes to build up a given amount of sediment and thus how long it takes to adjust the slope to a given level before evacuating the storage layer. The heavy tails in the pdf and periodicity in the timeseries of bed-sediment thickness is the result of dynamics on a network in propagating, altering, and amalgamating sediment inputs in sometimes unexpected ways.

By fixing the initial bed elevation and not allowing supply-limited conditions to incise the bed, we are only able to capture the emergent heavy tails in the pdf and periodicity in the timeseries of bed-sediment thickness in reaches that tend to accumulate sediment and for those downstream of these locations (see locations where $RC_i^{final} = 1$ in Figure 4.6c and compare with generators in Figure 4.8e and with periodicity in Figure 4.11b). The slope of reaches where $RC_i^{final} < 1$ (see Figure 4.6c) are steeper than required to pass the supply. These reaches would compensate by incising into their bed, lowering their slopes, and eventually attaining a slope sufficient to just pass the supply. Once this would occur, then these reaches would also be near capacity, initiate in-channel

storage dynamics, and exhibit the emergent heavy tails in the pdf and periodicities in the timeseries of bed-sediment thickness characteristic of this model formulation. To see heavy tails in the pdf and periodicities in the timeseries of simulated bed-sediment thickness for all reaches of a network would indicate that the river network is in dynamic equilibrium. Clearly the Greater Blue Earth River Basin is still adjusting from Holocene glaciation.

Herein, we have tried to understand some of the factors contributing to this emergent behavior through a connection to the underlying mechanisms specified in the model. It remains to be seen if the emergent behavior that arises from the model formulation (e.g., heavy tails, periodicity) is physically realistic. Keep in mind that the continuous long-term probabilistic-average transport of sediment as incorporated in the model is averaged over the intermittent short periods with intense transport and long periods with low transport. Thus, the simulated bed-sediment thicknesses, even "instantaneous" values from the model, inherently represent an average value. Additionally, sediment was supplied to the network randomly (each input delivered at a time independent from any others) with a characteristic interarrival time of one year, which likely contributed to the regularity of the multi-year periodicity. In reality, large amounts of sediment can be supplied across a region over a short duration due to heavy rainfall and high streamflows (violating the assumption of independent inputs) such that large magnitude inputs recur at a timescale much longer than one year (and capturing the large-magnitude, low-frequency events may be an important supplier/driver of realistic bed-material dynamics). The present model averages over these seemingly important factors of interannual variability that would likely give rise to a multi-scale response in bed-sediment thickness (including periodicity) as pulses of sediment of various sizes transport and disperse throughout the network.

Even with confidence in the inputs and in the reach-scale transport dynamics, given the long timescales and large spatial scales of the model, it is very difficult to objectively test the emergent behavior. One avenue for comparison is through residence-time distributions of sediment in a reach from simulations versus observations. Residence-time distributions are another emergent property that provide a common linkage from reach-

scale dynamics to watershed-scale behavior, and have received much attention in recent literature [e.g., *Rinaldo et al.*, 2015]. While not shown here, the residence-time distribution of bed-material sediment in a link ranges from the travel time of sediment in a link $t_{s,i,t}$ to roughly the dominant period T in a link (as this sets the timescale when most sediment capable of being evacuated, would be evacuated from the in-channel storage reservoir). Perhaps in time, a detailed quantification of residence-time distributions from the field and numerical simulations that are then related to hydro-geomorphic properties will allow for suitable validation and ultimately lead to better parameterizations of reach-scale dynamics for incorporating into this modeling framework. For now we have focused on describing how this particular model formulation gives rise to the simulated behavior and also on isolating the role of the channel network on bed-material dynamics. Different storage formulations may give rise to different emergent behavior, and as the use of network-based models become more widespread, it will be important to understand the connection between the specific formulation (including specification of inputs and mechanics of storage) and simulated behavior.

4.6 Concluding Remarks

We have presented a network-based, bed-material sediment model that combines spatially-explicit sediment sourcing with in-channel transport and storage dynamics on a river network. We have shown how to obtain analytically the time-averaged bed-sediment thickness for each link of an entire river network for any spatial distribution of inputs, with or without accounting for in-channel storage. In the absence of in-channel storage or where a given link and all upstream links are supply limited, we have shown how to compute analytically the time-averaged pdf of bed-sediment thickness, which is directly related to the structure of the inputs. Where in-channel storage occurs or for transport-limited conditions, the temporal variability of bed-sediment thickness is larger than that estimated for a Poisson distribution assuming no in-channel storage. Large

fluctuations in bed-sediment thickness arise from reaches transporting at capacity and the magnitude depends on the strength of the feedback between the volume of sediment placed in storage and the resulting slope. Additionally, the timeseries of bed-sediment thickness of these reaches is periodic, with the dominant period decreasing downstream and with increasing volumetric supply rate of sediment. The volumetric supply rate essentially sets how long it takes to build up a given amount of sediment and thus how long it takes to adjust the slope to a given level before evacuating the storage layer. The heavy tails in the pdf and periodicity in the timeseries of bed-sediment thickness is the result of dynamics on a network in propagating, altering, and amalgamating sediment inputs in sometimes unexpected ways.

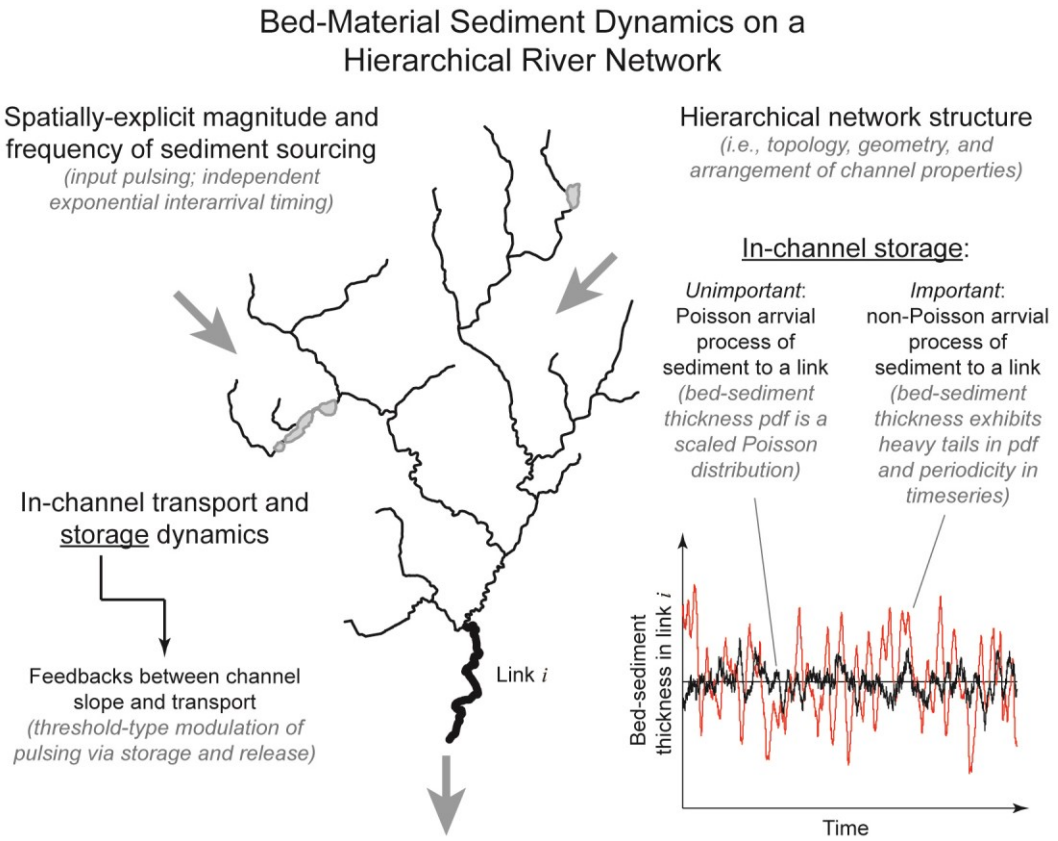

Figure 4.1. Conceptual overview of bed-material sediment dynamics on a hierarchical river network. The combination of spatially-explicit magnitude and frequency of sediment sourcing, hierarchal network structure, and in-channel transport and storage dynamics creates a temporal variability in bed-sediment thickness. When in-channel storage is unimportant, the probability distribution function (pdf) of bed-sediment thickness is a scaled Poisson distribution, which is directly related to the structure of the inputs. When in-channel storage is important, we see the emergence of heavy tails in the pdf and periodicity in the timeseries of bed-sediment thickness.

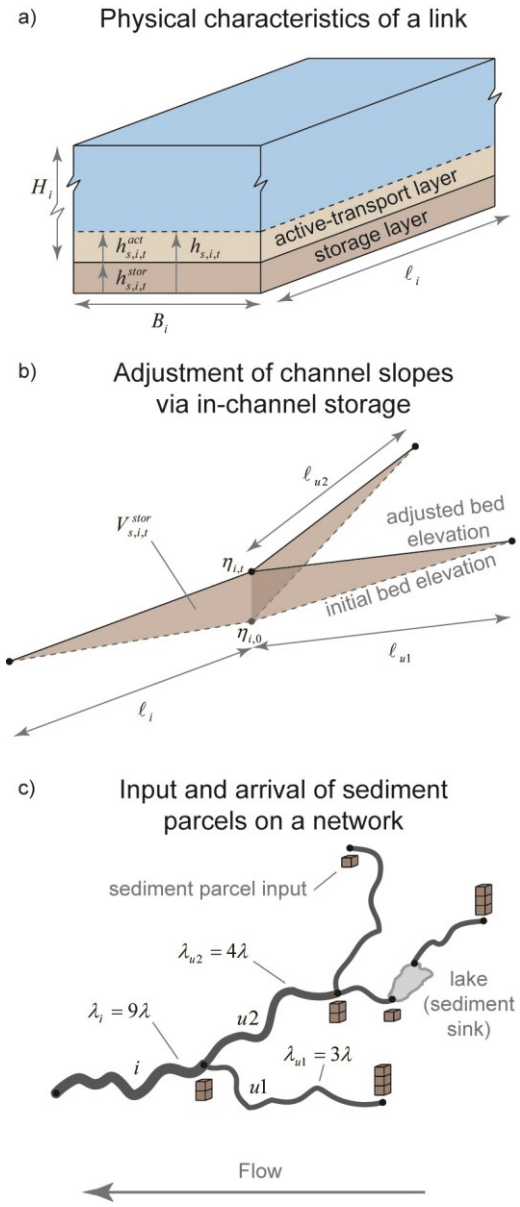

Figure 4.2. Schematic of model elements at various scales. (a) Link scale depicting the active-transport and storage layer. (b) Multi-link storage scale depicting how a volume of sediment $V^{stor}_{s,i,t}$ at time t is placed in its immediate link and directly upstream links to adjust bed elevation and thus slopes. (c) River-network scale depicting how the arrival rate of sediment parcels changes progressing downstream. Each cube represents an individual parcel with rate λ input to the upstream end of a link. Lakes act as sediment sinks removing any sediment arriving from upstream from the system. See text for definition of symbols.

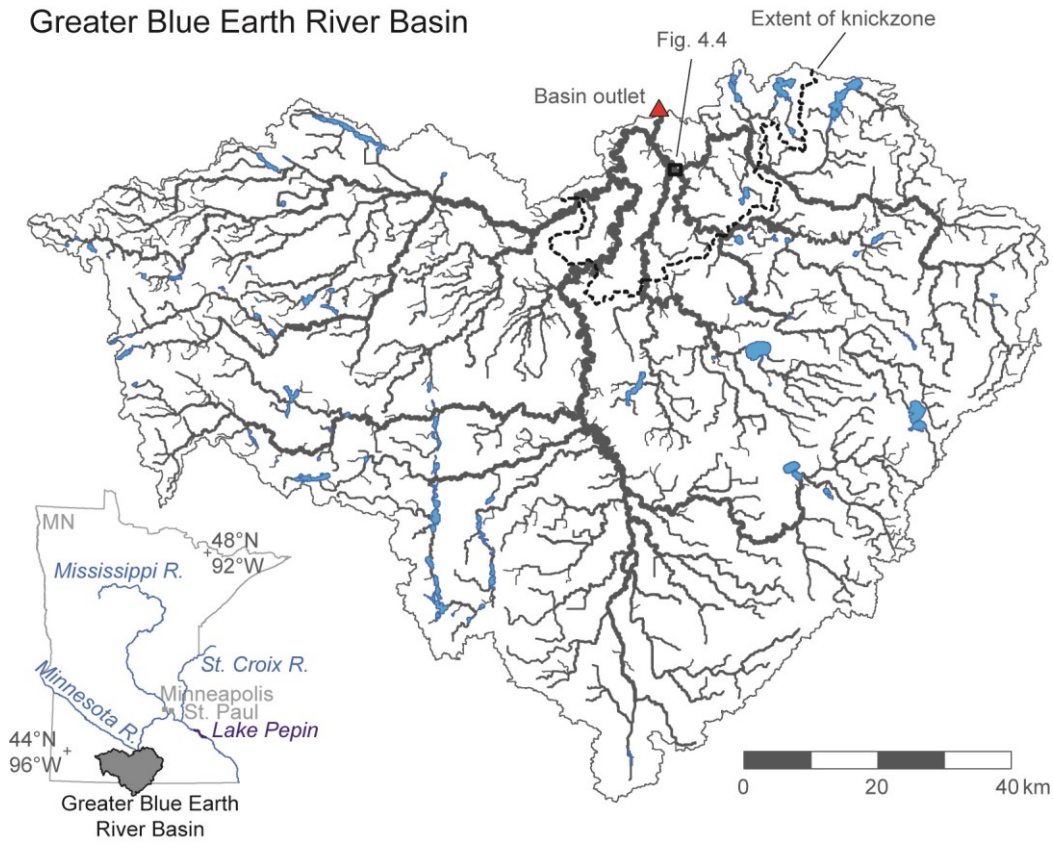

Figure 4.3. Study area map of the Greater Blue Earth River Basin. A detailed basin map shows the channel network (thicker lines correspond to reaches with larger upstream drainage areas), lakes incorporated into the model (shapes), and the approximate extent of the knickzone (dashed line). Location and extent of Figure 4.4 is shown by a small black box. Inset shows a location map of the Greater Blue Earth River Basin relative to the State of Minnesota.

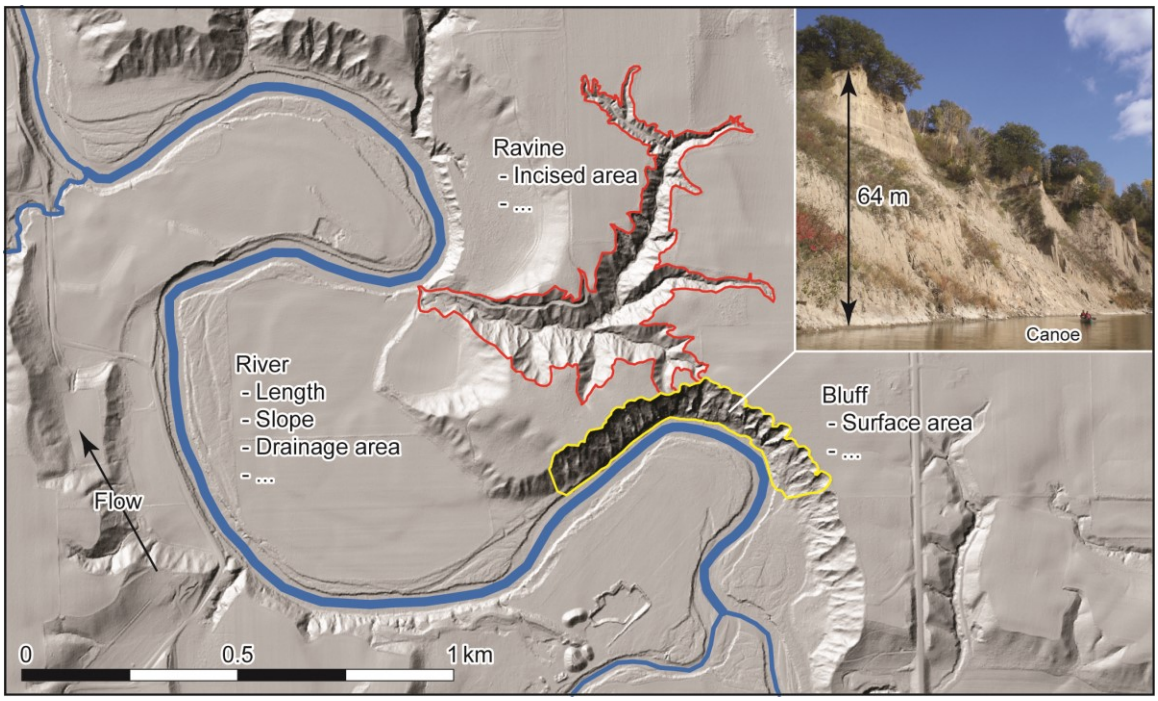

Figure 4.4. Lidar hillshade highlighting major features (river, bluff, and ravine, each with relevant attributes) incorporated into the model. Inset image shows a 64 m bluff; note the canoe for scale. Location and extent is shown in Figure 4.3 by a small black box.

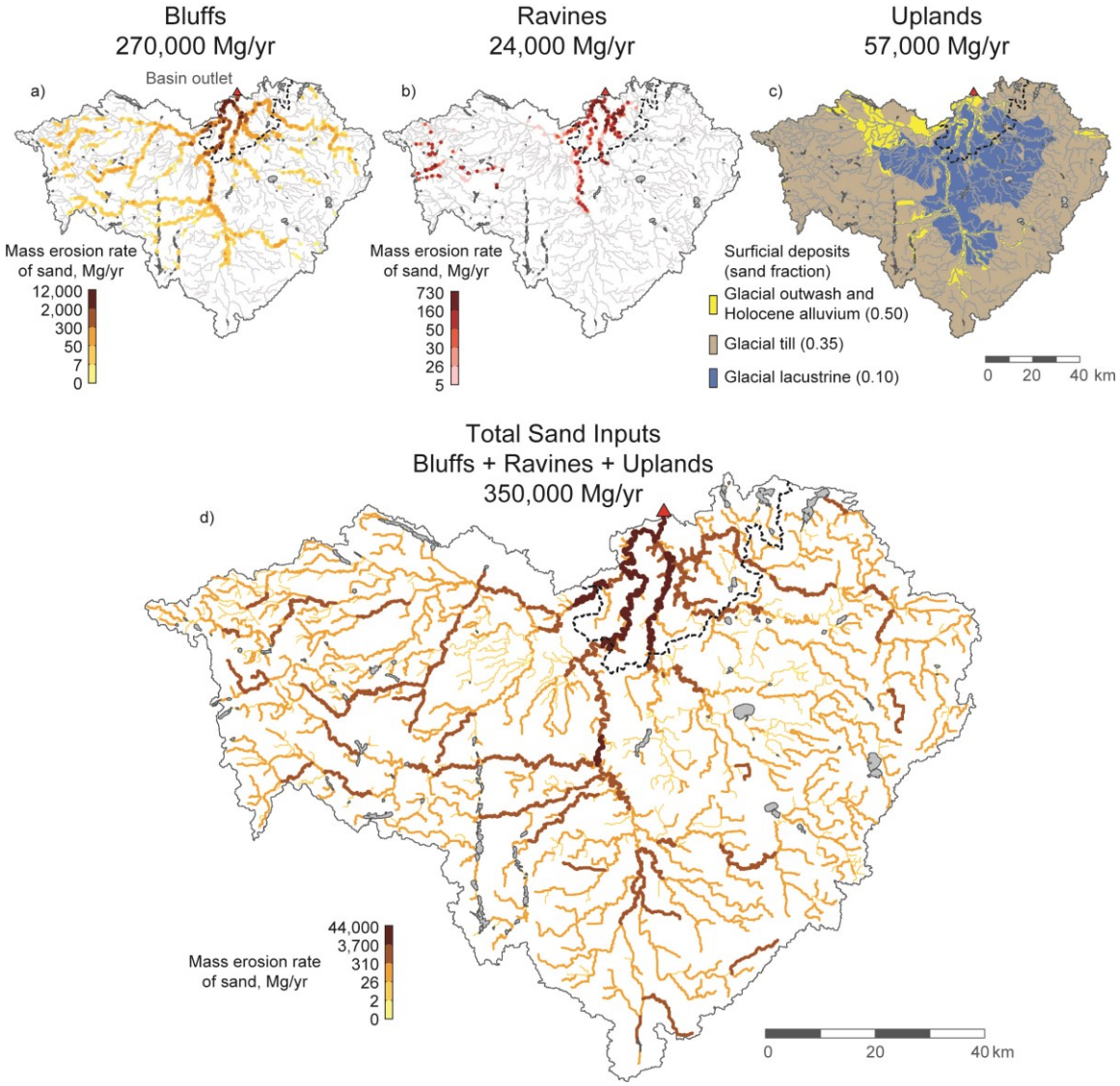

Figure 4.5. Spatially variable, temporally Poisson process of sediment pulsing. (a) Bluff locations colored by mass erosion rate of sand from each bluff. (b) Ravine locations colored by mass erosion rate of sand from each ravine. (c) Uplands with surficial deposits and sand fraction. (d) Total sand input delivered to each link of the network from bluffs, ravines, and uplands. The approximate extent of the knickzone is shown as a dashed line.

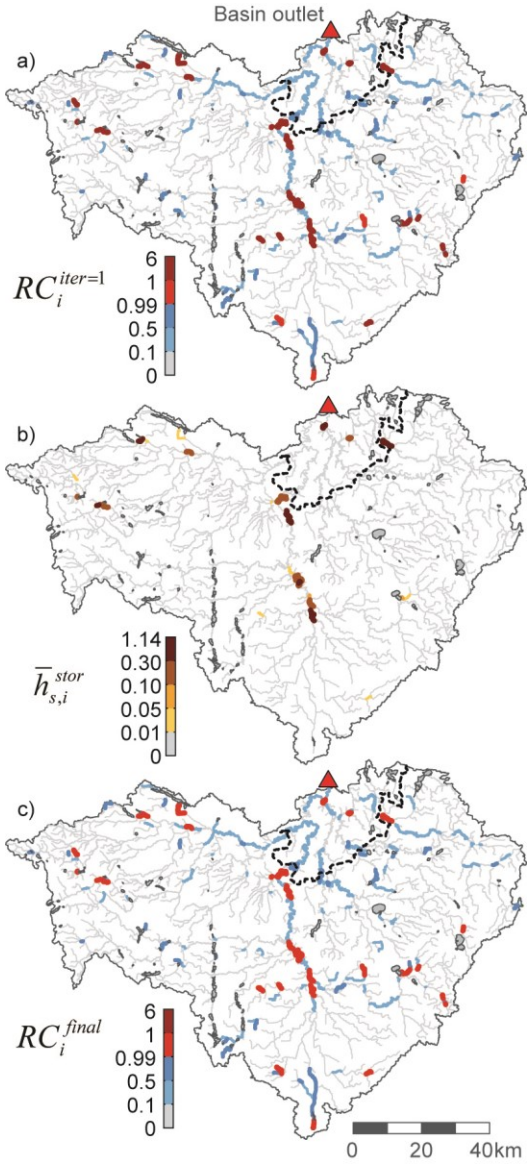

Figure 4.6. Bed elevations adjust such that transport capacity balances sand supply. (a) Initial ratio of sand supply relative to transport capacity $RC_i^{iter=1}$; a value of one indicates capacity balances supply. (b) Increase in bed elevations required for transport capacity to convey the sand supply $\overline{h}_{s,i}^{stor}$; note that these locations are where the values in (a) are greater than one. (c) Final ratio of sand supply relative to transport capacity after the bed has adjusted RC_i^{final}; note any values in (a) that were greater than one become equal to one. The approximate extent of the knickzone is shown as a dashed line. See text for definition of symbols.

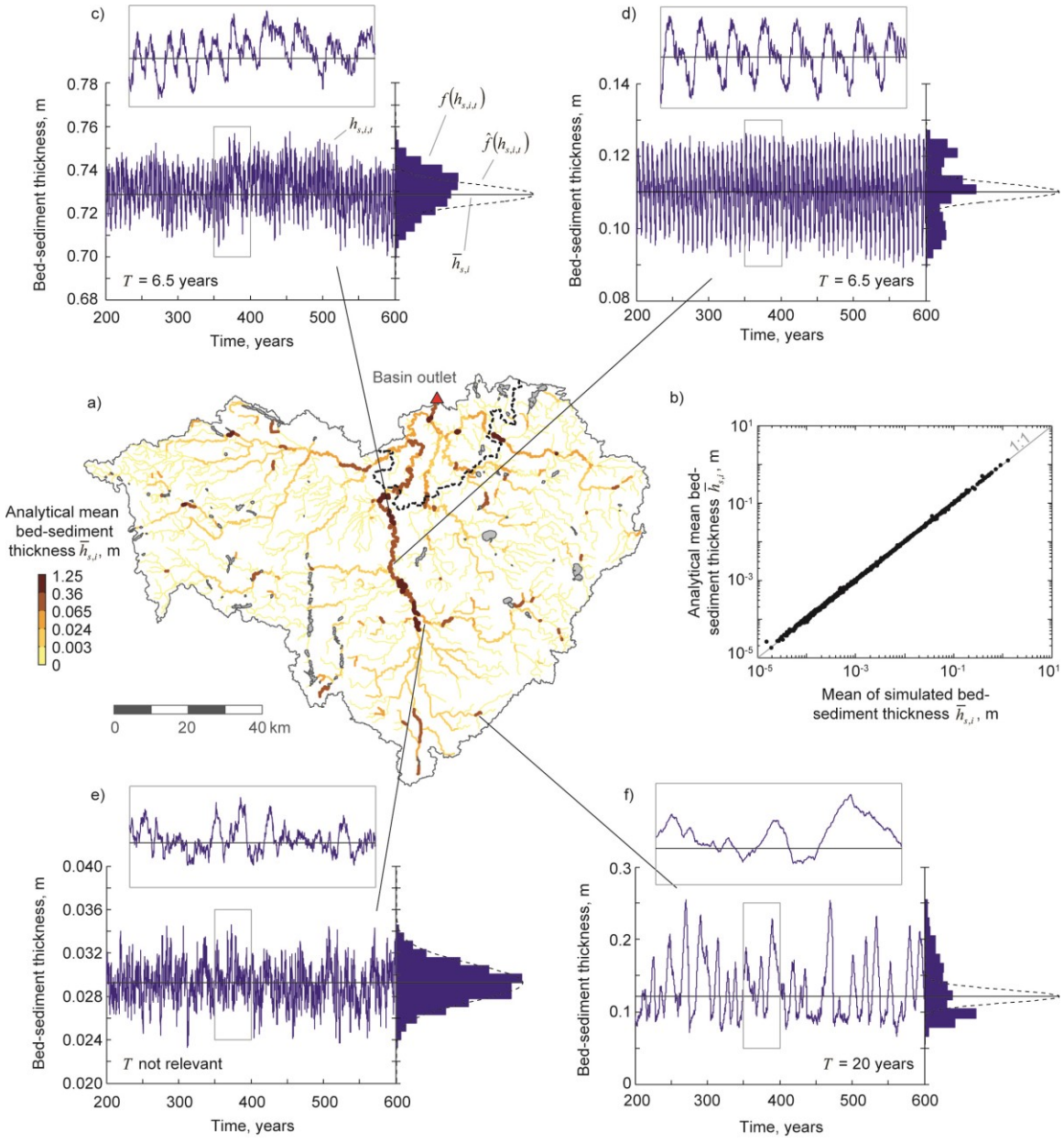

Figure 4.7. Simulated and analytical bed-sediment thickness with in-channel storage. (a) Analytical mean bed-sediment thickness $\bar{h}_{s,i}$. The color breaks are at the 0.99, 0.95, 0.90, and 0.75 quantiles. The approximate extent of the knickzone is shown as a dashed line. (b) Simulated mean bed-sediment thickness averaged from 200 to 600 years versus the analytical mean bed-sediment thickness $\bar{h}_{s,i}$. (c-f) Simulated bed-sediment thickness $h_{s,i,t}$ with probability distribution function (pdf) $f(h_{s,i,t})$ (caption continued on next page)

(caption for Figure 4.7 continued) shown at right (shaded). The solid horizontal line denotes the analytical mean bed-sediment thickness $\bar{h}_{s,i}$. The estimated pdf $\hat{f}\left(h_{s,i,t}\right)$ that assumes the in-channel storage process preserves the structure of a Poisson arrival process is shown at right (dashed line). Inset box zooms in on the simulated bed-sediment thickness timeseries between 350 and 400 years. The dominant period T of the bed-sediment thickness timeseries is also indicated. See text for definition of symbols.

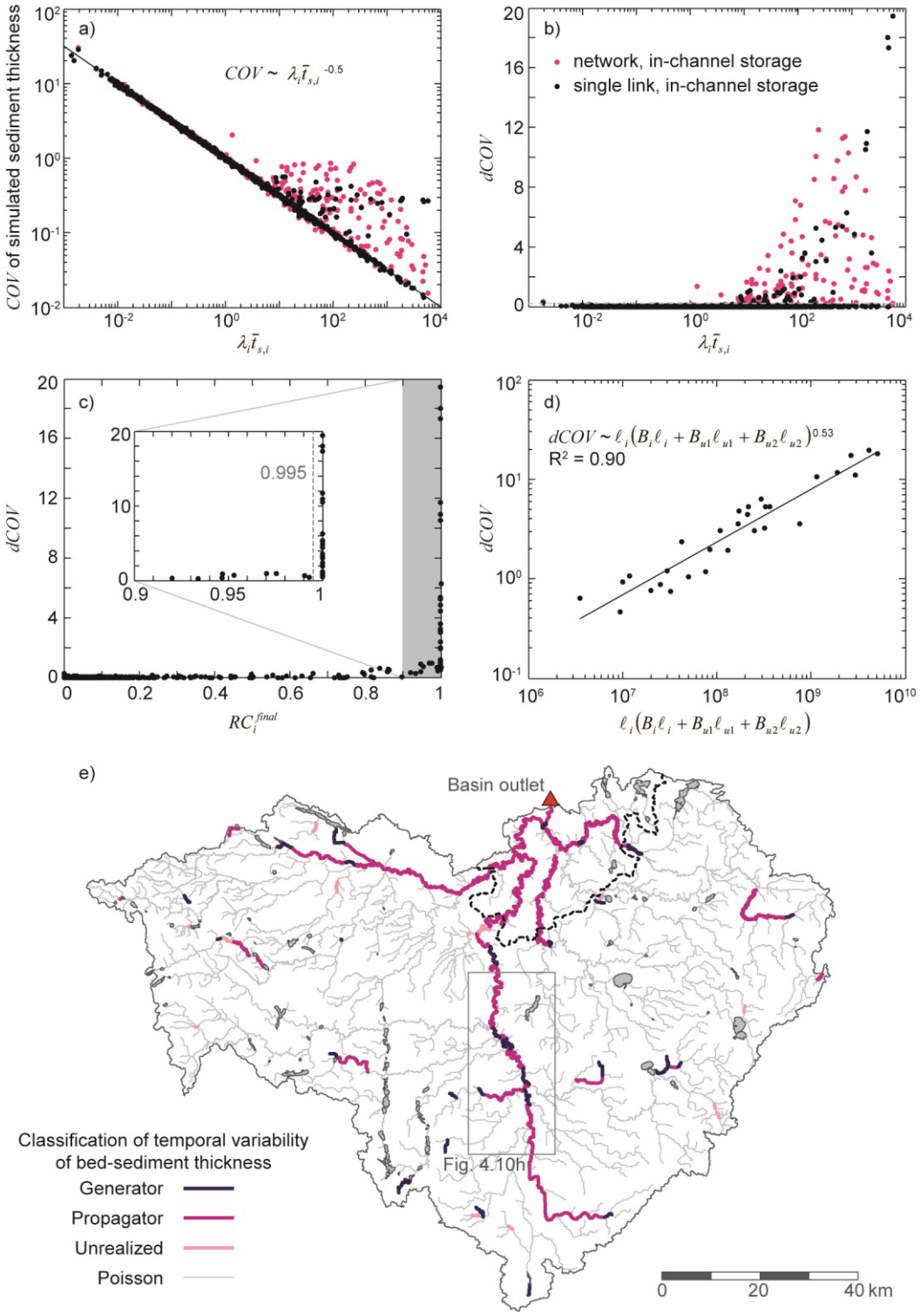

Figure 4.8. Controls on the temporal variability of simulated bed-sediment thickness; insights from the "single link, in-channel storage" (caption continued on next page)

(caption for Figure 4.8 continued) model and the "network, in-channel storage" model. (a) The coefficient of variation (*COV*) of simulated bed-sediment thickness versus $\lambda_i \bar{t}_{s,i}$. (b) The deviation *dCOV* in (a) from the power-law decay. The dashed line at a value of 0.2 is marked as a threshold for classifying links in (e). (c) *dCOV* versus relative capacity RC_i^{final}. Note that most of the deviation, i.e., the large temporal variability of bed-sediment thickness greater than estimated from the Poisson distribution $\hat{f}\left(h_{s,i,t}\right)$, occurs for links at capacity ($RC_i^{final} = 1$). (d) *dCOV* versus the term that determines the strength of the feedback between the volume of sediment in storage and the resulting slope $\ell_i\left(B_i\ell_i + B_{u1}\ell_{u1} + B_{u2}\ell_{u2}\right)$. Only those values from the "single link, in-channel storage" model where $RC_i^{final} > 0.995$ are shown. (e) Classification of temporal variability of bed-sediment thickness as either: *Generator* – links for which both models showed variability greater than Poisson; *Propagator* – links for which the network model showed variability greater than Poisson but not so for the single-link model; *Unrealized* – links for which the single-link model showed variability greater than Poisson but not so for the network model; or *Poisson* – links for which both models showed Poisson variability. Location and extent of Figure 4.10h is shown by a box. See text for definition of symbols.

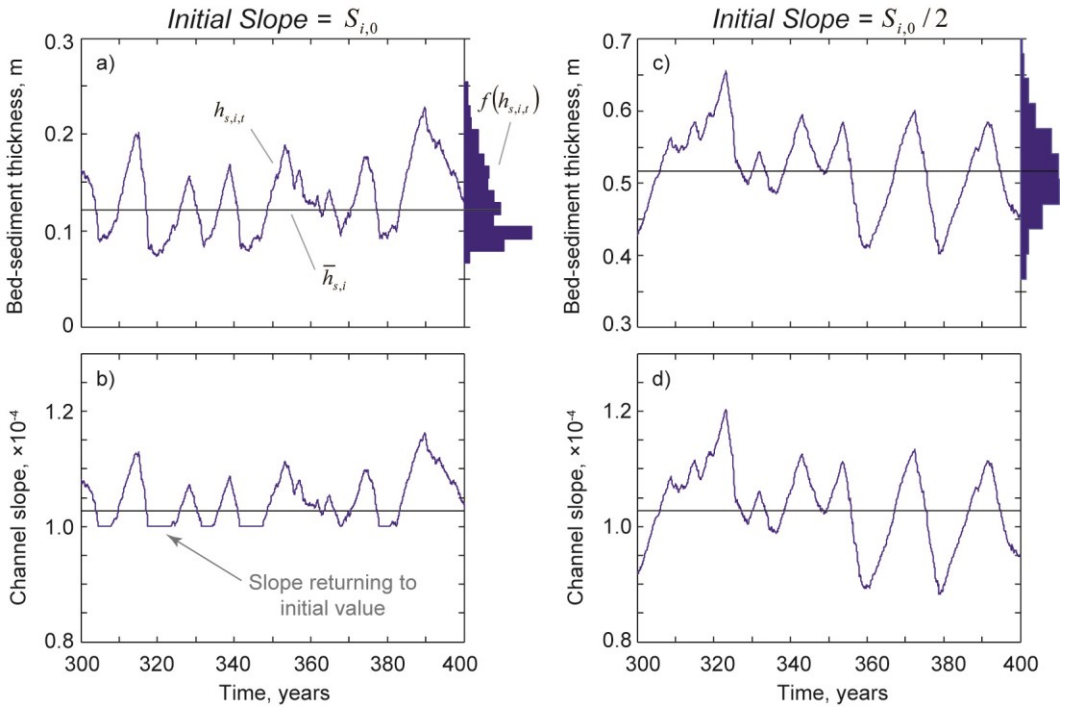

Figure 4.9. Links where bed elevation returns to its initial value have an asymmetric bed-sediment thickness about the mean. The (a) bed-sediment thickness and (b) channel slope under the same conditions as shown in Figure 4.7f; note the asymmetric distribution about the mean. The extent of the timeseries is shown from 300 to 400 years but the probability distribution function $f(h_{s,i,t})$ of the bed-sediment thickness (shown at right) is computed from 200 to 600 years. The (c) bed-sediment thickness and (d) channel slope for the same link but where the initial slope was divided by two, which allows sufficient bed-sediment thickness to build up so fluctuations in bed elevation never return to the initial value; note the symmetric distribution about the mean.

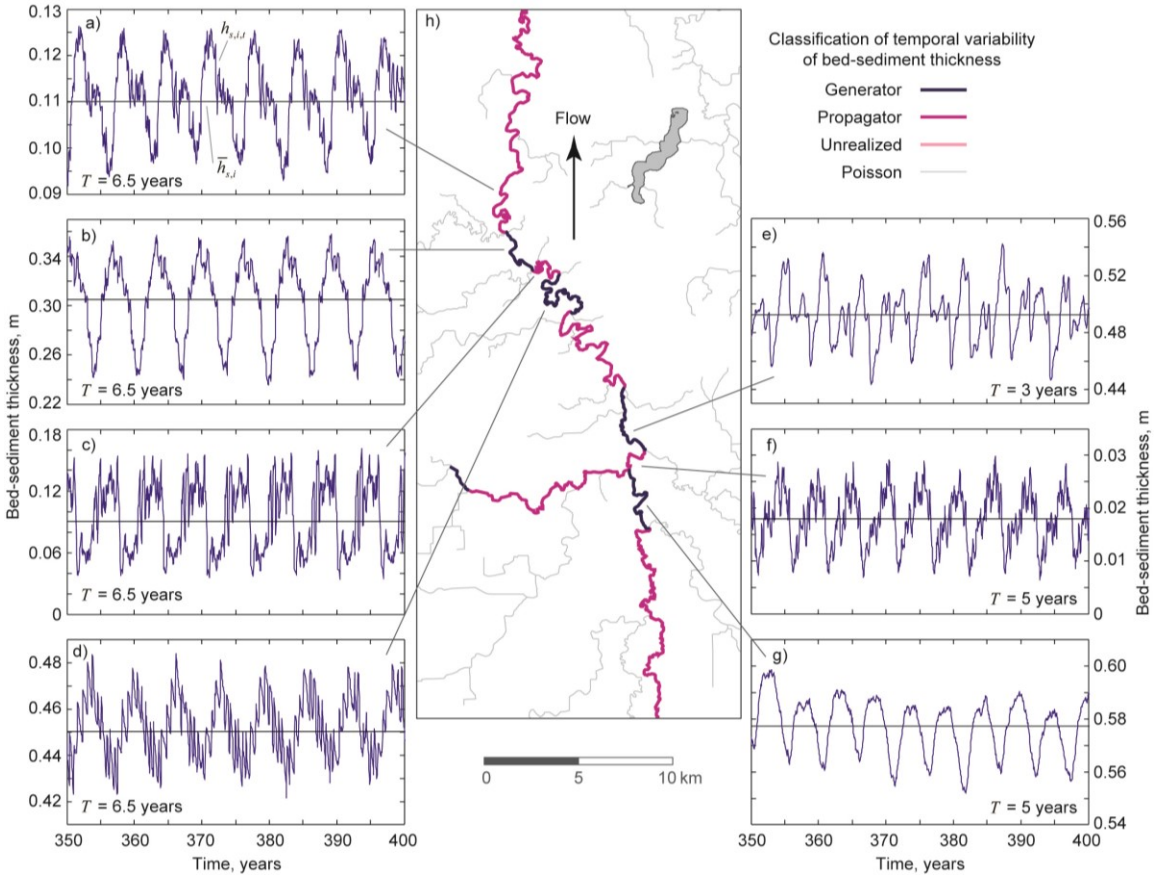

Figure 4.10. Network alteration and propagation of the structure of bed-sediment thickness. (a-d, e-g) Timeseries of bed-sediment thickness from 350 to 400 years. The location of each timeseries is indicated in (h). The tri-modal distribution shown in Figure 4.7d is shown here in (a). The dominant period T of the bed-sediment thickness timeseries is also indicated. See details on the link classification for (h) in the text or in the caption of Figure 4.8.

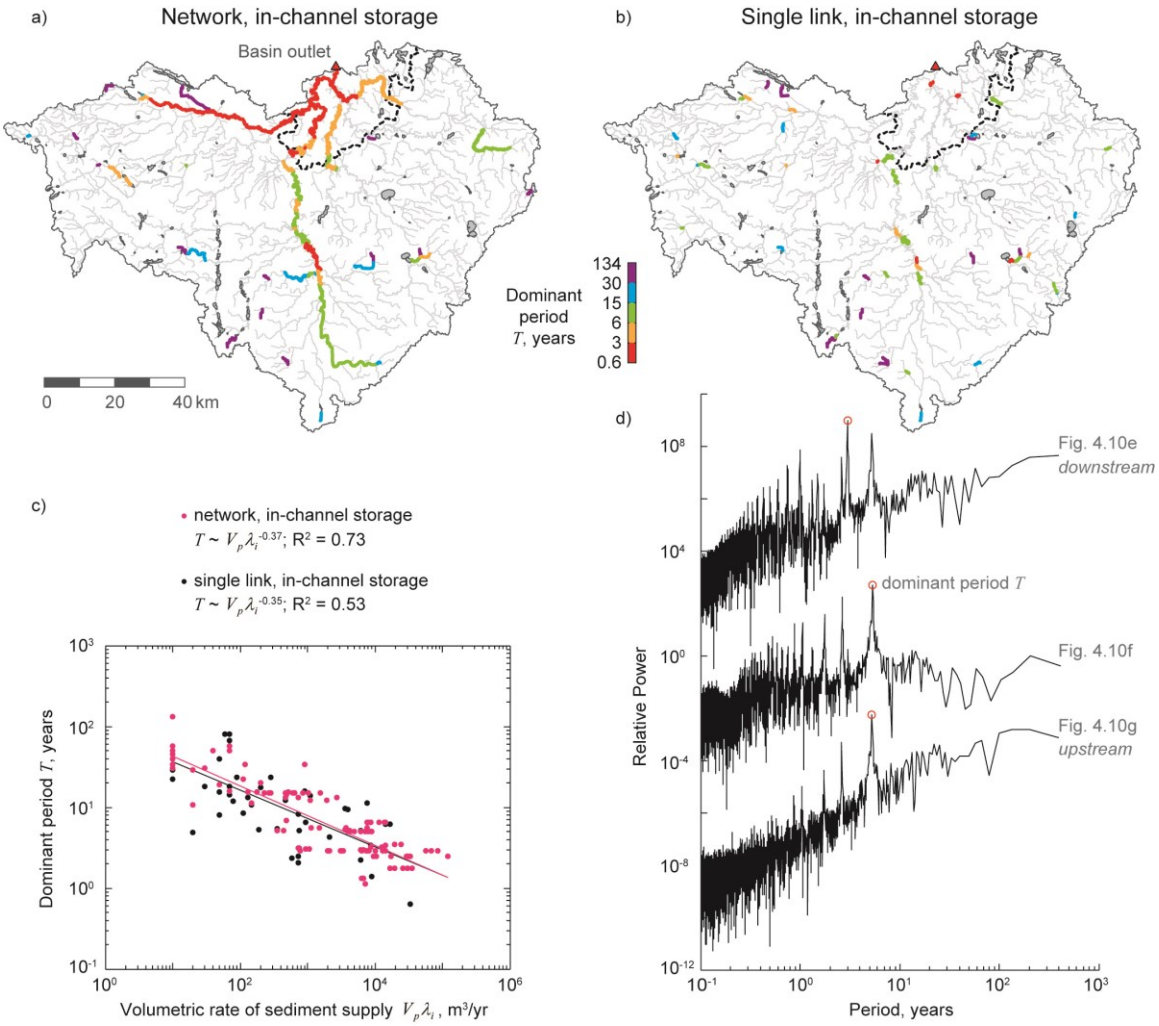

Figure 4.11. Periodicity of simulated bed-sediment thickness. Spatial distribution of the dominant period T of simulated bed-sediment thickness from the "network, in-channel storage" model (a) and the "single link, in-channel storage" model (b). Only links with a $dCOV > 0.2$ (see Figure 4.8b) are shown. (c) The dominant period T decreases for increasing volumetric rate of sediment supply $V_p \lambda_i$. (d) The dominant period T was defined as the maximum power of the Fourier transform of simulated bed-sediment thickness between 200 and 600 years (shown for the timeseries in Figure 4.10e-g), although multiple frequencies can be important. Power spectra are vertically offset.

Chapter 5

Concluding Remarks and Future Perspectives

Increasing pressure to meet the food, water, and energy demands of our growing society in a changing climate has strained the physical, chemical, and biological functioning of watersheds to maintain ecosystem services, such as providing clean water, and to sustain a productive and diverse ecosystem. Now more than ever, watershed managers could use a simple first-order approach for integrating physical, chemical, and biological processes within a watershed for guiding watershed-management decisions. Herein, we have presented a framework for doing just that – environmental inputs traced via a Lagrangian perspective on a river network according to process-based time delays associated with transport, storage, and transformation. Much of the information necessary for a first-order application can be obtained through remotely sensed data; field data provide further refinements and ground-truthing. Applied to the dynamics of bed-material sediment on river networks, this research has produced the following main results:

1. We presented a connectivity-based conceptual framework of environmental response, focusing on the sedimentological response for mud, sand, and gravel. The proposed framework relied on performing a non-linear process-based scaling of the network geometry (link lengths) to convert the network width function into a time response function or process-scaled width function (PSWF) where the process of interest is sediment transport. The process-scaled width function for sediment is the geomorphologic instantaneous unit sedimentograph (GIUS) or the sedimentological

response of a basin to an instantaneous unit volume of sediment uniformly entering all links of the network.

2. We showed that the network topology and sediment transport dynamics in the Minnesota River Basin combine to produce a double peaked response function for sand, suggesting that there exists a resonant frequency of sediment supply that could lead to an unexpected downstream amplification of sedimentological response. The two peaks of the sand response function were attributed to specific areas of the basin, highlighting that the disturbance of one region followed by the disturbance of another region after a certain period of time, may result in an amplification of the effects of the sediment inputs that is otherwise difficult to predict with mechanistic short-time horizon models. The synchronization and amplification of sediment delivery in specific places of a basin may result in greater than expected aggradation of the riverbed triggering disruption in ecosystem functioning, and leading to increased flood risk and increased cost associated with remediation. Therefore, the proposed framework has identified an important vulnerability of the Minnesota River Basin to spatial and temporal structuring of sediment delivery, and can aid in understanding how climatic trends and current and future management decisions may be unexpectedly superimposed on this landscape as it undergoes intensive human management while it is still adjusting to past geologic disturbances.

3. We put forward the hypothesis that places in the network predisposed (due to process dynamics and network topology) to accumulate excess sediment over a considerable river reach and over a considerable period of time reflect locations where a local imbalance in sediment flux may occur thereby highlighting a susceptibility to potential fluvial geomorphic change. We developed a dynamic connectivity framework which uses the river network structure and a simplified Lagrangian transport model to trace fluxes through the network and integrate emergent "clusters," i.e., places of excess flux accumulation, through a cluster persistence index (CPI).

4. We showed that areas with high values of CPI correspond to areas where sediment has a tendency to persist on the network, which may be related to sediment-driven fluvial geomorphic change. Of the three hotspots of fluvial geomorphic change

(defined as locations where observed rates of channel migration were high) in the Greater Blue Earth River Basin, two of these hotspots coincided with high CPI. The third hotspot was not identified by high CPI, but instead was believed to be a hotspot of streamflow-driven change based on additional information and the fact that high bed shear stress coincided with this hotspot. Nonetheless, the dynamic connectivity framework provided a network perspective of dynamical processes that occur at smaller scales, useful for understanding how reach-scale changes cascade into network-scale effects and for informing management actions.

5. We developed a network-based model for bed-material sediment that combines spatially-explicit sediment sourcing with in-channel transport and storage dynamics on a river network. We have shown how to compute analytically the time-averaged bed-sediment thickness for each link of an entire river network for any spatial distribution of inputs, with or without accounting for in-channel storage.

6. Under supply-limited conditions, we have shown how to analytically derive the time-averaged probability distribution function of bed-sediment thickness, which is directly related to the structure of the inputs.

7. Under transport-limited conditions, (1) the time-averaged probability distribution function of bed-sediment thickness is heavy tailed where the magnitude of fluctuations depends on the strength of feedback between the volume of sediment placed in storage and the resulting slope and (2) the timeseries of bed-sediment thickness is periodic with dominant period inversely proportional to the volumetric flux, which sets the timescale for the bed to adjust. The timeseries of bed-sediment thickness is the result of dynamics on a network in propagating, altering, and amalgamating sediment inputs in sometimes unexpected ways.

By embedding bed-material sediment dynamics on a river network, we have shown that it is possible to gain a better understanding of the emergent behavior of a watershed, which would be otherwise difficult to predict. This leads to the challenge of verifying whether the identified emergent behavior actually exists, even with confidence in the inputs, network connectivity, and reach-scale dynamics. One avenue for comparison is through residence-time distributions of water/sediment/nutrients in a reach from

simulations versus observations. Residence-time distributions are another emergent property that provide a common linkage from reach-scale dynamics to watershed-scale behavior, and have received much attention in recent literature [e.g., *Rinaldo et al*., 2015]. Perhaps in time, a detailed quantification of residence-time distributions from the field and numerical simulations that are then related to hydro-geomorphic properties will allow for suitable validation and ultimately lead to better parameterizations of reach-scale dynamics for incorporating into this framework. Some future research directions include:

1. While we have focused on analytical insights and describing the functioning and emergent behavior of the network-based, bed-material sediment model, this model is capable of addressing more pressing questions including: (1) How does the heterogeneity of landscape features affect the spatial distribution of sediment impacts, e.g., confined to select reaches near the sources? (2) What are the timescales of movement of sediment through the system, including storage, that can better inform legacy effects and hysteresis? (3) Where to target management actions that will most effectively reduce the detrimental impacts of sediment?

2. One major limitation of the present network-based, bed-material sediment model is not accounting for channel/floodplain interactions that are important for accurately quantifying how sediment moves through a watershed. Thus, a logical next step is to implement a mechanism for sediment storage and release from floodplains. Developing a probabilistic approach to floodplain exchange is fairly straightforward given the channel migration rate and the sediment load for a given reach [e.g., *Malmon et al.*, 2003; *Lauer and Willenbring*, 2010; *Viparelli et al*., 2013; *Lauer et al*., 2016]. The residence time of sediment in the floodplain is a key constraint for simulating channel/floodplain exchange. An understanding of floodplain residence time is beginning to emerge from an analysis of river-migration models [*Bradley and Tucker*, 2013] and from work that first measures the relevant fluxes and exchanges, and then develops the mathematical foundations around these measurements to understand sediment delivery timescales [*Pizzuto*, 2012; *Pizzuto et al.*, 2014]. But the component that is needed for network-scale models is a generalized understanding of the controls on floodplain residence time from floodplain, channel, sedimentologic, and hydrologic characteristics. One specific research question to

consider is to what extent does sediment storage and release from floodplains affect the delivery of sediment at the watershed scale?

3. Many agricultural landscapes of the Midwest, including the Minnesota River Basin, were once dominated by tall-grass prairie and dotted with poorly drained wetlands [*Marschner*, 1974]. Beginning in the late 1800s, these wetlands were drained for agriculture with the construction of surface ditches and installation of subsurface drain tiles [*Dahl and Allord*, 1996]. Only remnants of these wetlands remain today [*Musser et al.*, 2009]. However, where they do exist, they are important sources, sinks, and transformers of important macronutrients of carbon, nitrogen, and phosphorous. Specifically, unpublished data of Amy Hansen and Jacques Finlay (University of Minnesota) show that wetlands (at least seasonally) are (1) a carbon source to downstream reaches, (2) decease nitrate possibly through assimilation or denitrification, and (3) are important locations of phosphorous storage and transformation between dissolved and particulate forms. Thus, where these wetlands are located in the landscape has important implications for understanding downstream water quality.

Ongoing work is to extend the developed framework to nutrient dynamics that potentially includes carbon, nitrogen, and phosphorus cycling. The first step is locating existing wetlands in the 1,800 km^2 Le Sueur Basin (a subbasin of the Greater Blue Earth Basin), assigning attributes to those wetlands that affect water, sediment, and nutrient dynamics such as depth, surface area, vegetation, etc., and establishing their connectivity to the river network. Understanding the movement of water and sediment is an important first step for understanding nutrient dynamics because these nutrients tend to transport in either a dissolved phase with the water or a particulate phase sorbed to sediment (in the case of phosphorous). Then simple rules will need to be developed that inform how to generate, transport, store, and transform each important phase of each nutrient, which can be partly based on field data and also based on existing literature investigating the detailed process dynamics for each of these features (akin to the development of travel time of sediment through a fluvial channel described in chapter 2). Once these features and process dynamics are in place, the idea is to track the movement of different phases of nutrients: at least dissolved and particulate, through the network.

The ultimate goal of this future research is to better understand nutrient dynamics in a wetland/river network complex. Specific research questions to consider include: (1) How does the spatial heterogeneity of wetlands affect the distribution of nutrients throughout the network, i.e., how and where do nutrient hotspots emerge? (2) What are timescales of movement of various nutrients through the system and where are temporary storage zones (floodplains and wetlands) that can better inform legacy effects (particularly in regards to phosphorous)? (3) Where is the best place to target management actions in terms of creating wetlands in order to improve water quality? A potential extension of this work is to understand how changes in the water, sediment, and nutrient regimes cascade to changes in the community of aquatic biota, such as algae, insects, mussels, and fish, all within a network context.

References

Abad, J. D., and M. H. Garcia (2006), RVR Meander: A toolbox for re-meandering of channelized streams, *Computers and Geosciences*, 32, 92-101, doi:10.1016/j.cageo.2005.05.006.

Alexander, K. B., J. K. Böhlke, E. W. Boyer, et al. (2009), Dynamic modeling of nitrogen losses in river networks unravels the coupled effects of hydrological and biogeochemical processes, *Biogeochemistry*, 93, 91-116, doi:10.1007/S10533-008-9274-8.

Angel, J., and F. Huff (1997), Changes in heavy rainfall in Midwestern United States, *J. Water Resour. Plann. Manage.*, 123(4), 246–249, doi:10.1061/(ASCE)0733-9496(1997)123:4(246).

Belmont, P. (2011), Floodplain width adjustments in response to rapid base level fall and knickpoint migration, *Geomorphology*, 128, 92-102, doi:10.1016/j.geomorph.2010.12.026.

Belmont, P., K. B. Gran, S. P. Schottler, P. R. Wilcock, S. S. Day, C. Jennings, J. W. Lauer, E. Viparelli, J. K. Willenbring, D. R. Engstrom, and G. Parker (2011), Large shift in source of fine sediment in the Upper Mississippi River, *Environ. Sci. Technol.*, 45, 8804–8810, doi:10.1021/es2019109.

Benda, L., and T. Dunne (1997a), Stochastic forcing of sediment routing and storage in channel networks, *Water Resour. Res.*, 33(12), 2865–2880, doi:10.1029/97WR02387.

Benda, L., and T. Dunne (1997b), Stochastic forcing of sediment supply to channel networks from landsliding and debris flow, *Water Resour. Res.*, 33(12), 2849–2863, doi:10.1029/97WR02388.

Benda, L., N. L. Poff, D. Miller, T. Dunne, G. Reeves, G. Pess, and M. Pollock (2004a), The network dynamics hypothesis: How channel networks structure riverine habitats, *BioScience*, 54(5), 413-427, doi:10.1641/0006-568(2004)054[0413:TNDHHC]2.0.CO;2.

Benda, L., K. Andras, D. Miller, and P. Bigelow (2004b), Confluence effects in rivers: Interactions of basin scale, network geometry, and disturbance regimes, *Water Resour. Res.*, 40, W05402, doi:10.1029/2003WR002583.

Bertuzzo, E., R. Muneepeerakul, H. J. Lynch, W. F. Fagan, I. Rodriguez-Iturbe, and A. Rinaldo (2009), On the geographic range of freshwater fish in river basins, Water Resour. Res., 45, W11420, doi:10.1029/2009WR007997.

Bertuzzo, E., S. Azaele, A. Maritan, M. Gatto, I. Rodriguez-Iturbe, and A. Rinaldo (2008), On the space-time evolution of a cholera epidemic, Water Resour. Res., 44, W01424, doi:10.1029/2007WR006211.

Bevis, M. (2015), Sediment budgets indicate Pleistocene base level fall drives erosion in Minnesota's greater Blue Earth River basin, M.S. Thesis, University of Minnesota Duluth.

Bhunya, P. K., S. K. Jain, P. K. Singh, and S. K. Mishra (2010), A simple conceptual

model of sediment yield, *Water Resour. Manage.*, 24, 1697–1716, doi:10.1007/s11269-009-9520-4.
Blann, K. L., J. L. Anderson, G. R. Sands, and B. Vondracek (2009), Effects of agricultural drainage on aquatic ecosystems: a review, *Critical Reviews in Environmental Science and Technology*, 39(11), 909-1001, doi:10.1080/10643380801977966.
Botter, G., E. Bertuzzo, and A. Rinaldo (2010), Transport in the hydrologic response: Travel time distributions, soil moisture dynamics, and the old water paradox, *Water Resour. Res.*, 46, W03514, doi:10.1029/2009WR008371.
Botter, G., T. Settin, M. Marani, and A. Rinaldo (2006), A stochastic model of nitrate transport and cycling at basin scale, *Water Resour. Res.*, 42, W04415, doi:10.1029/2005WR004599.
Bracken, L. J., L. Turnbull, J. Wainwright, and P. Bogaart (2015), Sediment connectivity: a framework for understanding sediment transfer at multiple scales, *Earth Surf. Process. Landforms*, doi:10.1002/esp.3635.
Bracken, L. J., J. Wainwright, G. A. Ali, D. Tetzlaff, M. W. Smith, S. M. Reaney, and A. G. Roy (2013), Concepts of hydrological connectivity: Research approaches, pathways and future agendas, *Earth-Science Reviews*, 119, 17-34, doi:10.1016/j.earscirev.2013.02.001.
Bradley, D. N., and G. E. Tucker (2013), The storage time, age, and erosion hazard of laterally accreted sediment on the floodplain of a simulated meandering river, *J. Geophys. Res. Earth Surf.*, 118, 1308–1319, doi:10.1002/jgrf.20083.
Brown, C. B. (1943), Discussion of sedimentation in reservoirs, *Proc. Am. Soc. Civ. Eng.*, 69, 1493–1500.
Campbell Grant, E., W. Lowe, and W. Fagan (2007), Living in the branches: Population dynamics and ecological processes in dendritic networks, *Ecol. Lett.*, 10, 165–175, doi:10.1111/j.1461-0248.2006.01007.x.
Carlisle, D. M., M. R. Meador, T. M. Short, C. M. Tate, M. E. Gurtz, W. L. Bryant, J. A. Falcone, and M. D. Woodside (2013), The quality of our Nation's waters – Ecological health in the Nation's streams, 1993–2005, *U.S. Geological Survey Circular 1391*, 120 p.
Carrara, F., F. Altermatt, I. Rodriguez-Iturbe, and A. Rinaldo (2012), Dendritic connectivity controls biodiversity patterns in experimental metacommunities, Proc. Natl. Acad. Sci. U.S.A., 109(15), 5761–5766, doi:10.1073/pnas.1119651109.
Ceola, S., E. Bertuzzo, G. Singer, T. J. Battin, A. Montanari, and A. Rinaldo (2014), Hydrologic controls on basin-scale distribution of benthic invertebrates, Water Resour. Res., 50, 2903–2920, doi:10.1002/2013WR015112.
Clayton, L., and S. R. Moran (1982), Chronology of late Wisconsinan glaciation in middle North America, *Quat. Sci. Rev.*, 1, 55–82.
Cui, Y., and G. Parker (2005), Numerical model of sediment pulses and sediment-supply disturbances in mountain rivers, *J. Hydraul. Eng.*, 131(8), doi: 10.1061/(ASCE)0733-9429(2005)131:8(646).
Cui, Y., G. Parker, T. E. Lisle, J. Gott, M. E. Hansler-Ball, J. E. Pizzuto, N. E.

Allmendinger, and J. M. Reed (2003a), Sediment pulses in mountain rivers: 1. Experiments, *Water Resour. Res.*, 39(9), 1239, doi: 10.1029/2002WR001803.
Cui, Y., G. Parker, J. Pizzuto, and T. E. Lisle (2003b), Sediment pulses in mountain rivers: 2. Comparison between experiments and numerical predictions, *Water Resour. Res.*, 39(9), 1240, doi: 10.1029/2002WR001805.
Czuba, J. A., and E. Foufoula-Georgiou (2014), A network-based framework for identifying potential synchronizations and amplifications of sediment delivery in river basins, *Water Resources Research*, 50(5), 3826–3851, doi:10.1002/2013WR014227.
Czuba, J. A., and E. Foufoula-Georgiou (2015), Dynamic connectivity in a fluvial network for identifying hotspots of geomorphic change, *Water Resources Research*, 51(3), 1401-1421, doi:10.1002/2014WR016139.
Dadaser-Celik, F., and H. G. Stefan (2009), Stream flow response to climate in Minnesota, project report no. 510, 118 p., St. Anthony Falls Laboratory, University of Minnesota, Minneapolis, Minn.
Dahl, T. E., and G. J. Allord (1996), History of wetlands in the conterminous United States, in National Water Summary on Wetland Resources, *U.S. Geological Survey Water-Supply Paper 2425*, Reston Va. (http://water.usgs.gov/nwsum/WSP2425/history.html) last accessed April 22, 2016.
Day, S. S., K. B. Gran, P. Belmont, and T. Wawrzyniec (2013), Measuring bluff erosion part 2: pairing aerial photographs and terrestrial laser scanning to create a watershed scale sediment budget, *Earth Surf. Process. Landforms*, 38(10), 1068-1082, doi:10.1002/esp.3359.
Dietrich, W. E. (1982), Settling velocity of natural particles, *Water Resour. Res.*, 18(6), 1615–1626, doi:10.1029/WR018i006p01615.
Dooge, J. C. I. (1973), Linear theory of hydrologic systems, Agriculture Research Service Technical Bulletin No. 1468, U.S. Dept. of Agriculture. Reprinted in 2003: EGU Reprint Series, 1, European Geosciences Union, Kattenburg, Lindau, 327 p.
Durrett, R. (2012), *Essentials of Stochastic Processes*, 265 p., Springer, New York, New York.
Dust, D., and E. Wohl (2012), Conceptual model for complex river responses using an expanded Lane's relation, *Geomorphology*, 139-140, 109-121, doi:10.1016/j.geomorph.2011.10.008.
Eke, E., G. Parker, Y. Shimizu (2014), Numerical modeling of erosional and depositional bank processes in migrating river bends with self-formed width: morphodynamics of bar push and bank pull, *Journal of Geophysical Research Earth Surface*, doi:10.1002/2013JF003020.
Engelund, F., and E. Hansen (1967), *A Monograph on Sediment Transport in Alluvial Streams*, 62 p., Tek. Forlag, Copenhagen, Denmark.
Ferguson, R. I., and M. Church (2004), A simple universal equation for grain settling velocity, *J. Sedimentary Res*., 74(6), 933–937, doi: 10.1306/051204740933.
Foufoula-Georgiou, E., Z. Takbiri, J. A. Czuba, and J. Schwenk (2015), The change of nature and the nature of change in agricultural landscapes: Hydrologic regime

shifts modulate ecological transitions, *Water Resources Research*, 51(8), 6649-6671, doi:10.1002/2015WR017637.

Fryirs, K. (2013), (Dis)Connectivity in catchment sediment cascades: a fresh look at the sediment delivery problem, *Earth Surf. Process.*, 38, 30–46, doi:10.1002/esp.3242.

Furey, P. R., and V. K. Gupta (2007), Diagnosing peak-discharge power laws observed in rainfall-runoff events in Goodwin Creek experimental watershed, *Advances in Water Resources*, 30(11), 2387-2399, doi:10.1016/j.advwatres.2007.05.014.

Garcia, M. H. (2008), Sediment transport and morphodynamics, in *Sedimentation engineering: Processes, measurements, modeling, and practice: ASCE manuals and reports on engineering practice*, 110, edited by Garcia, M. H., ASCE, Reston, Virginia, 21–163.

Gassman, P. W., M. R. Reyes, C. H. Green, and J. G. Arnold (2007), The soil and water assessment tool: Historical development, applications, and future research directions, *Trans. Am. Soc. Agric. Biol. Eng.*, 50(4), 1211–1250.

Gracia-Sanchez, J. (1996), Generation of synthetic sedimentgraphs, *Hydrol. Process.*, 10(9), 1181–1191, doi:10.1002/(SICI)1099-1085(199609)10:9<1181::AID-HYP369>3.0.CO;2-X.

Gran, K. B., and J. A. Czuba (2016), Sediment pulse evolution and the role of network structure, *Geomorphology*, doi:10.1016/j.geomorph.2015.12.015.

Gran, K. B., N. Finnegan, A. L. Johnson, P. Belmont, C. Wittkop, and T. Rittenour (2013), Landscape evolution, valley excavation, and terrace development following abrupt postglacial base-level fall, *GSA Bulletin*, 125(11-12), 1851-1864, doi:10.1130/B30772.1.

Gran, K. B., P. Belmont, S. S. Day, C. Jennings, A. Johnson, L. Perg, and P. R. Wilcock (2009), Geomorphic evolution of the Le Sueur River, Minnesota, USA, and implications for current sediment loading, in *Management and Restoration of Fluvial Systems with Broad Historical Changes and Human Impacts*, vol. 451, edited by L. A. James, S. L. Rathburn, and G. R. Whittecar, pp. 119–130, Geol. Soc. of Am., Boulder, Colo., doi:10.1130/2009.2451(08).

Gran, K., P. Belmont, S. Day, C. Jennings, J. W. Lauer, E. Viparelli, P. Wilcock, and G. Parker (2011a), An integrated sediment budget for the Le Sueur River Basin, Minnesota Pollution Control Agency, *Report wq-iw7-29o*, Mankato, MN. 128 p. (http://www.pca.state.mn.us/index.php/view-document.html?gid=16202) last accessed 17 May 2016.

Gran, K. B., P. Belmont, S. S. Day, N. Finnegan, C. Jennings, J. W. Lauer, and P. R. Wilcock (2011b), Landscape evolution in south-central Minnesota and the role of geomorphic history on modern erosional processes, *GSA Today*, 21(9), 7–9, doi:10.1130/G121A.1.

Groisman, P. Y., R. W. Knight, T. R. Karl, D. R. Easterling, B. Sun, and J. H. Lawrimore (2004) Contemporary changes of the hydrological cycle over the contiguous United States: trends derived from in situ observations, *J. Hydrometeor.*, 5(1), 64–85, doi:http://dx.doi.org/10.1175/1525-7541(2004)005<0064:CCOTHC>2.0.CO;2.

Groisman, P. Y., R. W. Knight, and T. R. Karl (2012), Changes in intense precipitation over the central United States, *J. Hydrometeor.*, 13(1), 47–66, doi:http://dx.doi.org/10.1175/JHM-D-11-039.1.

Guo, J., and P. Y. Julien (2004), Efficient algorithm for computing Einstein integrals, *J. Hydraul. Eng.*, 130(12), 1198–1201, doi:10.1061/(ASCE)0733-9429(2004)130:12(1198).

Gupta, V. K., and O. J. Mesa (1988), Runoff generation and hydrologic response via channel network geomorphology – recent progress and open problems, *J. Hydrology*, 102, 3–28, doi:10.1016/0022-1694(88)90089-3.

Gupta, V. K., E. Waymire, and C. T. Wang (1980), A representation of an instantaneous unit hydrograph from geomorphology, *Water Resour. Res.*, 16, 855–862, doi:10.1029/WR016i005p00855.

Gupta, V. K., E. Waymire, and I. Rodriguez-Iturbe (1986), On scales, gravity and network structure in basin runoff, in *Scale Problems in Hydrology*, edited by V. K. Gupta, I. Rodriguez-Iturbe, and E. F. Wood, pp. 159–184, D. Reidel, Dordrecht, Holland.

Gupta, V. K., R. Mantilla, B. M. Troutman, D. Dawdy, and W. F. Krajewski (2010), Generalizing a nonlinear geophysical flood theory to medium-sized river networks, *Geophys. Res. Lett.*, 37, L11402, doi:10.1029/2009GL041540.

Hansen, A. T., J. A. Czuba, J. Schwenk, A. Longjas, M. Danesh-Yazdi, D. J. Hornbach, and E. Foufoula-Georgiou (2016), Coupling freshwater mussel ecology and river dynamics using a simplified dynamic interaction model, *Freshwater Science*, 35(1), 200-215, doi:10.1086/684223.

Harvey, A. M. (2002), Effective timescales of coupling within fluvial systems, *Geomorphology*, 44, 175–201, doi:10.1016/S0169-555X(01)00174-X.

Heckmann, T., W. Schwanghart, and J. D. Phillips (2015), Graph theory – recent developments of its application in geomorphology, *Geomorphology*, doi:10.1016/j.geomorph.2014.12.024.

Hobbs, H. C., and J. E. Goebel (1982), *Geologic map of Minnesota, Quaternary geology*, State map series, S-1, scale 1:500,000, Minn. Geological Survey, St. Paul, Minn. [Available at http://hdl.handle.net/11299/60085, last accessed 29 May 2014].

Horizon Systems (2014), NHDPlus Version 2, Horizon Systems Corporation, Herndon, Va. [Available at http://www.horizon-systems.com/NHDPlus/NHDPlusV2_home.php, last accessed 1 April 2016].

Istvánovics, V., M. Honti, A. Kovács, G. Kocsis, and I. Stier (2014), Phytoplankton growth in relation to network topology: time-averaged catchment-scale modelling in a large lowland river, *Freshwater Biology*, doi:10.1111/fwb.12388.

Jacobson, R. B. and K. B. Gran (1999), Gravel sediment routing from widespread, low-intensity landscape disturbance, Current River Basin, Missouri, *Earth Surf. Process. Landforms*, 24(10), 897-917, doi:10.1002/(SICI)1096-9837(199909)24:10<897::AID-ESP18>3.0.CO;2-6.

Jin, S., L. Yang, P. Danielson, C. Homer, J. Fry, and G. Xian (2013), A comprehensive change detection method for updating the National Land Cover Database to circa

2011, *Remote Sensing of Environment*, 132, 159-175, doi:10.1016/j.rse.2013.01.012.
Johnson, J.W. (1943), Distribution graphs of suspended-matter concentration, *Transactions of the American Society of Civil Engineers*, 108(1), 941–956.
Kalin, L., R. S. Govindaraju, and M. M. Hantush (2004a), Development and application of a methodology for sediment source identification. I: Modified unit sedimentograph approach, *J. Hydrol. Eng.*, 9(3), 184–193, doi:10.1061/(ASCE)1084-0699(2004)9:3(184).
Kalin, L., R. S. Govindaraju, and M. M. Hantush (2004b), Development and application of a methodology for sediment source identification. II: Optimization approach, *J. Hydrol. Eng.*, 9(3), 194–207, doi:10.1061/(ASCE)1084-0699(2004)9:3(194).
Kelley, D. W., and E. A. Nater (2000), Historical sediment flux from three watersheds into Lake Pepin, Minnesota, USA, *J. Environ. Qual.*, 29, 561–568, doi:10.2134/jeq2000.00472425002900020025x.
Keulegan, G. H. (1938), Laws of turbulent flow in open channels, *Journal National Bureau of Standards*, Research Paper 1151, 21, 707-741, Washington, D.C.
Kirkby, M. J. (1976), Tests of the random network model and its application to basin hydrology, *Earth Surf. Process.*, 1, 197–212, doi:10.1002/esp.3290010302.
Kirsch, N. A., S. A. Hanson, P. A. Renard, and J. W. Enblom (1985), *Biological survey of the Minnesota River*, Minnesota Dept. of Natural Resources Fisheries, Special Publication #139, St. Paul, Minn., 85 p., [Available at http://files.dnr.state.mn.us/publications/fisheries/special_reports/139.pdf, last accessed 22 April 2016].
Kumar, S., and R. A. Rastogi (1987), A conceptual catchment model for estimating suspended sediment flow, *J. Hydrol.*, 95, 155–163, doi:10.1016/0022-1694(87)90122-3.
Kronvang, B., H. E. Andersen, S. E. Larsen, and J. Audet (2013), Importance of bank erosion for sediment input, storage and export at the catchment scale, *J. Soils Sediments*, 13, 230-241, doi:10.1007/s11368-012-0597-7.
Lagasse, P. F., W. J. Spitz, L. W. Zevenbergen, and D. W. Zachmann (2004), *Handbook for predicting stream meander migration*, National Cooperative Highway Research Program Report 533, Transportation Research Board of the National Academies, Washington, D.C., 105 p. (http://onlinepubs.trb.org/onlinepubs/nchrp/nchrp_rpt_533.pdf) last accessed 24 May 2014.
Lane, S. N., S. C. Reid, V. Tayefi, D. Yu, and R. J. Hardy (2008), Reconceptualising coarse sediment delivery problems in rivers as catchment-scale and diffuse, *Geomorphology*, 98, 227–249, doi:10.1016/j.geomorph.2006.12.028.
Lark, T. J., J. M. Salmon, and H. K. Gibbs (2015), Cropland expansion outpaces agricultural and biofuel policies in the United States, *Environ. Res. Lett.*, 10(4), 044003, doi:10.1088/1748-9326/10/4/044003.
Lauer, J. W., and G. Parker (2008), Net local removal of floodplain sediment by river meander migration, *Geomorphology*, 96, 123–149, doi:10.1016/j.geomorph.2007.08.003.

Lauer, J. W., and J. Willenbring (2010), Steady state reach-scale theory for radioactive tracer concentration in a simple channel/floodplain system, *J. Geophys. Res.*, 115, F04018, doi:10.1029/2009JF001480.

Lauer, J. W., E. Viparelli, and H. Piégay (2016), Morphodynamics and sediment tracers in 1-D (MAST-1D): 1-D sediment transport that includes exchange with an off-channel sediment reservoir, *Advances in Water Resources*, doi:10.1016/j.advwatres.2016.01.012.

Lee, K. T., and C.-C. Yang (2010), Estimation of sediment yield during storms based on soil and watershed geomorphology characteristics, *J. Hydrol.*, 382, 145–153, doi:10.1016/j.jhydrol.2009.12.025.

Lee, Y. H., and V. P. Singh (1999), Prediction of sediment yield by coupling Kalman filter with instantaneous unit sediment graph, *Hydrol. Process.*, 13(17), 2861–2875, doi:10.1002/(SICI)1099-1085(19991215)13:17<2861::AID-HYP805>3.0.CO;2-Z.

Lenhart, C. F., M. L. Titov, J. S. Ulrich, J. L. Nieber, B. J. Suppes (2013), The role of hydrologic alteration and riparian vegetation dynamics in channel evolution along the lower Minnesota River, *Transactions of the American Society of Agricultural and Biological Engineers*, 56(2), 549-561, doi: 10.13031/2013.42686.

Leopold, L. B., and Maddock Jr., T. (1953), The hydraulic geometry of stream channels and some physiographic implications, *U. S. Geological Survey Professional Paper*, 252, Washington, D.C., 57 p.

Leopold, L. B., M. G. Wolman, and J. P. Miller (1964), *Fluvial Processes in Geomorphology*, W. H. Freeman, San Francisco, Calif.

Lisle, T. E. (2008), The evolution of sediment waves influenced by varying transport capacity in heterogeneous rivers, in *Gravel Bed Rivers VI: From Process Understanding to River Restoration*, edited by H. Habersack, H. Piegay, and M. Rinaldi, pp. 443–472, Elsevier, Amsterdam, doi: 10.1016/S0928-2025(07)11136-6.

Lisle, T. E., Y. Cui, G. Parker, J. E. Pizzuto, and A. M. Dodd (2001), The dominance of dispersion in the evolution of bed material waves in gravel-bed rivers, *Earth Surf. Process.*, 26, 1409-1420, doi: 10.1002/esp.300.

Lisle, T. E., J. E. Pizzuto, H. Ikeda, F. Iseya, and Y. Kodama (1997), Evolution of a sediment wave in an experimental channel, *Water Resour. Res.*, 33(8), 1971-1981, doi: 10.1029/97WR01180.

Maidment, D. R., F. Olivera, A. Calver, A. Eatherall, and W. Fraczek (1996), Unit hydrograph derived from a spatially distributed velocity field, *Hydrol. Process.*, 10(6), 831–844, doi:10.1002/(SICI)1099-1085(199606)10:6<831::AID-HYP374>3.0.CO;2-N.

Malmon, D. V., T. Dunne, and S. L. Reneau (2003), Stochastic theory of particle trajectories through alluvial valley floors, *J. Geol.*, 111, 525–542.

Mantilla, R., V. K. Gupta, O. J. Mesa (2006), Role of coupled flow dynamics and real network structures on Hortonian scaling of peak flows, 322, 155-167, doi:10.1016/j.jhydrol.2005.03.022.

Marani, A., R. Rigon, and A. Rinaldo (1991), A Note on Fractal Channel Networks, *Water Resour. Res.*, 27(12), 3041–3049, doi:10.1029/91WR02077.

Mari, L., E. Bertuzzo, R. Casagrandi, M. Gatto, S. A. Levin, I. Rodriguez-Iturbe, and A. Rinaldo (2011), Hydrologic controls and anthropogenic drivers of the zebra mussel invasion of the Mississippi-Missouri river system, Water Resour. Res., 47, W03523, doi:10.1029/2010WR009920.

Marschner, F. J. (1974), *The Original Vegetation of Minnesota, a Map Compiled in 1930 by F.J. Marschner Under the Direction of M.L. Heinselman of the United States Forest Service*, Map 1:500,000, Cartogr. Lab. of the Dep. of Geogr., Univ. of Minn., St. Paul, Minn.

Massoudieh, A., A. Gellis, W. S. Banks, and M. E. Wieczorek (2013), Suspended sediment source apportionment in Chesapeake Bay watershed using Bayesian chemical mass balance receptor modeling, *Hydrol. Process.*, 27, 3363-3374, doi:10.1002/hyp.9429.

McCluney, K. E., N. L. Poff, M. A. Palmer, J. H. Thorp, G. C. Poole, B. S. Williams, M. R. Williams, and J. S. Baron (2014), Riverine macrosystems ecology: sensitivity, resistance, and resilience of whole river basins with human alterations, *Front. Ecol. Environ.*, 12(1), 48-58, doi:10.1890/120367.

McKay, L., T. Bondelid, T. Dewald, et al. (2012), NHDPlus Version 2: User Guide, U.S. Environmental Protection Agency, Washington, D.C. (ftp://ftp.horizon-systems.com/NHDPlus/NHDPlusV21/Documentation/NHDPlusV2_User_Guide.pdf), last accessed 1 April 2016.

Mesa, O. J., and E. R. Mifflin (1986), On the relative role of hillslope and network geometry in hydrologic response, in *Scale Problems in Hydrology*, edited by V. K. Gupta, I. Rodriguez-Iturbe, and E. F. Wood, pp. 1–17, D. Reidel, Dordrecht, Holland.

Michaels, P. J., P. C. Knappenberger, O. W. Frauenfeld, and R. E. Davis (2004), Trends in precipitation on the wettest days of the year across the contiguous USA, *Int. J. Climatol.*, 24(15), 1873–1882, doi:10.1002/joc.1102.

Motta, D., J. D. Abad, E. J. Langendoen, M. H. Garcia (2012), A simplified 2D model for meander migration with physically-based bank evolution, *Geomorphology*, 163-164, 10-25, doi:10.1016/j.geomorph.2011.06.036.

MPCA (2014), General report to the Congress of the United States pursuant to section 305(b) of the 1972 Clean Water Act: water years 2012-2013, *Minnesota Pollution Control Agency Report wq-s7-50*, 62 p., St. Paul, Minn. [Available at https://www.pca.state.mn.us/water/water-quality-assessment-and-listing, last accessed 26 April 2016].

Muneepeerakul, R., E. Bertuzzo, H. J. Lynch, W. F. Fagan, A. Rinaldo, and I. Rodriguez-Iturbe (2008), Neutral metacommunity models predict fish diversity patterns in Mississippi-Missouri basin, Nature, 453, 220– 222, doi:10.1038/nature06813.

Musser, K., S. Kudelka, and R. Moore (2009), Minnesota River Basin trends, *Water Resources Center Report*, Minnesota State University, Mankato, MN, 64 p.

Muzik, I. (1996), Flood modeling with GIS-derived distributed unit hydrographs, *Hydrol. Process.*, 10(10), 1401–1409, doi:10.1002/(SICI)1099-

1085(199610)10:10<1401::AID-HYP469>3.0.CO;2-3.
Nash, J. E. (1957), The form of the instantaneous unit hydrograph, *Bull. Int. Assoc. Sci. Hydrol.*, 3, 114–121.
Neal, C. W. M., and A. M. Anders (2015), Suspended sediment supply dominated by bank erosion in a low-gradient agricultural watershed, Wildcat Slough, Fisher, Illinois, United States, *Journal of Soil and Water Conservation*, 70(3), 145-155, doi:10.2489/jswc.70.3.145.
Novotny, E. V., and H. G. Stefan (2007), Stream flow in Minnesota: indicator of climate change, *J. Hydrology*, 334(3-4), 319-333, doi:10.1016/j.jhydrol.2006.10.011.
Ojakangas, R. W., and C. L. Matsch (1982), *Minnesota's Geology*, 255 p., Univ. of Minn. Press, Minneapolis, Minn.
Paola, C., P. L. Hellert, and C. L. Angevine (1992), The large-scale dynamics of grain-size variation in alluvial basins, 1: Theory, *Basin Res*., 4(2), 73–90, doi:10.1111/j.1365-2117.1992.tb00145.x.
Park, C. C. (1977), World-wide variations in hydraulic geometry exponents of stream channels: an analysis and some observations, *J. Hydrol.*, 33, 133–146, doi:10.1016/0022-1694(77)90103-2.
Parker, G. (2004), 1D aggradation and degradation of rivers: Normal flow assumption, chap. 14, in *1D Sediment Transport Morphodynamics with Applications to Rivers and Turbidity Currents*, Urbana, Illinois, 38 p. [Available at http://hydrolab.illinois.edu/people/parkerg//morphodynamics_e-book.htm, last accessed 1 April 2016].
Parker, G. (2008), Transport of gravel and sediment mixtures, in *Sedimentation engineering: Processes, measurements, modeling, and practice: ASCE manuals and reports on engineering practice*, 110, edited by Garcia, M.H., ASCE, Reston, Virginia, 165–251.
Parker, G., Y. Shimizu, G. V. Wilkerson, E. C. Eke, J. D. Abad, J. W. Lauer, C. Paola, W. E. Dietrich, and V. R. Voller (2011), A new framework for modeling the migration of meandering rivers, *Earth Surf. Process. Landforms*, 36(1), 70-86, doi:10.1002/esp.2113.
Passalacqua, P., P. Belmont, and E. Foufoula-Georgiou (2012), Automatic geomorphic feature extraction from lidar in flat and engineered landscapes, *Water Resour. Res.*, 48, W03528, doi:10.1029/2011WR010958.
Passalacqua, P., P. Belmont, D. M. Staley, J. D. Simley, J. R. Arrowsmith, C. E. Bode, C. Crosby, S. B. DeLong, N. F. Glenn, S. A. Kelly, D. Lague, H. Sangireddy, K. Schaffrath, D. G. Tarboton, T. Wasklewicz, J. M. Wheaton (2015), Analyzing high resolution topography for advancing the understanding of mass and energy transfer through landscapes: A review, *Earth Science Reviews*, 148, 174-193, doi:10.1016/j.earscirev.2015.05.012.
Pizzuto, J. E. (2012), Predicting the accumulation of mercury-contaminated sediment on riverbanks—An analytical approach, *Water Resour. Res.*, 48, W07518, doi:10.1029/2012WR011906.
Pizzuto, J., E. R. Schenk, C. R. Hupp, A. Gellis, G. Noe, E. Williamson, D. L. Karwan, M. O'Neal, J. Marquard, R. Aalto, and D. Newbold (2014), Characteristic length

scales and time-averaged transport velocities of suspended sediment in the mid-Atlantic region, USA, *Water Resour. Res.*, 50(2), 790–805, doi:10.1002/2013WR014485.

Pryor, S. C., J. A. Howe, and K. E. Kunkel (2009), How spatially coherent and statistically robust are temporal changes in extreme precipitation in the contiguous USA?, *Int. J. Climatol.*, 29(1), 31–45, doi:10.1002/joc.1696.

Raghuwanshi, N.S., R.A. Rastogi, and S. Kumar (1994), Instantaneous-unit sediment graph, *J. Hydraul. Eng.*, 120(4), 495–503, doi:10.1061/(ASCE)0733-9429(1994)120:4(495).

Reid, S. C., S. N. Lane, D. R. Montgomery, C. J. Brookes (2007a), Does hydrological connectivity improve modelling of coarse sediment delivery in upland environments?, *Geomorphology*, 90, 263–282, doi:10.1016/j.geomorph.2006.10.023.

Reid, S. C., S. N. Lane, J. M. Berney, and J. Holden (2007b), The timing and magnitude of coarse sediment transport events within an upland, temperate gravel-bed river, *Geomorphology*, 83, 152–182, doi:10.1016/j.geomorph.2006.06.030.

Renard, K. G., G. R. Foster, G. A. Weesies, D. K. McCool, and D. C. Yoder (1997), Predicting soil erosion by water: a guide to conservation planning with the Revised Universal Soil Loss Equation (RUSLE) (Vol. 703). Washington, DC: United States Department of Agriculture, 407 p.

Rinaldo, A., A. Marani, and R. Rigon (1991), Geomorphological dispersion, *Water Resour. Res.*, 27(4), 513–525, doi:10.1029/90WR02501.

Rinaldo, A., and I. Rodriguez-Iturbe (1996), Geomorphological theory of the hydrological response, *Hydrological Processes*, 10(6), 803-829, doi:10.1002/(SICI)1099-1085(199606)10:6<803::AID-HYP373>3.0.CO;2-N.

Rinaldo, A., G. Botter, E. Bertuzzo, A. Uccelli, T. Settin, and M. Marani (2006a), Transport at basin scales: 1. Theoretical framework, *Hydrol. Earth Sys. Sci.*, 10, 19–29, doi:10.5194/hess-10-19-2006.

Rinaldo, A., G. Botter, E. Bertuzzo, A. Uccelli, T. Settin, and M. Marani (2006b), Transport at basin scales: 2. Applications, *Hydrol. Earth Sys. Sci.*, 10, 31–48, doi:10.5194/hess-10-31-2006.

Rinaldo, A., P. Benettin, C. J. Harman, M. Hrachowitz, K. J. McGuire, Y. van der Velde, E. Bertuzzo, and G. Botter (2015), Storage selection functions: A coherent framework for quantifying how catchments store and release water and solutes, *Water Resour. Res.*, 51, 4840–4847, doi:10.1002/2015WR017273.

Rodriguez-Iturbe, I., and A. Rinaldo (1997), Fractal river basins: chance and self-organization, Cambridge University Press, New York, NY, 564 p.

Rodriguez-Iturbe, I., and J. B. Valdes (1979), The geomorphologic structure of hydrologic response, *Water Resour. Res.*, 15, 1409–1420, doi:10.1029/WR015i006p01409.

Schmitt, R. J. P., Bizzi, S. and Castelletti, A. (2016), Tracking multiple sediment cascades at the river network scale identifies controls and emerging patterns of sediment connectivity. *Water Resour. Res.*. Accepted Author Manuscript. doi:10.1002/2015WR018097.

Schottler, S. P., J. Ulrich, P. Belmont, R. Moore, J. W. Lauer, D. R. Engstrom, and J. E. Almendinger (2014), Twentieth century agricultural drainage creates more erosive rivers, *Hydrol. Processes*, 28(4), 1951–1961, doi:10.1002/hyp.9738.

Shah-Fairbank, S. C., P. Y. Julien, and D. C. Baird (2011), Total sediment load from SEMEP using depth-integrated concentration measurements, *J. Hydraul. Eng*., 137(12), 1606–1614, doi:10.1061/(ASCE)HY.1943-7900.0000466.

Sharma, K. D., R. P. Dhir, and J. S. R. Murthy (1992), Modelling suspended sediment flow in arid upland basins, *Hydrol. Sci.*, 37(5), 481–490, doi:10.1080/02626669209492613.

Shenk, G. W., and L. C. Linker (2013), Development and application of the 2010 Chesapeake Bay watershed Total Maximum Daily Load Model, *J. Am. Water Resour. Assoc.*, 49(5), 1042–1056, doi:10.1111/jawr/12109.

Sherman, L. K. (1932), Streamflow from rainfall by the unit-graph method, *Eng. News Record*, 108, 501–505.

Singh, P. K., P. K. Bhunya, S. K. Mishra, and U. C. Chaube (2008), A sediment graph model based on SCS-CN method, *J. Hydrol.*, 349, 244–255, doi:10.1016/j.jhydrol.2007.11.004.

Sklar, L. S., J. Fadde, J. G. Venditti, P. Nelson, M. A. Wydzga, Y. Cui, and W. E. Dietrich (2009), Translation and dispersion of sediment pulses in flume experiments simulating gravel augmentation below dams, *Water Resour. Res.*, 45, W08439, doi: 10.1029/2008WR007346.

STATSGO2 (2015), Description of the STATSGO2 database, Natural Resources Conservation Service, Washington, D.C. [Available at http://www.nrcs.usda.gov/wps/portal/nrcs/detail/soils/survey/geo/?cid=nrcs142p2_053629, last accessed 4 August 2015].

Trimble, S. W. (1983), A sediment budget for Coon Creek basin in the Driftless Area, Wisconsin, 1853-1977, *American Journal of Science*, 283(5), 454-474, doi:10.2475/ajs.283.5.454.

Trimble, S. W. (1981), Changes in sediment storage in the Coon Creek basin, Driftless Area, Wisconsin, 1853 to 1975, *Science*, 214(4517), 181-183, doi:10.1126/science.214.4517.181.

Troutman, B. M., and M. R. Karlinger (1985), Unit hydrograph approximations assuming linear flow through topologically random channel networks, *Water Resour. Res.*, 21, 743–754, doi:10.1029/WR021i005p00743.

U.S. Geological Survey (2012), National map, *http://nationalmap.gov*, (accessed November 9, 2012).

U.S. Geological Survey (2014), *USGS Water Data for Minnesota*, U.S. Geological Survey, Reston, Va. [Available at http://waterdata.usgs.gov/mn/nwis?, last accessed 20 May 2014].

van de Lageweg, W. I., W. M. van Dijk, A. W. Baar, J. Rutten, and M. G. Kleinhans (2014), Bank pull or bar push: What drives scroll-bar formation in meandering rivers?, *Geology*, 42(4), 319-322, doi:10.1130/G35192.1.

Vanoni, V. A., ed. (1975), *Sedimentation engineering*, vol. 54 of the American Society of Engineers Manuals and Reports on Engineering Practice, 726 p.

Viparelli, E., J. W. Lauer, P. Belmont, and G. Parker (2013), A numerical model to develop long-term sediment budgets using isotopic sediment fingerprints, *Computers & Geosciences*, 53, 114-122, doi:10.1016/j.cageo.2011.10.003.

Wainwright, J. (2006), Degrees of separation: Hillslope-channel coupling and the limits of palaeohydrological reconstruction, *Catena*, 66(1-2), 93-106, doi:10.1016/j.catena.2005.07.016.

Wilcock, P. (2009), *Identifying Sediment Sources in the Minnesota River Basin*, Minnesota Pollution Control Agency, report number wq-b3-43, Mankato, MN. 16 p. (http://www.pca.state.mn.us/index.php/view-document.html?gid=8099) last accessed April 29, 2014.

Wilcock, P. R., and J. C. Crowe (2003), Surface-based transport model for mixed-size sediment, *J. Hydraul. Eng.*, 129(2), 120–128, doi:10.1061/(ASCE)0733-9429(2003)129:2(120).

Wilkinson, S. N., I. P. Prosser, and A. O. Hughes (2006), Predicting the distribution of bed material accumulation using river network sediment budgets, *Water Resour. Res.*, 42, W10419, doi:10.1029/2006WR004958.

Williams, J.R. (1978), A sediment graph model based on instantaneous unit sediment graph, *Water Resour. Res.*, 14(4), 659–664, doi:10.1029/WR014i004p00659.

Wong, M., and G. Parker (2006), Reanalysis and correction of bed-load relation of Meyer-Peter and Muller using their own database, *J. Hydraul. Eng.*, 132(11), 1159–1168, doi:10.1061/(ASCE)0733-9429(2006)132:11(1159).

Wu, W., and S. Wang (2006), Formulas for sediment porosity and settling velocity, *J. Hydraul. Eng.*, 132, 858-862, doi:10.1061/(ASCE)0733-9429(2006)132:8(858).

Zhang, Y. K., and K. E. Schilling (2006), Increasing streamflow and baseflow in Mississippi River since the 1940s: effect of land use change, *J. Hydrology*, 324(1-4), 412-422, doi:10.1016/j.jhydrol.2005.09.033.